

## Heterogeneous catalyst preparation by liquid-phase atomic layer deposition

Présentée le 19 juin 2020

à la Faculté des sciences de base  
Laboratoire des procédés durables et catalytiques  
Programme doctoral en chimie et génie chimique

pour l'obtention du grade de Docteur ès Sciences

par

**Benjamin Pierre LE MONNIER**

Acceptée sur proposition du jury

Prof. A.-C. Corminboeuf, présidente du jury  
Prof. J. S. Luterbacher, directeur de thèse  
Prof. X. Carrier, rapporteur  
Dr B. O'Neil, rapporteur  
Prof. K. Sivula, rapporteur



# Acknowledgements

## *To the family and friends*

I am thankful for the strong and unconditional support from my close family despite the distance that PhD studies impose and it is even more remarkable considering their unawareness of the challenge that represent a doctoral study. I will never be enough thankful for the life lessons from my grandpa, Gérard Le Monnier. The echo of his words pulled me out of the toughest times.

I am thankful for the team of skilled chemical engineers with whom I spent most of my PhD, Dr. Ydna Questell and Dr. Masoud Talebi. Good days and bad days, they were always there to support, to cheer up, and to have fun, in or out of the lab. Our differences of cultures mixed with the turbulences of the PhD studies forged an unlikely, long-lasting friendship that I am grateful for.

During my PhD, I also bonded with almost doctors (Luca S. and Christophe B.), baby PhD students (Marina C. and Lorenz M.), and actual doctors (Dr. Louisa S. and Dr. Gael P.). Each of them participated in making my life brighter. I shared with them small and big moments that mattered. I thank you all.

I owe a great deal to some good people that encouraged me, trusted me and bore my isolation and my roller coaster mood during these years. I haven't been able to express the gratitude that they deserve. Without you, I would not have made it, Céline (Pépette) L., Lidivine B., Chloé W., Anne Laure E. and Ken G.

## *To the peers who made me a chemist*

On the academic side, I thank professors and labs that pumped up my motivation and ambition. In order of appearance in my life, Prof. Samuel George who initiated me to solid state chemistry. Prof. Yves Wouters and Prof. Frederick Lemaître for their singular perspective on chemical reactions. Prof. Xavier Carrier and Prof. Petra de Jongh who transferred to me their passion for catalysis and nano-material preparation. I thank also Prof. Kevin Sivula who I look up to as a mentor. His availability when I needed help and his scientific guidance were crucial in the achievement of my work. Finally, I thank Prof. Jeremy S. Luterbacher who offered me this opportunity to work at EPFL and gave me the freedom I needed to explore my ideas.

At last, I am thankful for my jury members. I am very pleased to present my work to them as I greatly value their opinion. I did not ease my task by picking such experts, but their critiques and advice are those that matter to me.

From the bottom of my heart, thank you all.

Condat sur Vienne, le 24 décembre 2019

# Abstract

Heterogeneous catalyst preparation has been performed for close to a century but has been rapidly evolving spurred by the evolution in synthetic techniques and growing needs in energy, chemicals and materials. An increasing number of catalyst synthesis strategies and tools have emerged in the past decades, including Atomic Layer Deposition (ALD). This technique allows the deposition of thin films with unmatched accuracy. Originally designed for flat substrates, this method has recently begun to be used for the preparation of heterogeneous catalysts.

The development of ALD, both in academic research and industrial processing, is inhibited by inherent high investment and operating costs of the technique. The global aim of this doctoral project was to design new ALD processes specifically designed for heterogeneous catalyst preparation. This aim is achieved in three steps: transposing gas-phase layer-by-layer growth to the liquid phase, matching the quality and versatility of gas-phase ALD in the liquid phase, and finally going beyond what is technically possible with gas-phase ALD set-ups.

The first chapter of this manuscript describes current state-of-the-art methods used both in heterogeneous catalyst preparation and atomic layer deposition on particles. This chapter does not aim to be a comprehensive review but to present the main research developments necessary to understand this thesis work in a broader context.

The second chapter is based on a published article in which I describe a first step toward liquid-phase ALD. A procedure was developed for stoichiometrically limited layer-by-layer deposition of alumina in solution onto a copper-based catalyst. A conformal porous layer was obtained which allowed the diffusion of chemicals to the copper below. Additionally, the deposited layer was an efficient barrier against irreversible deactivation during the catalytic hydrogenation of a biosourced molecule in a continuous flow reactor.

The third chapter, based on a published communication, presents the fully optimized method for liquid-phase ALD. In this work, I demonstrate the self-limiting nature of the studied chemical reactions and use this process to deposit various type of inorganic layers (oxide, phosphate and sulfide) on a broad range of substrates relevant for catalysis. This technique also allows a direct monitoring of surface reaction, highlighting phenomena such as nucleation of clusters and their coalescence to form films. The materials were extensively characterized by electronic microscopy to confirm that the quality of the coating matched that of coatings obtained via gas-phase ALD.

The fourth chapter describes soon to be submitted work where deposition is used during the early stages of nucleation on a surface to form targeted atomic clusters for catalysis. The goal was to build a catalytic cluster atom-by-atom to carefully tune its chemical environment. Starting from a single Zn atom deposited on silica, I demonstrate the positive effect of Al on dehydrogenation catalytic activity and the enhancement of stability brought by Si anchoring. These effects demonstrate that liquid-phase ALD can be more than just a tool for overcoating catalysts but also a method for the rational design of new catalysts.



Finally, the thesis concludes with my perspective on new challenges and opportunities in the further development of liquid-phase ALD.

## Keywords

Heterogeneous catalysis, atomic layer deposition, materials preparation, nanomaterials, surface chemistry

# Résumé

La préparation de catalyseurs hétérogènes se fait depuis près d'un siècle mais cela a rapidement évolué, stimulée par maturation des techniques de synthèse et la demande croissante en énergie, produits chimiques et matériaux. Un nombre grandissant de stratégies et d'outils pour la synthèse de catalyseurs ont émergé ces dernières dizaines d'années, dont le Dépôt par Couche Atomique (ALD). Cette technique permet la déposition de films minces avec une précision inégalée. A l'origine conçue pour des supports plats, cette méthode est de plus en plus utilisée pour la préparation de catalyseurs.

Le développement de l'ALD, dans les domaines académiques et industriels, est ralenti par un haut coût d'investissement et de fonctionnement, inhérent à la technique. L'objectif global de ce projet de thèse était de concevoir un nouveau procédé d'ALD, spécialement dédié à la préparation de catalyseurs hétérogènes. Cet objectif fut accompli en trois étapes: transposer la croissance en phase gaz à une croissance en phase liquide, égaler la qualité et la versatilité de l'ALD en phase gaz, puis aller au-delà de ce qui est techniquement possible avec les systèmes d'ALD actuels.

Le premier chapitre de ce document fait l'état de l'art des méthodes utilisées pour la préparation de catalyseurs hétérogènes et de l'ALD sur poudre. L'objectif de ce chapitre n'est pas de faire une revue exhaustive de la littérature mais de présenter les principales avancées dans le domaine pour comprendre la place de cette thèse dans un contexte global.

Le deuxième chapitre est basé sur un article publié où je décris un premier pas vers l'ALD en phase liquide. Une procédure a été développée pour le dépôt en couche par couche stœchiométrique d'alumine, en solution, sur un catalyseur à base de cuivre. Une couche poreuse et conforme fut obtenue, ce qui permet la diffusion des réactifs vers le cuivre. De plus, la couche déposée est une barrière efficace contre la désactivation irréversible du catalyseur pendant l'hydrogénation de molécules biosourcées.

Le troisième chapitre, basé sur une communication publiée, présente la méthode pour l'ALD en phase liquide finale. Dans ces travaux, j'ai démontré la nature auto limitante des réactions étudiées et utilisé ce procédé pour déposer des couches inorganiques sur une large gamme de substrats, importants en catalyse. Cette technique permet un suivi des réactions de surface, éclairant des phénomènes tels que la nucléation et la coalescence de nuclei. Les matériaux ont été analysés en détail par microscopie électronique pour confirmer que la qualité de la couche égale celle préparée par ALD en phase gaz.

Le quatrième chapitre décrit des travaux, bientôt soumis pour publication, où la déposition est utilisée uniquement lors des premières étapes de nucléation sur une surface pour fabriquer des petits groupes d'atomes pour la catalyse. L'objectif est de construire, atome par atome, un site actif afin de l'ajuster précisément. A partir d'un seul atome de Zn déposé sur silice, j'ai démontré l'effet positif de la présence d'un atome Al voisin sur l'activité catalytique ainsi que le gain en stabilité par l'ancrage par un atome de Si. Ces effets montrent que l'ALD en phase liquide est plus qu'un outil pour faire des couches minces mais aussi une méthode pour la conception rationnelle de nouveaux catalyseurs.

Finalement, la thèse se conclut avec ma perspective sur les nouveaux défis et nouvelles opportunités dans le développement de l'ALD en phase liquide.

## Mots-clés

Catalyse hétérogène, dépôt par couche atomique, préparation de matériaux, nanomatériaux, chimie de surface

# Contents

<b>Acknowledgements.....</b>	<b>iii</b>
<b>Abstract .....</b>	<b>iv</b>
<b>Résumé .....</b>	<b>vi</b>
<b>List of Figures .....</b>	<b>xi</b>
<b>List of Tables .....</b>	<b>xix</b>
<b>List of Equations .....</b>	<b>xx</b>
<b>Chapter 1      Introduction .....</b>	<b>21</b>
1.1    A brief overview on catalysts and catalysis .....	21
1.2    Structure and chemistry of heterogeneous catalysts .....	22
1.2.1 Components of heterogeneous catalysts .....	22
1.2.2 Unwanted modifications of heterogeneous catalysts components .....	23
1.3    Preparation of heterogeneous catalysts .....	27
1.3.1 Supports .....	27
1.3.2 Nanoparticles .....	29
1.3.3 Single-atom catalysts .....	30
1.4    Atomic Layer Deposition for heterogeneous catalyst preparation .....	32
1.4.1 Chemistry of ALD .....	33
1.4.2 An overview of ALD utilization in heterogeneous catalysis .....	35
1.4.3 The difficult transition from wafer to powder.....	38
1.5    Objectives of this work .....	41
1.5.1 Layer-by-layer growth of metal oxides in solution .....	41
1.5.2 Matching liquid-phase atomic layer deposition's quality and versatility ....	42
1.5.3 Overcoming gas phase limitations.....	42
<b>Chapter 2      Layer-by-layer growth of a metal oxide in solution.....</b>	<b>43</b>
2.1    Introduction .....	44
2.2    Experimental.....	45
2.3    Results and discussion .....	47
2.4    Conclusions .....	53
2.4.1 Supplementary data.....	53

2.4.2	Acknowledgements.....	53
<b>Chapter 3</b>	<b>Developing a new method for liquid-phase ALD.....</b>	<b>55</b>
3.1	Abstract .....	56
3.2	Introduction .....	56
3.3	Results and discussion .....	58
3.4	Experimental Section.....	66
3.5	Conclusion.....	67
3.5.1	Supporting Information.....	68
3.5.2	Acknowledgements.....	68
<b>Chapter 4</b>	<b>Atom-by-atom design of catalytic clusters .....</b>	<b>69</b>
4.1	Abstract .....	70
4.2	Introduction .....	70
4.3	Results and discussion .....	72
4.4	Conclusion.....	77
4.5	Experimental section.....	78
4.5.1	Supplementary information.....	79
4.5.2	Acknowledgements.....	79
<b>A</b>	<b>Supporting information of chapter 2 .....</b>	<b>81</b>
A.1	Figures.....	81
A.2	Tables .....	85
A.3	Calculation of irregularity factor .....	85
A.4	Control experiments.....	86
A.5	Determination of mass transfer effects .....	86
<b>B</b>	<b>Supplementary information of chapter 3.....</b>	<b>89</b>
B.1	Figures.....	89
B.2	Details on material preparation based on previously published methods.....	99
B.3	Experimental considerations for TMA titrations.....	99
B.4	Estimation of mass transfer limitations.....	101
B.5	Solvent and ligand effects during TMA titrations .....	102
B.6	S4 Experimental considerations about water titrations.....	105
<b>C</b>	<b>Supplementary information of chapter 4.....</b>	<b>109</b>
<b>Chapter 5</b>	<b>Conclusion.....</b>	<b>112</b>

5.1	Achieved results .....	112
5.2	Future work and Outlook .....	113
<b>Bibliography .....</b>		<b>115</b>
<b>Curriculum vitae.....</b>		<b>124</b>

## List of Figures

**Figure 1.1:** Summary of frequent deactivation phenomena visualized at different scales. The active nanoparticles are represented in orange, the support in yellow and carbonaceous deposits in grey.....25

**Figure 1.2:** Scanning transmission electron microscopy images acquired with high annular angle detector and a bright field detector, representing various support structures. A) copper on TiO<sub>2</sub> P25 (catalyst prepared by Dr. Yeap), B) home-made silica “SBA-15”, C) commercial silica “KCC-1” and D) platinum nanoparticles over carbon support (catalyst prepared by Dr. Questell).....28

**Figure 1.3:** Examples of single atom catalysts (SACs). A) Ligand-free single atom Pt on alumina, B) Iron atom integrated in the structure of a carbon support, C) single atom alloy of Pd in Cu and D) Organometallic complex grafted on a silica surface. All figures were reproduced with permission from publishers<sup>[77–80]</sup>.....31

**Figure 1.4:** Description of the ALD cycle for alumina deposition on hydroxyl-bearing surface. A) the surface is covered with reactive hydroxyl groups. B) Precursor A, here trimethyl aluminum, is injected and saturates the surface. C) The excess is purged out, with the only remaining A being on the saturated surface. D) The counter-reactant B, here water, is injected and reacts with the surface. E) The excess is purged leaving a surface that is ready for a new cycle. The repetition of this cycle produced a film as represented on F). The figure has been adapted with the permission of the publisher<sup>[110]</sup>.....34

**Figure 1.5:** Examples of ALD utilization in the field of heterogeneous catalysis. (A) ALD was used as a protective overcoat on a supported Pd catalyst to avoid the formation of coke. (B) ALD was used to stabilize supported nanoparticles against sintering and the picture highlights the deposited layer surrounding the nanoparticle. (C) The scheme depicts an example where a thin overcoat stabilized a mesoporous material and prevented phase transition. (D) ALD is used with templating for improving the selectivity of the active surface beneath by creating a size-selective molecular overcoat. These figures were reproduced and adapted with the permission of the publishers<sup>[141,141,143,149]</sup>.....37

**Figure 1.6:** Example of ALD reactors for coatings on flat (wafer) substrates. (A) The most common reactor family for wafers where the main variation is in the position of inlet and outlet. (B) Batch ALD reactor where several wafers are loaded in same time. (C) Continuous ALD reactor with spatial separation of the processes, where the substrate moves from one zone to the next. (D) An alternate design of a continuous ALD reactor with spatial separation of the processes specifically designed for soft substrates that can be rolled from one zone to another. These figures were reproduced with the authorization of the publisher<sup>[185,186]</sup>.....39

**Figure 1.7:** Different ALD reaction chamber configurations representing the different strategies for processing powders. (A) the fixed bed reactor, (B) the fluidized bed reactor, (C) the rotary reactor, (D) flow through rotary reactor and (E) spatial (or pneumatic) reactor. ....40

**Figure 2.1:** STEM HAADF images of (A) Copper nanoparticles supported on alumina spheres ( $\text{Cu}/\text{Al}_2\text{O}_3$ ); (B)  $\text{Cu}/\text{Al}_2\text{O}_3$  after deposition of an amorphous alumina overcoat (60 cycles, using a water-to-aluminum molar ratio of 2.0).48

**Figure 2.2:** (A) Schematic representation of the aluminum precursor ( $\text{Al}(\text{OsBu})_3$ ) and its projected surface area. (B) Experimental setup for the stoichiometrically limited layer-by-layer overcoating. (C) Two-reaction sequence of a single overcoating cycle. (D) Evolution of BET surface area and additional catalyst mass as a function of the number of overcoating cycles (using a water to aluminum molar ratio of 2). ....49

**Figure 2.3:** Influence of the stoichiometry on the structural properties of the catalysts after deposition of 30 cycles. (A) Impact of the aluminum precursor quantity added per cycle (reported in number of equivalent monolayers or ML per cycle) on the thickness and conformality of the overcoat (using a water-to-aluminum molar ratio of 2.0). (B) Influence of water-to-aluminum ratio on the overcoat's density and on copper's accessibility. ....50

**Figure 2.4:** Catalytic activity per total moles of Cu of (A)  $\text{Cu} / \text{Al}_2\text{O}_3$  and (B)  $\text{Cu} / \text{Al}_2\text{O}_3$  after deposition of an amorphous alumina overcoat (60 cycles, using a water-to-aluminum molar ratio of 2.0) during the catalytic conversion of furfural into furfuryl alcohol in 1-butanol ( $130^\circ\text{C}$ , 22 bar, 35 mL/min  $\text{H}_2$ ). Catalysts were calcined at  $400^\circ\text{C}$  under air flow and reduced at  $300^\circ\text{C}$  under  $\text{H}_2$  flow between each run. ....52

**Figure 3.1:** Process of the liquid phase ALD by stoichiometric injection based on precursor and counter-reactant titration of dispersed powder substrate. ....58

**Figure 3.2** Surface titration by released methane quantification and mechanisms of alumina growth. a) Surface titration of available hydroxyl groups during TMA addition normalized by initial mass of substrate. b) Reaction schemes for TMA and a hydroxylated surface leading to the release of one or two molecules of methane per TMA. c) Surface titration of hydrolysable methyl groups after deposition of a stoichiometric quantity of TMA. d) Reaction schemes for water and an alkyl aluminum-covered surface leading to the release of one or two molecules of methane per molecule of water. e) and g) Growth per cycle (GPC), (i.e. quantity added at saturation) determined by TMA and water surface titration at each cycle on silica nanospheres, normalized by surface area with a starting hydroxyl density of e)  $2 \text{ OH}/\text{nm}^2$  and g)  $8 \text{ OH}/\text{nm}^2$ . The numerical labels above the water points refer to the water/aluminum ratio. f) Schematic representation of cluster growth showing, alternatively, a surface covered by pending aluminum, or bridging aluminum, leading to alternating high (up to 2) and low (as low as 1) water-to-aluminum ratios during each cycle. h) Sketches illustrating the various steps of ALD growth that



were observed: the nucleation and growth of clusters, their merging, and continuous film growth.....59

**Figure 3.3** a-c) Bright field transmission electron microscopy images of silica spheres coated with 10 cycles of TMA/water deposition using a) a commercial fluidized bed reactor ALD (2g batch) b) a round bottom flask (2g batch) c) the same procedure up-scaled to 158g. d) the same deposition method but on a basic substrate (MgO) with slightly higher surface area and e) using a high surface area silica as a substrate. f)  $\text{AlPO}_4$  deposited onto silica particles using the same method but replacing  $\text{H}_2\text{O}$  by  $\text{H}_3\text{PO}_4$  as a counter-reactant. g) ZnS deposited onto silica spheres by the same liquid phase method using diethyl zinc and hydrogen sulfide as reactants. h-n) Elemental mapping of the corresponding coated samples above using scanning transmission electron microscopy with an energy disperse X-ray detector. ....62

**Figure 3.4** a) Evolution of the dispersion measured by pulse CO chemisorption and Temperature Programmed Reduction (TPR) of bare and coated Palladium catalyst during several thermal aging cycles (oxidation/reduction). b) STEM-EDX pictures of supported palladium nanoparticles on silica coated with 20 cycles of stoichiometrically injected alumina. c) Particle size distribution of both protected and unprotected catalysts, measured by TEM. ....65

**Figure 4.1:** Schematic representation of different types of growth modes in atomic layer deposition (ALD) that could be leveraged in heterogeneous catalyst preparation. (A) ALD cycles on a surface densely covered with nucleation sites. A compact monolayer can be grafted on a surface, leading to a film growth<sup>[105]</sup>. (B) ALD cycles on a surface with a low concentration of nucleation site. In this case, a relatively large distance separates the grafted precursors leading to island formation<sup>[133]</sup>. (C) ALD “island” growth when injecting different precursor at each cycle. In this case, the sequence is not a binary loop. Instead, each cycle can feature a different component.....71

**Figure 4.2:** (A) trimethyl aluminum titration plots showing methane release following hydrolysis of the methyl ligands until full conversion of the surface hydroxyl groups. (B) DRIFTS spectra of dehydroxylated silica (black curve) and the same material after injection of exactly one aluminum monolayer (red curve). The full spectra are shown in **Figure C.1** (C) Schematic representation of the “Zn/Al” catalyst with the stoichiometries determined using Grignard, aluminum, water and zinc titrations, these results were confirmed by XPS (Zn/Al ratio of 1.9). (D) Schematic representation of the various catalysts, as prepared, at room temperature and in solvent. Considering the high temperature of reaction ( $550^\circ\text{C}$ ) and the consequent removal of solvent, all atoms are considered to be directly bond to the surface by covalent or dative bond during the catalytic run. The methyl groups on the silicon atoms are also expected to be burnt off. ....73

**Figure 4.3:** X-ray Photoelectron Spectra of Zn, Al and Zn/Al catalysts. (A) Zn 2p peak showing a shift from lower to higher binding energy when both metals are

present within the cluster on the silica surface. (B) Al 2p peak showing a shift from higher to lower binding energy when both metals are present within the cluster on the silica surface. ....74

**Figure 4.4:** (A) Temperature Programmed Reaction (TPR) of aluminum- and zinc-based catalysts showing the rate of propylene production versus temperature. (B) Arrhenius plots corresponding to the activity between 325 °C and 580 °C. 75

**Figure 4.5:** Catalytic tests in a quartz plug flow reactor at 1 atm, 50 mL/min flow rate (30% propane in He) at 550°C, with 100 mg of catalyst diluted in 0.5g of silicon carbide. (A) Rate of propylene production per time and mass of catalyst as a function of time on stream used to compare the absolute activity of the catalysts over time. (B) Relative rate normalized by the maximum initial activity to compare relative catalyst stability. ....76

**Figure A.1:** Particles size distribution for Cu/Al<sub>2</sub>O<sub>3</sub>. ....81

**Figure A.2 :** N<sub>2</sub> adsorption and desorption isotherms for Cu/Al<sub>2</sub>O<sub>3</sub> after deposition of 0, 15, 30, 45, and 60 Al<sub>2</sub>O<sub>3</sub> layers. ....82

**Figure A.3:** HAADF STEM pictures and EDX maps for Cu/Al<sub>2</sub>O<sub>3</sub> after 5 catalytic cycles (during the liquid phase hydrogenation of furfural) showing copper sintering. ....83

**Figure A.4:** Particles size distribution for Cu/Al<sub>2</sub>O<sub>3</sub> after 5 catalytic cycles (during the liquid phase hydrogenation of furfural). ....83

**Figure A.5:** Example of overcoat thickness measurements for irregularity factor determination (30 Al<sub>2</sub>O<sub>3</sub> cycles on Cu/Al<sub>2</sub>O<sub>3</sub>).....84

**Figure B.1:** Total methane released at each cycle after both aluminum and water injections. The results (which correspond to those shown in Figure 2e) show that the overall CH<sub>4</sub>/Al on each cycle is close to 3, indicating that the mass balance is closed. A 5% error was measured when repeating the experiments. ....89

**Figure B.2:** Growth per cycle (GPC) measured on high surface area silica (>350m<sup>2</sup>/g) showing a short cluster growth phase, a cluster merging phase and a film growth phase. As discussed in the main text, a low water-to-aluminum ratio is observed when clusters meet and alternating additions of higher (H<sub>2</sub>O to Al ratios >1) and lower (H<sub>2</sub>O to Al ratios <1) water-to-aluminum ratios are observed during film growth.....90

**Figure B.3:** Picture of the setup for surface titration and atomic layer deposition, which highlights the simplicity of the procedure and equipment along with its limited footprint. The Schlenck tube on the left-hand side contained the precursor solution while the tube on the right-hand side contained the counter reactant solution. The septum-capped round bottom flask contained the dispersed catalyst in the solvent of interest.....90

**Figure B.4:** Comparison between alumina coatings on silica nanospheres using our Liquid phase ALD method and gas phase ALD using a fluidized bed reactor. In

both cases, the silica spheres were coated with TMA/water 10 cycles. a-d) TEM bright field images showing that both coating are thin and conformal. e-h) STEM EDX elemental mapping highlighting the presence of alumina on silica surface, without free standing alumina nor uncoated particles. j and j) STEM-HAADF and TEM bright field images at low magnification, showing that the particles are well dispersed on the grid and not glued all together by the coating.....91

**Figure B.5:** Solid state nuclear magnetic resonance spectroscopy of: a) 10-cycles of alumina deposited on silica spheres by gas-phase ALD and b) 10-cycles of alumina deposited on silica spheres by the liquid-phase ALD presented in this work. Both spectra are very similar and feature an important peak corresponding to penta-coordinated aluminum, which indicates an amorphous phase.<sup>[283]</sup> .....92

**Figure B.6:** Powder X-ray diffraction pattern of 10-cycles of alumina deposited on silica spheres by gas-phase and liquid-phase ALD. Both are identical and only display a large peak around 22°, which corresponds to the silica core.<sup>[284]</sup> .92

**Figure B.7:** X-ray photoelectron spectroscopy (XPS) of 10-cycles of alumina deposited on silica spheres. a) Alumina peak shown for samples prepared by gas-phase ALD, b) Alumina peak shown for samples prepared by liquid-phase ALD. c) Oxygen peak shown for samples prepared by gas-phase ALD. d) Oxygen peak shown for samples prepared by liquid-phase ALD. The Peaks of aluminum have the same energy for the samples resulting from both liquid and gas phase preparation methods, indicating that the phase is the alumina same in both cases. Oxygen peaks can be deconvoluted into the alumina and silica contributions. The oxygen from the alumina phase has the same energy in both cases, confirming that the structure of the overcoat is the same for both preparation method. The higher total contribution of the oxygen from the silica in the case of preparation by liquid phase ALD is indicative of a thinner layer, which is consistent with what was observed by electron microscopy.<sup>[285,286]</sup> .....93

**Figure B.8:** Transmission electron microscopy images of commercial magnesium oxide coated with 10 TMA/water cycles in liquid phase. a) and d) are STEM HAADF images showing no traces of free alumina. b) and e) are EDX pictures showing that the alumina coating systematically follows the surface of the support. c) and f) are bright field pictures showing that alumina follows to a degree where its visualization is difficult.....94

**Figure B.9:** Transmission electron microscopy images of silica nanospheres coated with 10 TMA/water cycles in liquid phase using a reaction time of only 10 min between injections. a) Bright field image b) HAADF image c) and d) are the elemental mapping corresponding to the HAADF image. ....94

**Figure B.10:** Scanning transmission electron microscopy images of high surface area silica KCC (“hairy” spherical porous particles), coated with 10 TMA/water cycles in liquid phase. a-c) Imaging of the entire particle showing that aluminum is detected inside the porous ring of the material and not just on its outer surface. d-f)

A close-up of the outer ring showing “stripes” of aluminum following the silica pores. ....95

**Figure B.11:** N<sub>2</sub> adsorption isotherm at 77 K of a) bare high surface area silica b) the same material coated with 10 cycles of stoichiometric TMA/H<sub>2</sub>O. ....95

**Figure B.12:** Additional transmission electron microscopy analysis of silica nanospheres coated with 5 cycles of TMA/H<sub>3</sub>PO<sub>4</sub> in the liquid phase. a) Elemental mapping by EDX. b) Line scan corresponding the EDX picture shown in a), demonstrating that an overcoat contains Al, P and O while the bulk of the sphere is mainly composed of Si and O. c-f) Elemental mapping showing the distribution of silica and aluminum phosphate on the nanospheres, which confirms the highly conformal nature of the overcoat. ....96

**Figure B.13:** aluminum a) and phosphorus b) solid state NMR spectra of silica coated with 10-cycles of AlPO using on trimethyl aluminum and phosphoric acid injections. The aluminum peaks match with what expected for an amorphous aluminum phosphate phase. The phosphorus chemical shift also matched what was expected for an aluminum phosphate phase.<sup>[287,288]</sup> ....96

**Figure B.14:** XPS spectra of aluminum phosphate deposited onto silica spheres by 5 cycles of liquid phase ALD using injections of trimethyl aluminum and phosphoric acid. a) aluminum speak, b) phosphorous peak, c) oxygen peak and d) Si peak. The aluminum energy is relatively high, which is consistent with a phosphate or phosphonate phase.<sup>[288,289]</sup> The phosphorus peak energy matches that of a phosphate phase. No separation between the oxygen peaks of the phosphate and silica phases can be done because they are to close to close in energy. The silicon peak is consistent with a typical silica phase.<sup>[289][285]</sup> ....97

**Figure B.15:** TEM images of ZnS deposited on silica spheres by 5 cycles of liquid-phase ALD. a) TEM bright field image, b) EDX map, c) Electron diffraction pattern and d) STEM-HAADF image. The bright field picture reveals how homogeneously dispersed the crystallites are on the surface. The EDX mapping shows a continuous layer of ZnS consistent with a shell rather than isolated crystallites. The electron diffraction pattern shows clear diffraction spots, confirming that ZnS is at least partially crystalline. The STEM-HAADF imaging confirms that the ZnS layer is conformal and perfectly follows the surface of the substrate. ....98

**Figure B.16:** STEM-HAADF images of a) Palladium supported on silica nanospheres b) the same catalyst with an alumina overcoat (after 20 cycles of TMA/H<sub>2</sub>O deposition in liquid phase) after thermal treatment (600°C under 10%H<sub>2</sub> in Ar for 1 hour, 20 °C/min), and c) the same catalyst without an overcoat after thermal treatment showing several large (>10 nm) particles. ....99

**Figure B.17:** a) Study of the post saturation slope by repeating TMA surface titration on 1.3g (black squares) and 2.3g (blue triangles) of silica. b) TMA titration with and without silica showing that the slope after saturation is independent of the presence of a support. ....100

**Figure B.18:** Study of the solvent effect on the saturation point (equivalence at full coverage) and methane released during surface titration of silica with TMA (the slope represents the number of CH<sub>4</sub> molecules release per atom of Al added). .....103

**Figure B.19:** Density of alkyl aluminum deposition on commercial alumina spheres (hydroxyl density: 8 OH/nm<sup>2</sup>) depending on the ligand size and solvent that was used. In case 1), the deposition was performed using tri octyl aluminum (C<sub>8</sub>) in dibutyl ether. In case 2), the same precursor was used but the solvent was decane. In case 3) trimethyl aluminum (C<sub>1</sub>) was used in dibutyl ether and finally in 4) TMA was used in decane. ....104

**Figure B.20:** Titration curve of alumina spheres by tri octyl aluminum in dibutyl ether and decane. Contrary to TMA, the released ligand is in the liquid-phase, as is the excess of precursor. Therefore, after full coverage, octane from the excess of precursor is detected, leading to a slope of 3 since each precursor is hydrolyzed and releases all 3 ligands. ....105

**Figure B.21:** Hydrolysis of TMA solution in dibutyl ether by a solution of water in dioxane.....106

**Figure B.22:** Methane balance on the first cycle of deposition of trimethyl aluminum on silica powder, hydrolyzed by water solution in dioxane or pure water. ....107

**Figure B.23:** Superimposed chromatograms corresponding to a solution of TMA hydrolyzed by water in DBE (blue chromatogram) and a mixture of dioxane and DBE (pink chromatogram). a) the full chromatograms b) a zoom on the first half of it and c) a zoom on the last part. Above the peaks, the corresponding molecule, identified by mass spectroscopy. The certainty of the structure of the two last peaks (part c) is high due to the very low concentration of these compounds. Methane is assumed to be the first compound to come out (no MS detection due to too low concentration). ....108

**Figure C.1:** Full window of DRIFT spectra of dehydroxylated silica (in black) and the same material after adding a stoichiometric amount of tri methyl aluminum (in red). The peak at 3750 cm<sup>-1</sup> is attributed to isolated hydroxyl vibration. The peaks at 2963, 2936 and 2873 cm<sup>-1</sup> are attributed to CH<sub>2</sub> and CH<sub>3</sub> vibrations from the aluminum precursor and the solvent still attached). The contribution below 2000cm<sup>-1</sup> is mainly attributed to the vibrations of Si-O-Si bridges in the SiO<sub>2</sub> bulk.109

**Figure C.2:** Scanning transmission electron microscopy with energy disperse X-ray detector (STEM-EDX) elemental mapping of Al and Zn on as prepared “Zn-O-Al” catalyst. The sample display a homogeneous distribution of Al and Zn throughout the silica matrix which is consistent with a homogeneous monolayer rather than particles formation. ....109

**Figure C.3:** Picture of the U shape quartz reactor containing the catalyst diluted in silicon carbide (SiC) stuck between two plugs of quartz wool. The red circle

highlights the zone where the volatile zinc deposited after being carried off by the gas flow at high temperature.....110

**Figure C.4:** Comparison of spent catalysts. (A) a picture showing, from left to right, fresh “Zn-O-Al”, spent “Zn-O-Al” from catalysis in stainless steel reactor and spent “Zn-O-Al” from quartz reactor. The fresh and spent in quartz samples are white (as should be the concerned metal oxide) while the catalyst spent in stainless steel reactor is black, indicative of extensive carbon deposition. (B) Scanning transmission electron microscopy (STEM) picture taken with high annular angle field (HAADF) detector of “Zn-O-Al” spent catalyst in stainless steel reactor. The picture shows carbon filaments that grew from a nanoparticle. Elemental analysis (with EDX detector) reveals that this particle is made of pure iron and is likely coming from the pipes as no iron was detected on fresh catalysts. (C) STEM-EDX elemental mapping of “Zn-O-Al” spent catalyst in quartz reactor. In opposition with the previous case, no carbon filament were spotted. However, significant phase separation is observed as ZnO particles are spotted as well as some Zn-free zones around it. The aluminum seems to be still homogeneously dispersed. ....110

**Figure C.5:** Catalytic run in quartz reactor (550°C, 50 mL/min, 30% propane, 1 atm, 100 mg of catalyst). The data in black are the catalytic results showed in the main text and serves as a reference for the blue and pink one. In blue is the catalytic behavior of “Si-O-Zn-O-Al” when trimethyl methoxysilane was used as a precursor without the presence of pyridine. The match with “Zn-O-Al” behavior suggests that no silicon attached during the procedure. The pink data shows “Si-O-Zn-O-Al” catalyst when trimethyl chloride silane was used a precursor. The match with the “Al-O-Zn” behavior indicates that only one of the two zinc remain and it is unlikely that any silicon attached the surface.....111

## List of Tables

<b>Table A-1:</b> STEM-HAADF analysis of overcoated catalysts by 30 cycles with 0.5, 1 and 2 aluminum sec butoxide monolayers per cycle. ....	85
<b>Table A-2:</b> ICP OES analysis of samples collected during furfural hydrogenation (after concentration). ....	85
<b>Table A-3:</b> Parameters for furfural hydrogenation control experiments. ....	85

## List of Equations

<b>Equation A-1:</b> relative standard deviation.....	85
<b>Equation A-2:</b> irregularity factor .....	85
<b>Equation A-3:</b> Weisz-Prater criterion.....	86
<b>Equation A-4:</b> Wilke-Chang equation for bulk diffusivity .....	86
<b>Equation A-5 :</b> solute over pore diameter size ratio.....	87
<b>Equation A-6 :</b> relative coefficient of diffusivity.....	87
<b>Equation A-7 :</b> Effective diffusivity.....	87
<b>Equation A-8 :</b> observed rate of reaction.....	87
<b>Equation A-9 :</b> surface observed rate of reaction .....	88
<b>Equation B-1:</b> Antoine Equation.....	100
<b>Equation B-2:</b> Stokes-Einstein equation .....	101
<b>Equation B-3:</b> (2) Schmidt, (3) Sherwood and (4) Reynolds numbers .....	102



# Chapter 1 Introduction

The goal of this first chapter is define the principle concepts that underlie this thesis to introduce the essential framework of my project. First, I will describe the main features of heterogeneous catalysts: their function, their nature, and their structure. Then I will describe how the structure of catalysts can evolve throughout the preparation of the material and under reaction conditions. Finally, I will explain what atomic layer deposition (ALD) is and how it is used in heterogeneous catalyst preparation.

The second chapter presents a new method, created in our lab, which set the groundwork for liquid-phase ALD. This Chapter was adapted from a study published in *Applied Catalysis B* and introduces a new tool that enables layer-by-layer growth of metal oxide overcoats in liquid phase. These overcoats could be used for improving heterogeneous catalyst stability in the context of biomass conversion.

The third chapter describes a method developed for liquid-phase ALD and presents examples of several prepared materials. I also discuss some mechanistic insights gained into the method. Emphasis was put on the scalability, flexibility and ease of using this new method for catalyst overcoating. The Chapter is adapted from an article recently published in *Advanced Materials*.

The fourth chapter presents an underused potential use of ALD for catalysis: the growth of multinuclear clusters. The point of this work was to demonstrate that liquid-phase ALD could be used as unique tool for designing heterogeneous catalysts atom by atom, which could create new opportunities to understand the role of different, clearly-defined active sites in catalysis.

## 1.1 A brief overview on catalysts and catalysis

Catalysis is as an important chemical phenomenon with colossal economic implications. The term “catalysis” is attributed to the Swedish chemist Berzelius (1779-1848)<sup>[1]</sup> and describes the acceleration of a chemical reaction by the presence of an external chemical moiety that is not consumed by the reaction.

One way to comprehend the consequences of catalysis in our daily life is to realize that catalytic processes transform crude oil into plastics, textiles, cosmetics, fuel, food additives and dyes. Most readers will be in close proximity with something that has been catalytically transformed as they read these lines. Petrochemistry relies massively on catalysis and provide us with many everyday items, but this is clearly not the only field of application. For instance, the catalytic production of ammonia allows the production of fertilizer, necessary for global agriculture. Catalysts are also present in fuel cells, enabling emerging electric vehicle technologies as well as in pharmacological production, assisting the synthesis of drugs. Finally, catalytic reactions are also happening continually in our bodies.

Catalysts can be classified into three categories: homogeneous, heterogeneous or enzymatic. Homogeneous catalysts are active molecules that react with a substrate in the same phase as itself and are

typically liquid. Heterogeneous catalysts are solids that react with molecules in a different phase. Enzymatic catalysts are called enzymes and catalyze biochemical reactions. Considering that enzymes are macromolecules, one can argue that enzymatic catalysts fit in the description of homogeneous one. From my perspective, enzymatic catalysis is a completely separated system as the macromolecule, usually surround the substrate prior to reaction, setting up a local environment, very different from the bulk phase.

This thesis presents new tools and methods for preparing nanostructured solids for heterogeneous catalysis.

## 1.2 Structure and chemistry of heterogeneous catalysts

### 1.2.1 Components of heterogeneous catalysts

Heterogeneous catalysts are often made of two main components: the active material and a support. The active material is the moiety where chemicals adsorb and react, while the support facilitates the stability, activity, recyclability and macro-structure of the catalyst. Commonly, heterogeneous catalysts can be depicted as nanoparticles of active material, stuck on the walls of porous supports. However, self-standing nanoparticles or active supports can also be used as catalysts.

Typically, redox reactions are catalyzed by transition metals (e.g. Ni, Cu, Fe, etc.), noble metals (e.g. Pt, Ru, Au etc.) and, in some cases, reducible metal-oxides (e.g. CeO<sub>2</sub>, V<sub>2</sub>O<sub>5</sub>, etc.)<sup>[2,3]</sup>. For several reactions, noble metals are often more active and more stable than transition metals but they are also far less abundant and more expensive. Their high activity can sometimes be an issue if they further catalyze a targeted intermediate product to another unwanted molecule. The supported metal usually makes up 0.5 to 10 wt% of the catalyst (i.e. the loading). In the case of noble metal, this can be as low as 0.025 wt% while in case of transition metal the loading can reach 30 wt%<sup>[4,5]</sup>. The efficiency of a catalyst preparation is often related to its metal dispersion. Dispersion is defined as the ratio of the surface metal atoms over the total atoms of a given material. Considering that the reaction happens at the surface of the active material and that the material's cost is proportional to its total number of atoms, the dispersion is often proportional to the activity of a catalyst over its cost. Hence a higher dispersion is almost always preferred.

Acid-base reactions are catalyzed by materials bearing functionalities such as hydroxyl groups for Bronsted-type reactions or under-coordinated metal atoms for Lewis-type reactions<sup>[3]</sup>. Often these catalysts are metal oxides, which intrinsically have hydroxyl groups that can be acidic or basic. However, acid-base catalyst also include acidic polymers such as Nafion or Amberlist<sup>[6]</sup>. The acidity of solids is defined by their point of zero charge (PZC), which is the pH at which the surface is neutral. For example, silica is considered acidic (PZC around 2) while magnesia is considered basic (PZC around 10)<sup>[7,8]</sup>. Specific acids or bases like amines<sup>[9]</sup> or sulfonic acids<sup>[10]</sup> can also be grafted onto the surface of a catalyst which leads to bifunctional materials with antagonist functions (e.g. silica supporting both acidic and basic functional groups)<sup>[11]</sup>. In cases of reaction catalyzed by acid-base materials, the support is often catalytically active without the need for additional supported components.

The support is arguably as important as the active material. As its name indicates, one of the support's roles is to physically support the nanoparticles of active material. However, the support can also play

an important role in the catalytic reaction, by creating unique active sites at the metal-support interface. On a larger scale, the support also provides the macro-scale structure of a catalyst as is the case for structured catalytic beds within continuous flow reactors. More generally, supports can protect the active material against undesired phenomena that are detailed in the next section.

The choice of the support is often partially dictated by the price of the material, as this material accounts for roughly 90% of the total weight of the catalyst. Additionally, the support has to be stable under harsh working conditions. For instance, the support material has to be insoluble in the reaction media and capable of maintaining its structure under harsh temperatures and high mechanical stress. For these reasons, metal-oxides are extensively used, especially aluminosilicates. These are acidic materials made of three abundant and affordable elements—Si, O and Al—with extremely tunable structures, and high mechanical and thermal resistance. Other metal oxides such as titania ( $\text{TiO}_2$ ), zirconia ( $\text{ZrO}_2$ ) and ceria ( $\text{CeO}_2$ ) are also often used. In contrast to aluminosilicates, these metal oxides have redox properties that can be advantageously used to influence the catalytic properties of the active material or to run tandem reactions. However, the latter materials are more expensive and less easily tuned than aluminosilicates. Finally, carbon-based materials are also frequently used as supports. Their properties are drastically different from metal-oxides as there are far fewer surface functionalities. Because of the lack of surface functional groups, carbon materials are usually more inert. One of the great advantages of carbon supports is their electrical conductivity. For this reason, carbon is often chosen as a support for electrochemical catalytic reactions.

### 1.2.2 Unwanted modifications of heterogeneous catalysts components

Theoretically, a catalyst is supposed to be perfectly restored once the catalytic loop is closed, meaning that both activity and selectivity should remain constant with time. However, stability is almost never completely maintained during heterogeneous catalysis processes<sup>[12]</sup>.

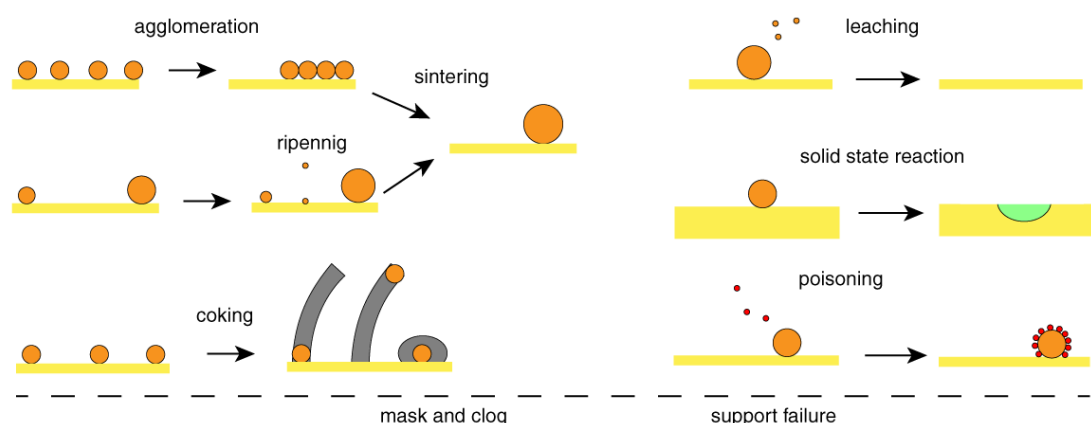
Deactivation occurs through chemical and physical phenomena and is exacerbated by elevated temperature. The main reason for deactivation is that heterogeneous catalysts are, by definition, thermodynamically unstable. Their reactivity comes from the fact that they have high surface energies relative to less catalytically active materials. Therefore, high energy processes will lead the catalyst to a more stable, hence less active, state. Deactivation phenomena are summarized in **Figure 1.1**.

Physical deactivation often refers to mechanical damages due to compression in a catalytic bed, but also includes sintering and agglomeration of the catalytic material. Such forms of deactivation can refer to both the active material and the support, although the mechanisms are different.

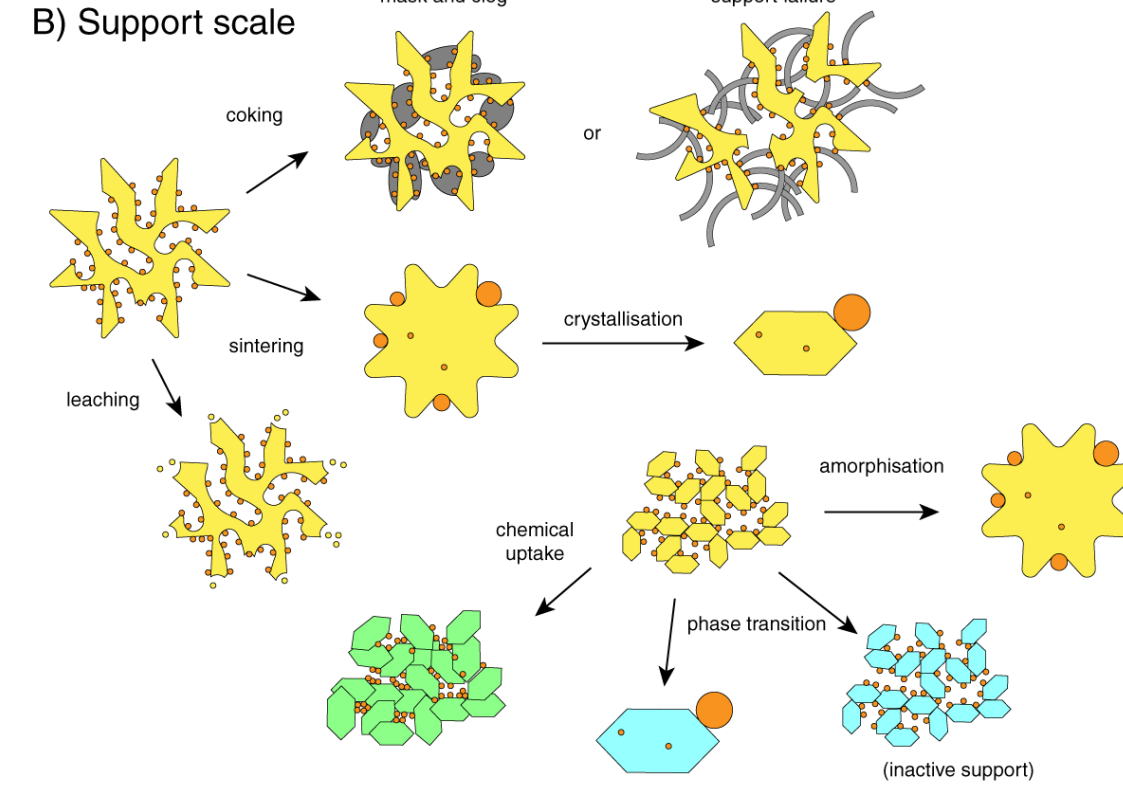
In the case of supported materials (oftentimes metals), high reaction temperatures promote the movement of particles until they meet and merge to make bigger particles through a sintering process (**Figure 1.1 A**). As the diameter of the active material increases, the dispersion and the productivity drop. Another mechanism of supported metal nanoparticle deactivation is known as Ostwald ripening<sup>[13]</sup>. This phenomenon involves a progressive migration of individual atoms from the smallest particles to the biggest. Both sintering and Ostwald ripening happen because of the high surface tension of metallic nanoparticles and the thermodynamic drive to minimize this surface tension. The smaller the particle, the higher the surface tension and the faster the agglomeration<sup>[14]</sup>. High temperatures also

cause support pores to collapse<sup>[15]</sup>, which leads to the trapping of active material or their expulsion to the external surface (**Figure 1.1 B**). Pores collapsing also decreases the support surface area, which increases the nanoparticle concentration and promotes their aggregation and sintering. This phenomenon is amplified by the presence of water as it stabilized mobile species and open oxo bridges<sup>[16]</sup>.

### A) Nanoparticle scale



### B) Support scale



### C) Reactor scale

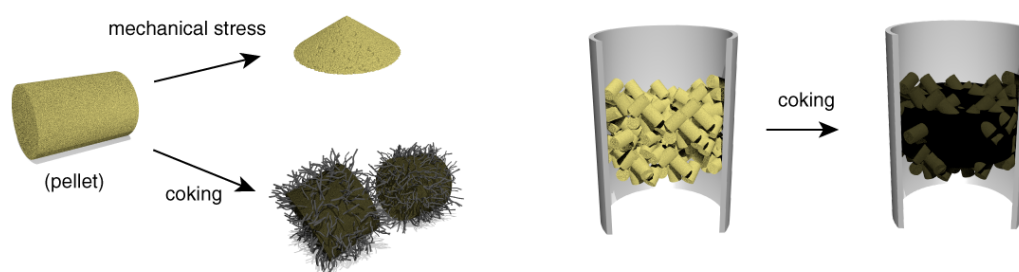


**Figure 1.1:** Summary of frequent deactivation phenomena visualized at different scales. The active nanoparticles are represented in orange, the support in yellow and carbonaceous deposits in grey.

Another mechanism for thermal deactivation of the support is crystallization<sup>[17]</sup>. This mechanism can affect both amorphous and crystallized materials. Elevating the temperature facilitates the movement

of atoms, facilitating their rearrangement into a more thermodynamically favored configuration. Glasses are metastable by definition. Therefore, all amorphous metal-oxides can potentially undergo crystallization that would reduce their porosity (**Figure 1.1 B**). However, crystallized materials are not immune to this type of deactivation as most metal oxides can exist in several crystalline phases with only one being the most thermodynamically favored. For example, high temperatures promotes the shift from gamma to alpha alumina; the latter being mechanically less strong and hardly porous. Another example would be for titania, where redox properties are affected by the transition from anatase to the rutile crystal structure. Finally, the reverse phenomenon is also encountered. In the case of zeolites, hot steam promote the amorphization of the support (**Figure 1.1 B**), which leads to the loss of the advantageous pore structure and acidity that is created by the crystalline structure<sup>[18]</sup>.

Solid-state reactions between the support and the active material can be categorized in between physical and chemical deactivation. Here again, the use of high temperature is the main trigger of these phenomena. Depending on the case, active species might diffuse into the bulk of the support or form an inert material (**Figure 1.1 A**) or expand it to promote pore closing (**Figure 1.1 B**).

Chemical deactivation can be classified in three ways. The first category of processes is known as poisoning. In such cases, a molecule that is present in the feed binds more strongly to the active site than the targeted substrate (**Figure 1.1 A**). In this case, the active site is no longer available to treat the incoming substrate and is considered to be poisoned. Example of poisons are sulfur compounds for transition metal nanoparticles<sup>[19]</sup>, alkaline ion for Bronsted acid sites<sup>[20]</sup> or transition metals for noble metal nanoparticles<sup>[21]</sup>. The second deactivation category results from the catalysis of undesired reaction. In this case, the transformed molecules are further catalyzed and react more than once, crosslinking with their neighbors. This process results in the growth of polymeric carbonaceous species with various structures (**Figure 1.1 A and B**). They are referred as humins, coke, carbon filament, or char depending on the mechanism with which they are formed<sup>[22]</sup>. The growth of such polymers clogs pores, masks active sites, eventually breaks apart catalyst pellets and can increase the pressure drop in the catalytic bed until there is total plugging (**Figure 1.1 C**). Fortunately, carbonaceous species are easily burned off, restoring some degree of catalytic activity. The full capability of the catalyst can often not be fully recovered as the local heat produced by calcination leads to several physical deactivation processes (as previously described)<sup>[23]</sup>. Importantly, the presence of polymeric species fouling a catalyst does not necessarily come from further reactions involving products. In some cases, polymeric species come from impurities in the feed<sup>[24]</sup>.

The third category of chemical deactivation processes is the leaching of the active component or the support itself (**Figure 1.1 A and B**)<sup>[25]</sup>. This can happen in the liquid phase, when the solvent is polar enough to slowly dissolve a metal oxide by hydration of the cation<sup>[26]</sup>. Metal nanoparticles are also affected by chemical etching in acidic media (oxidation into soluble cation) or chelating media (complexation by an oxygenated molecule). Such deactivation is frequently observed in the field of biomass conversion as the solvent is often acidic water and the highly oxygenated molecules have strong interactions with the catalytic cations.<sup>[27]</sup> Gas-phase leaching can occur but is mainly an issue for metals with low melting points (e.g. Zn, Na), oxides with high vapor pressure ( $\text{RuO}_4$  and  $\text{PtO}_2$ ) and metals that form volatile species ( $\text{Ni}(\text{CO})_4$ ,  $\text{Fe}(\text{CO})_5$ ,  $\text{Ru}(\text{CO})_5$ ,  $\text{CuCl}_2$ )<sup>[17]</sup>.

## 1.3 Preparation of heterogeneous catalysts

### 1.3.1 Supports

Methods of support preparation vary significantly depending on which class of support is being prepared. I will focus here on the two main categories: metal oxides and carbon-based supports.

The preparation of metal oxide supports with high surface area relies on the decomposition and condensation of molecular precursors. A large number of techniques multiplied by an even greater number of synthesis parameters offers an infinite number of potential structures. In the scope of this introduction, I will briefly list the most common synthesis techniques for metal oxide catalysts.

*Flame spray pyrolysis* is a technique based on the dispersion of a metal precursor ( $\text{SiCl}_4$ ,  $\text{AlCl}_3$ ,  $\text{TiCl}_4$  etc.) sprayed through a flame (i.e. in a mixture of hydrogen and air)<sup>[28]</sup>. The precursors decompose in the presence of oxygen and hydrogen, leading to the formation of particulates of metal oxides. Although this approach limits the formation of pores, the particles are small enough to display a high enough surface area for catalysis<sup>[29]</sup>. A typical example of material prepared that way is the frequently-used  $\text{TiO}_2$  “P25” (**Figure 1.2 A**).

*Precipitation* is a milder approach that consists of the dissolution of salts at a controlled pH and temperature, followed by a change in one or multiple parameters, which reduces the solubility of the given salt. This procedure is usually done in an aqueous phase and offers many synthetic handles to tune the final structure of the material<sup>[29]</sup>. Nature of the solvent, of the precursors, of the acid catalysts, ratio of precursors, ageing and sub sequenced thermal treatments are examples of parameter that strongly influence the final material structure.<sup>[30–32]</sup>

*Organic sol-gel reactions* are performed using organometallic precursors in organic media. Typically a metal alkoxide is hydrolyzed and condensed in a very similar way to organic monomer polymerization<sup>[33]</sup>. This method offers even more degrees of freedom than the previous one but is also significantly more expensive. Organic ligand can be engineered adequately, a broad range of organic templates or catalysts can be used to assisted growth and help controlling the kinetic. Sol-gel is arguably the most accurate technique for rationally controlling the structure of the final metal oxide. A representative example would be the well-established method to form silica with an extremely narrow pore size distribution and organized structure called SBA-15 (**Figure 1.2 B**)<sup>[34]</sup>. In this case, a soft template made of well-organized micelles guide the silica growth. Chiral or imprinted metal oxides can also be prepared with a judicious choice of template<sup>[35,36]</sup>. Silica materials prepared by sol-gel represent an incredibly large family of nanostructured materials among which one can pick a material to fit one’s needs (**Figure 1.2 C**). Silica is not the only materials that can be prepared using such processes. Other materials such as alumina<sup>[37]</sup>, titania<sup>[38]</sup> or zinc oxide<sup>[39]</sup> are commonly made with these approaches. In sol-gel processes, the drying is also critical. As the solvent is removed, the pores can collapse. A distinction is made between a xerogel and an aerogel depending on whether the solvent is in a liquid or supercritical phase, respectively, prior to drying<sup>[40]</sup>.

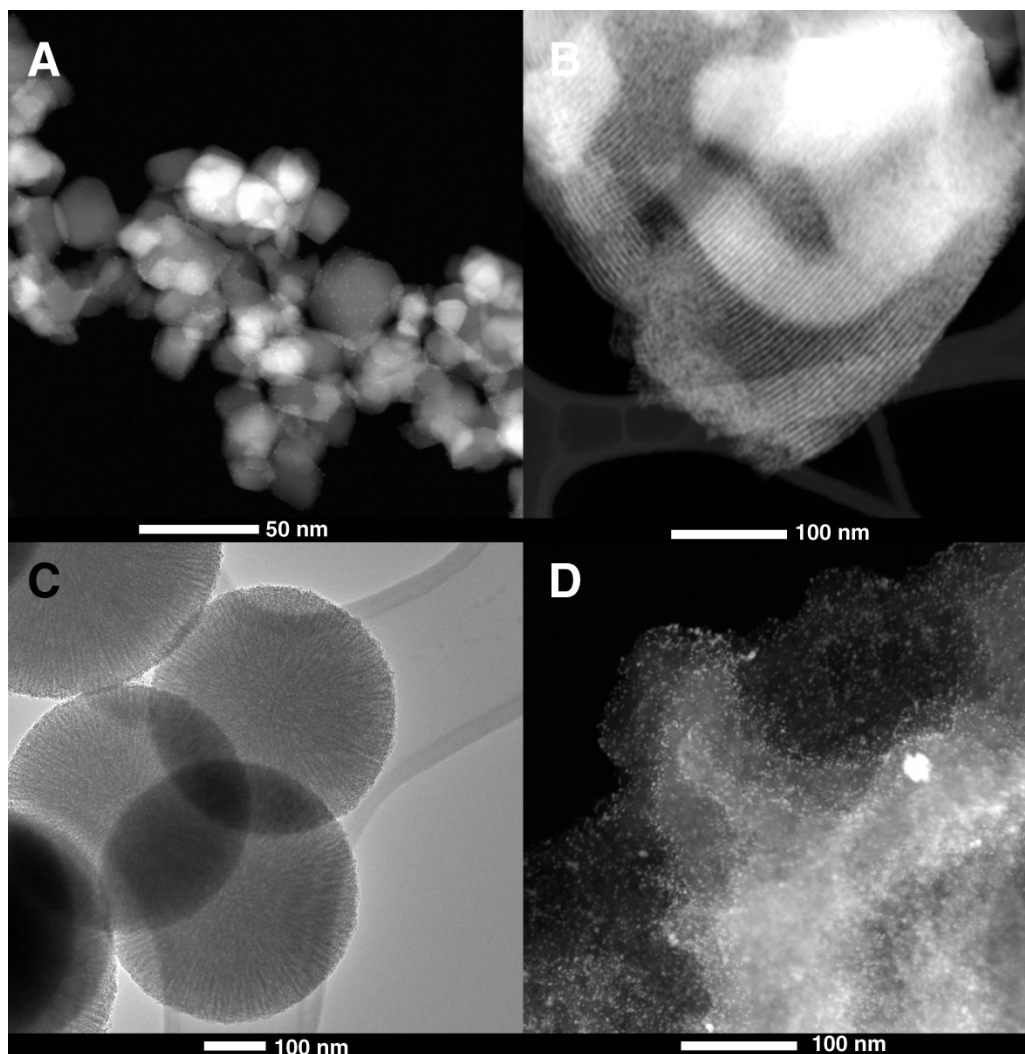


**Figure 1.2:** Scanning transmission electron microscopy images acquired with high annular angle detector and a bright field detector, representing various support structures. A) copper on  $\text{TiO}_2$  P25 (catalyst prepared by Dr. Yeap), B) home-made silica “SBA-15”, C) commercial silica “KCC-1” and D) platinum nanoparticles over carbon support (catalyst prepared by Dr. Questell).

Sol-gel reactions generally involve water as the oxygen source, but not always. Non hydrolytic sol-gel can be performed, for example, using an alcohol as the oxygen source<sup>[41]</sup>. These reactions are better categorized according to the ligand that they release.<sup>[42]</sup> For instance, reaction between an acetate precursor and an alkoxide one lead to the elimination of an ester. In a same way, reaction between alkoxide and a halide precursor releases an alkyl halide. Some routes form an intermediate hydroxyl group that will condense in a second step to form an oxo bridge but the direct formation of a bridge between two precursors is also possible. Interestingly, materials prepared by non-hydrolytic sol-gel can have different properties from those prepared hydrolytically. For instance, titania prepared by non-hydrolytic sol-gel methods is completely dehydroxylated while titania prepared by hydrolytic sol-gel is fully covered with hydroxyl groups<sup>[43]</sup>. Another example is the crystallization path that alumina follows upon thermal treatment. In case of preparation by a hydrolytic sol-gel method, alumina will go from pseudo boehmite to gamma alumina to delta alumina over a range of roughly one thousand degrees, while alumina prepared using the non-hydrolytic route can remain amorphous up to 900°C and then crystallize into gamma alumina<sup>[44]</sup>.



Finally, *hydrothermal synthesis* is a procedure in which all the ingredients are loaded into a sealed autoclave, generally with a Teflon liner to avoid corrosion, and heated at a high temperature. The mechanisms of reactions during the hydrothermal treatment are complicated to investigate, therefore less known. Parallel reactions such as precipitation/dissolution and topotactic transition are generally admitted to occur.<sup>[45,46]</sup> This process is used in the preparation of many catalytic crystalline materials among which we can cite the basic hydroxy apatite, the acidic zeolites and metal organic frameworks (MOF)<sup>[47–49]</sup>. Are concerned also, many oxides that can be prepared via other approach (e.g. ZnO, CeO<sub>2</sub>, TiO<sub>2</sub> etc.), the shape and size being highly dependent of the synthetic conditions.<sup>[50–52]</sup>

Carbon supports are widely used in electrochemistry due to their electrical conductivity. The great variety of structures goes far beyond the known allotropes (graphite, diamond, nanotubes, and fullerenes) and keeps expanding. Carbon supports are characterized by a particularly high surface area and low density compared to metal oxides. In practice, their ultra low weight can be inconvenient for handling but it makes the transmission electronic microscopy easier as the difference of density between the support and the nanoparticle lead to a better contrast (**Figure 1.2 D**). The principal preparation route is to pyrolyze a preformed carbon-based material or molecular precursor<sup>[53,54]</sup>. Both the nature and structure of the carbon source have a large impact on the final morphology and crystallinity of the support. Therefore a broad range of bio-sourced materials and artificial precursors have been pyrolysed<sup>[55]</sup> in order to explore new structures for more rational design<sup>[56]</sup>.

### 1.3.2 Nanoparticles

The active nanoparticles that are put on the previously reviewed structures are usually intrinsically unstable because of their high surface energy. Therefore, strategies have been developed to target and maintain their small size during preparation. First let's consider unsupported nanoparticles. In this case, the most commonly used means of preparation is called “colloidal synthesis”<sup>[57]</sup>. Many variations of this strategy exist depending on the material and final structure targeted, but they all rely on separation in time of nucleation and growth steps, facilitated by a protective agent such as a surfactant or bulky ion. The role of the protective agent is to slow down the growth and to keep the nuclei separated<sup>[58]</sup>. This agent can also favor the formation of a given surface structure over another. A very high number of nanostructures have been achieved using this type of method, demonstrating the breadth of atomic architectures currently available and providing very well defined model catalysts<sup>[59,60]</sup>. However, industrial applications of these materials has been limited as their preparation is expensive and their instability limits their long term use<sup>[61]</sup>.

The most common preparation used both industrially and academically is to grow nanoparticles on a support. During the preparation, the support helps limits nanoparticle agglomeration and also serves as a nucleation source since heterogeneous precipitation is always favored compared to homogeneous precipitation.

The basic principle of growth on supports is to add a solution containing dissolved salts to a support<sup>[62,63]</sup>. If the support is dispersed in a solvent, the method is referred to as “wet impregnation” while if the volume of solvent is just sufficient to fill the pore volume then it is considered “incipient wetness impregnation” (IWI). Next, the salt is precipitated from the solution, for example using a reducing agent or simply by evaporating the solvent. This method is also commonly used to load colloidal nanoparticles on a support.<sup>[64]</sup> The final step is a series of thermal treatments that turn the

precipitated salt into active nanoparticles. A calcination step is generally used to turn the salt into an oxide nanoparticle and also to burn off any organic ligand that might have been necessary in the previous step. In the case of metallic particles, a reduction step is performed, usually followed by a mild passivation to enable storage in aerobic conditions. Although the practical steps are relatively simple, the mechanisms of nanoparticle formation are extremely complex<sup>[65]</sup>. A great deal of effort has been made to optimize the interaction between the solubilized salt and the support surface. For instance, electrostatic interaction, choice of ligand, choice of solvent and all the properties of the support are key parameters that can notably be tuned to increase the dispersion of the final supported material<sup>[63]</sup>. As a general trend, noble metals are easier to disperse and more reducible supports better stabilize small nanoparticles<sup>[66]</sup>. However, non-reducible silica is frequently used because of the ease of producing this material with a high surface area, which decreases the surface concentration of nanoparticles and their tendency to agglomerate.

### 1.3.3 Single-atom catalysts

The heterogeneous community uses the term “single-atom catalyst” to describe isolated single active sites on the surface of a support formed by a single atom of a given material<sup>[67,68]</sup>. Within this review, three categories of single atom catalyst are distinguished: isolated cations, single-atom alloys and grafted homogeneous catalysts. Technically, acid sites in zeolites are isolated enough that they can be considered single atom catalysts. While such sites in zeolites are present in a vast number of catalysts, in practice, most people use the term “single atom catalyst” only for supported heteroatoms<sup>[69,70]</sup>.

The first category describes the presence of an active atom on a support with a coordination shell made only of the support or solvent (**Figure 1.3 A**). By analogy with homogenous catalysts, the support acts as a giant chelating ligand. The idea behind this strategy is to minimize the size of the supported nanoparticles. The dispersion then reaches 100%, meaning that the expensive part of the catalyst is fully utilized and metal-support interface sites are maximized. Several strategies to prepare such materials have been developed. I present here a few selected cases in order to illustrate the wide range of possibilities.

The most straight forward way of preparing an isolated ion on a surface is to use wet or dry impregnation, as described before, but at very low loadings (between 0.025 and 0.5wt%)<sup>[69,71]</sup>. Decreasing the metal loading increases the average distance between the atoms, diminishing the probability for them to meet and form nanoparticles. All of the previously described tools (electrostatic adsorption, precipitation etc.) can be used to promote efficient anchoring to the surface<sup>[72,73]</sup>.

Another approach is to decompose an existing catalyst<sup>[74]</sup>. For instance, gold nanoparticles supported on ceria can be carefully leached so that the Au-Au breaks but not the Au-O bond at the metal-support interface. After washing, only gold atoms that are strongly bonded to the surface remain.

As was demonstrated in several studies, ceria can efficiently stabilize single atoms and can be used for atom trapping. For instance, Jones *et al.* prepared single atom of platinum on ceria in two steps. First they prepared platinum nanoparticles supported onto alumina. Then, they physically mixed it with cerium oxide and heated up the whole thing. Due to the high temperature, volatile species of platinum flew from the alumina to the ceria.<sup>[75]</sup> The final material consisted of atomically dispersed

platinum on ceria. Such phenomenon of re-dispersion is particularly tricky to track and depending on the cases can be beneficial or detrimental<sup>[76]</sup>.

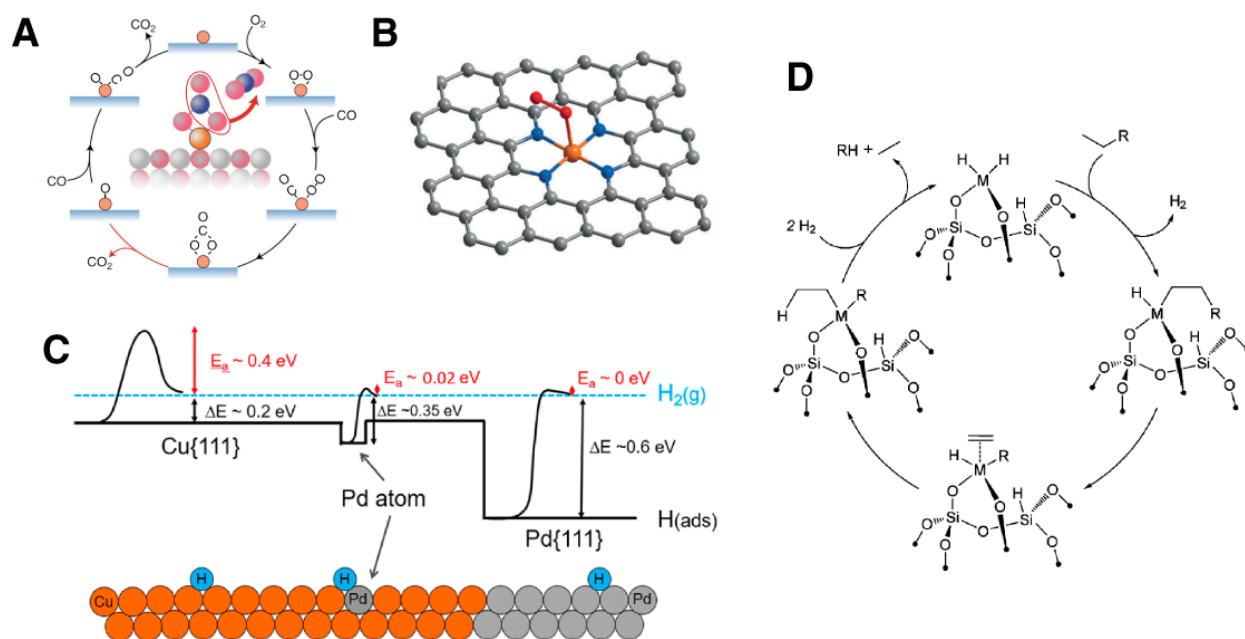


**Figure 1.3:** Examples of single atom catalysts (SACs). A) Ligand-free single atom Pt on alumina, B) Iron atom integrated in the structure of a carbon support, C) single atom alloy of Pd in Cu and D) Organometallic complex grafted on a silica surface. All figures were reproduced with permission from publishers<sup>[77–80]</sup>.

Single atoms can also be integrated directly into the bulk of the support. In this strategy, the active atom is present in the precursor mixture of the support and integrates as the support itself forms. This is the case for a co-precipitation procedure where salts of the active species and support precursor are precipitated together<sup>[81]</sup>. Similarly, for wet impregnation, low loadings can be used to create a final material with homogeneously dispersed atoms as opposed to a biphasic mixture of the active components and the support. Crystalline zeolites containing tin atoms in their framework have notably been successfully prepared and used in several reaction including for biomass conversion<sup>[82,83]</sup>. Platinum-containing FeO<sub>x</sub> have also been prepared and used for the selective reduction of nitroarenes<sup>[84]</sup>. The dispersion of an active atom into the bulk of a material can also be achieved by pyrolysis of an organometallic compound, forming a carbonaceous, porous materials with an integrated active metal<sup>[85,86]</sup> (**Figure 1.3 B**). Finally, isolated active sites can also constitute the main structural component of a material as is the case for metal organic frameworks (MOFs) where nodes of the repeating unit can be catalytically active<sup>[87]</sup>.

Single-atom alloys (SAAs) is a very diluted solid solution of one active metal into a less active one. For example Pd atoms diluted into a Cu phase (**Figure 1.3 C**). SAAs represent a small minority among the many examples of single atom catalysts. Despite displaying interesting catalytic properties and being relatively easy to prepare<sup>[88]</sup>, their characterization is particularly challenging as the metal loading in heterogeneous catalysis is low and the ratio of active metal over total metal has to be low too, leading to an extremely diluted system. Mechanistic studies usually rely on preparation and analysis in an ultra-high vacuum (UHV) environment, using a well-defined plan of metal as a support on

which active metal is deposited by soft landing, in order to clearly separate the various concomitant effects<sup>[78,89,90]</sup>.

The final category of single-atom catalysts that is discussed here corresponds to grafted homogeneous catalysts (**Figure 1.3 D**). The strategy is to take functioning homogeneous organometallic catalysts and to graft them on a surface in order to combine their advantages with those of a heterogeneous system (e.g. usually increased stability and recyclability). Their preparation is very similar to the first case of grafting isolated atoms, but this time, the aim also includes preserving the carefully chosen ligands that will influence the reaction.

The most frequently used procedure is to take an organometallic complex with one or several hydrolysable ligands and to solubilize it in an organic, aprotic, dry solvent. Then, this solution is added to a metal oxide (usually silica) that has been thermally pretreated before use. The complexes will be anchored to silica hydroxyl groups by hydrolytic condensation, releasing a sacrificial ligand. The excess complexes are washed off and the catalyst is dried more or less harshly depending on the desired final structure. Comprehensive reviews of procedures and lists of organometallic precursors are regularly published and can be found elsewhere<sup>[80,91–93]</sup>. The thermal pretreatment of silica is particularly important to ensure isolation of the atoms. As mentioned previously, the grafting reaction happens on the hydroxyl group of the metal oxide. Typically, metal oxides have between five and nine hydroxyl groups per square nanometer<sup>[94–96]</sup>. If such a concentration of complexes were actually reached (which is unlikely due to steric interactions), it would be impossible to discriminate between properties coming from individual metal atoms and the ones coming from intermetallic interactions. Also, significant deactivation would become likely as the metals would tend to rapidly form nanoparticles under most reaction conditions. Silica is a good choice of support for studying grafted organometallic compounds as its hydroxyl density can be lowered from 4.6 OH/nm<sup>2</sup> to below 1 OH/nm<sup>2</sup> by thermal treatment in vacuo<sup>[97]</sup>, minimizing the probability of having two neighboring complexes. In a sense, one can visualize this grafting procedure as the deposition of a monolayer of metal complexes on a surface.

#### 1.4 Atomic Layer Deposition for heterogeneous catalyst preparation

Atomic Layer deposition (ALD) has recently been used for the preparation of novel heterogeneous catalysts and will be a key subject of this thesis. Specifically, ALD is a method for growing thin films molecular layer by molecular layer by grafting of organometallic precursors. ALD is a specific case of chemical vapor deposition (CVD) that is almost exclusively performed in gas phase at low pressure and at high temperatures. Most of ALD's applications are in the micro-electronics field where the deposition of thin layers with atomic accuracy allows the preparation of small components such as gate oxides for Metal Oxide Semiconductor Field effect transistor (MOSFET) and Dynamic Random Access Memory (DRAM) capacitors<sup>[98,99]</sup>. The key feature of this technique, as will be discussed more extensively below, is the self-limited nature of the deposition reaction, which limits the growth to one atomic layer at a time ensuring control and uniformity of the layer. Multilayer growth is performed simply by repeating the deposition cycle to reach the desired film thickness.

Given the extremely high level of accuracy accessible by ALD and the constantly growing library of materials that can be deposited, researchers have started to use ALD for other applications than micro-

electronics. Notably, the potential of ALD is being investigated for the design of solar cells, batteries, fuel cells, sensors, membranes and, as previously mentioned, heterogeneous catalysts<sup>[100–103]</sup>.

#### 1.4.1 Chemistry of ALD

As previously mentioned, ALD deposition proceeds through cycles (**Figure 1.4**). A substrate, generally a wafer, is placed into a reactor under reduced pressure ( $< 1$  Torr) at a temperature usually ranging from 150 to 350 °C. A continuous flow of inert gas flushes any adsorbed species from the surface and the cycle starts. The first step (or first half cycle<sup>[104]</sup>) is a pulse of precursor, (“A”). This precursor reacts irreversibly with the substrate surface and cannot react with itself. During this step, adsorption sites are gradually consumed until full coverage is achieved. At this point, the excess of A in the gas phase or physisorbed at the surface is purged out by a flow of inert gas. The second step (or second half cycle) is a pulse of counter-reactant (“B”). B can react with A but not with itself. Hence, B will react with each A on the substrate surface until a complete layer has been deposited. In the same way as before, not more than one monolayer of B can be deposited and the excess is purged from the reactor. After the second cycle, the surface is ready to accept another layer of the initial precursor (A). Repeating the cycle leads to the formation of ABABAB layers with a thickness directly proportional to the number of cycles. The chemical composition is controlled by wisely choosing A and B and, if needed, a third reactant C<sup>[105]</sup>.

The example of alumina deposition also highlights the narrow process requirements that are often required for ALD. Even if the reactions are self-limited, the ALD chemistry can be performed only within a specific temperature window<sup>[106]</sup>. At too low of a temperature, chemicals might condense as a liquid on the substrate, forming more than a monolayer. Low temperatures could also lead to a low concentration, if not absence, of reactant in the gas phase. In some cases, a high temperature is needed for the chemical reaction to proceed. However, when an excessively high temperature is used, the compounds can decompose on the surface, leading to thicker and/or uncontrolled growth. In case of the TMA/water reactants, the side product (or released ligand) is the very inert methane, which is easily removed. In some other cases, the behavior of the ligand (chemical bonding to the surface, low volatility, decomposition) can lead to further issues. For instance, chlorinated precursors can lead to halogen transfer to the surface. Depending on the desired degree of control over the thickness of the deposited layer, one can choose to work at higher pressure than usual. This approach is referred to as “atmospheric pressure ALD”. The advantages include lower cost of equipment as well as faster diffusion of the reactants. However, the difficulty of desorbing unreacted species often leads to longer purges or higher growth per cycle<sup>[107,108]</sup>. To summarize, a major challenge in ALD is the choice or design of suitable reagents. Past and continuing progress in this area enables the deposition of an expanding number of materials.

The most common example used to describe an ALD cycle is the deposition of alumina using trimethyl aluminum (TMA) as a precursor and water as a counter-reactant<sup>[109]</sup>. In this case, neither TMA nor water can react with itself but they can react together through the same acid-base reactions involved in sol-gel reactions. Interestingly, TMA was one the first precursor used in alumina sol-gel chemistry. Both hydrolysis and condensation lead to the formation of methane that is removed during the purge stages.

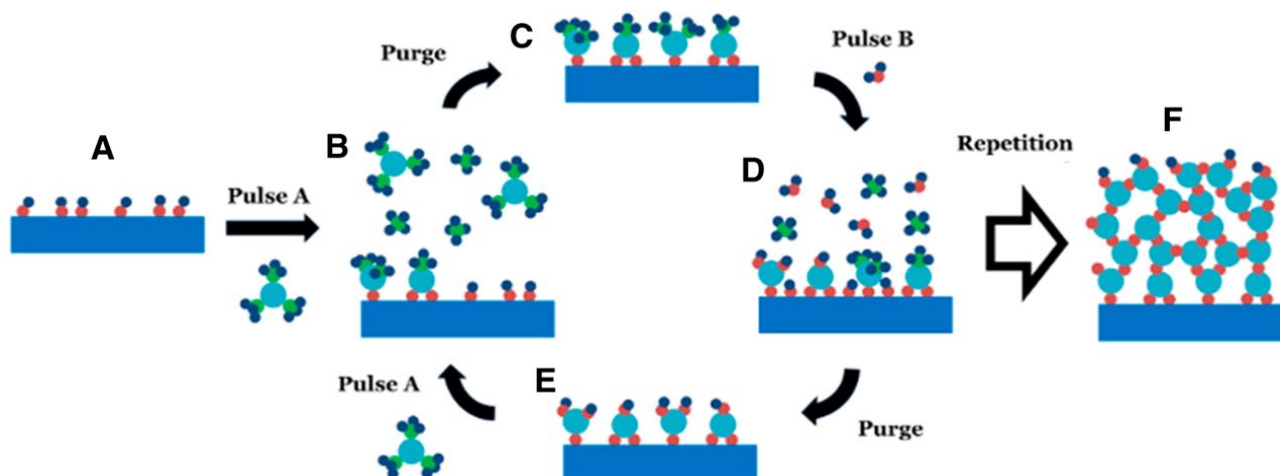


**Figure 1.4:** Description of the ALD cycle for alumina deposition on hydroxyl-bearing surface. A) the surface is covered with reactive hydroxyl groups. B) Precursor A, here trimethyl aluminum, is injected and saturates the surface. C) The excess is purged out, with the only remaining A being on the saturated surface. D) The counter-reactant B, here water, is injected and reacts with the surface. E) The excess is purged leaving a surface that is ready for a new cycle. The repetition of this cycle produced a film as represented on F). The figure has been adapted with the permission of the publisher<sup>[110]</sup>.

For the metal precursor, efforts have focused on designing the chelating ligand, which offers many possibilities. In comparison, modifying the counter-reagent is often more difficult. For oxygen addition, principle precursors include water<sup>[111]</sup>,  $O_3$ <sup>[107]</sup>,  $O_2$ <sup>[112]</sup>,  $O$ <sup>[113]</sup> (plasma) and peroxide<sup>[114]</sup>. The deposition conditions are often suitable for the use of a plasma to boost reactivity, especially of oxygen species<sup>[115]</sup>. Beyond oxides, other materials such as nitrides, sulfides, phosphates, metals are also prepared using, respectively, ammonia<sup>[116,117]</sup> or hydrazine as a nitrogen source, hydrogen sulfide<sup>[118–120]</sup> as a sulfur source, trimethyl phosphate as a phosphate source<sup>[121]</sup>, and  $H_2$ , formalin or  $O_2$  to consume the ligands<sup>[122–125]</sup>. ABC cycles where B needs to be activated to react again or to facilitate the deposition of ternary compounds are common<sup>[126]</sup>. The deposition of hybrid organic/inorganic materials, referred to as molecular layer deposition (MLD), is performed in exactly the same way. The only difference is the use of a bifunctional organic counter-reagent instead of water. Typically, ethylene glycol would react with trimethylaluminum to form an alucone<sup>[127]</sup>. The growth of fully organic layers is also possible using reactions developed in polymer science<sup>[128]</sup>. The advantage of MLD versus ALD is a better control of the structure of the final material. The utilization of organic reagent allows, for example, the formation of pores<sup>[129]</sup>. The presence of organic linkers also facilitates the preparation of non-stoichiometric oxides and doped oxides. This was notably used in the preparation of photoactive  $TiO_2$ <sup>[130,131]</sup>. Finally, ALD and MLD were performed in alternating sequences on some materials to combine properties such as wettability and stability<sup>[132]</sup>.

While ALD is designed for continuous film deposition, some parameters can influence the morphology of the deposited material and ultimately lead to the formation of atomic “islands” or nanoparticles<sup>[133]</sup>. Typically, a low surface density of reactive groups will favor the formation of nuclei that can eventually merge into a film<sup>[134]</sup>. Noble metal deposition on metal oxides often suffers from a significant delay in the formation of a film, whereas immediate coverage can be achieved if the surface is metallic<sup>[122,135]</sup>. In other words, the use of an ALD set-up does not ensure the deposition of a conformal film, free of pinholes, cracks and impurities. Active research is dedicated to the detection

and elimination of such defects as the quality of microelectronic components can be strongly related to the permeability of each insulator involved<sup>[136]</sup>. The quality of the layer depends on the temperature of deposition, nature of substrate and precursors involved<sup>[137–139]</sup>. Since the fields of microelectronic and heterogeneous catalysis have different material requirements, structures that are typically avoided in the first field can be advantageously used in the latter.

#### 1.4.2 An overview of ALD utilization in heterogeneous catalysis

##### *Protective shell*

In recent years, ALD has been used as a method to overcoat catalysts. Overcoating involves taking an existing working catalyst and to cover its surface with a thin film. In doing so, the stability can be greatly improved and, in certain cases, the reaction can be tuned. In some cases, a thin overcoat has helped anchor nanoparticles to their position, which prevents them from sintering. For instance, studies have demonstrated that a few layers of alumina prevented sintering of Cu<sup>[140,141]</sup>, Au<sup>[142]</sup>, and Pt<sup>[143]</sup> supported nanoparticles. The proposed stabilization mechanism involves the covering of undercoordinated atoms, reducing their mobility<sup>[140]</sup>.

An overcoat has also been shown to prevent coking during dry reforming of methane with Ni<sup>[144]</sup> and Pd catalysts<sup>[145]</sup> (**Figure 1.5 A**). In the case of the Pd catalyst, the deposited metal oxide was grown amorphously and heated until crystallization. As a consequence, pores opened in the oxide overcoat, allowing the nanoparticle access to the reaction media. Critically, the pore size was small, preventing the existence of excessive neighboring active sites on the metallic surface, hence limiting polymerization. Additionally, ALD metal-oxide overcoats also protect against leaching<sup>[140]</sup> (**Figure 1.5 B**). The most reactive atoms have been suggested to be are the most likely to leach and are thus preferential adsorption sites for ALD precursors. In the first stages of undercoordinated atoms that were weakly attached becomes securely anchored. Enveloping titanium oxide with a layer of alumina has been shown to delay the phase transition from anatase to rutile<sup>[140]</sup>. The displacement of atoms is presumed to be constricted by the oxide shell. A similar effect has also been demonstrated in the case of iron oxide protected by alumina and silica<sup>[146]</sup> (**Figure 1.5 C**). In a last example, a protective layer of zirconia over ceria-supported palladium catalysts was demonstrated to be an efficient barrier against the sulfurization of the support<sup>[147]</sup>.

##### *Selectivity enhancer*

Beyond stability, ALD has also shown to be a convenient way to tune catalyst selectivity. Several strategies have been used to achieve this objective. For instance, a low number of cycles will form an overcoat that only partially covers a supported nanoparticle. In this case, the first atoms covered, typically at the corner and edge sites, are deactivated. Because of their low coordination number, these atoms often present a different reactivity (and selectivity) than the atoms on the nanoparticle's facets. After coating, only the atoms on the facets that are chemically equivalent remain accessible and produce the same product<sup>[148]</sup>. Another strategy is to use a template to preserve access to an active material. A subsequent deposition of a metal oxide proceeds anywhere but on the template (**Figure 1.5 D**). After removal of the templating agent by calcination or with an ozone treatment, a pore is formed that can act as a molecular sieve, with a size related to the original template<sup>[149]</sup>. Another

method to introduce porosity with sieving properties is to use a molecular layer deposition (MLD) approach<sup>[127]</sup>. The principle is the same as ALD but uses sacrificial organic linkers during the deposition that are burnt off in order to leave a targeted porosity. Selectivity between linear and cyclic alkene hydrogenation has been reported using such a strategy<sup>[150]</sup>. Hong Yi et al. also reported an enhancement of selectivity when using an ALD-deposited overcoat. In their case, the alumina was crystallized after deposition and the selectivity switch was attributed to the difference of diffusion within the pores<sup>[151]</sup>. Finally, selectivity can also be tuned by decorating active nanoparticles with a metal oxide. For example, the deposition of a nickel oxide island on top of a platinum nanoparticle modified the electronic properties of the metal, changing its selectivity<sup>[152]</sup>. In general, the possibility to precisely deposit an oxide on top of a metal is very versatile avenue to tune the electronic property of any given metal<sup>[153,154]</sup>. This type of structure is referred to in the literature as an “inverse catalyst”<sup>[155]</sup>. These structures can be compared to the sites formed via Strong Metal Support Interactions (SMSI)<sup>[156]</sup>. Usually, SMSI are observed in the case of metal nanoparticles on a reducible support<sup>[157]</sup>. The interaction between the two materials is so favorable that at high temperature the support will partially cover the nanoparticle, altering the reactive sites<sup>[158–160]</sup>. A very similar nanostructure is obtained by ALD without applying harsh thermal treatment<sup>[161]</sup>. Overall, ALD has proven to be a particularly efficient deposition technique of a promoter on an active phase by facilitating their interaction<sup>[162]</sup>.

Changes in selectivity with using ALD have not only been achieved with supported metal nanoparticles. As previously mentioned, bulk materials are often without any addition as acid/base catalysts. Therefore, ZnO, Al<sub>2</sub>O<sub>3</sub> and V<sub>2</sub>O<sub>5</sub> ALD have been used to tune the acidity of metal oxides notably for aluminosilicates, influencing their activity and selectivity<sup>[163–165]</sup>.

### *High surface area materials*

While atomic layer deposition not a well-suited material to create self-standing high surface area materials from scratch, it has been successfully used to bypass the difficulties of making porous materials that are recalcitrant to usual synthetic strategies for the preparation of high surface area supports. As mentioned previously, silica is extensively used in catalysis for its low price and the ease with which it can be prepared with various controlled nanostructures. Many other materials with interesting catalytic properties do not offer the same possibilities for synthetic control, often due to the high (or low) reactivity of their precursors. In an effort to transpose the accessible nanostructures of silica to other materials, ALD of titania, niobium oxide, tungsten oxide and zinc oxide have been performed on silica supports that had been synthesized prior to deposition to have the desired nanostructures<sup>[166–169]</sup>. High surface area alumina has also been used as a support for the deposition of CeO<sub>2</sub> and Fe<sub>2</sub>O<sub>3</sub><sup>[170,171]</sup>. In these cases, the authors emphasized that ALD was the only way to perform a conformal deposition without forming nanoparticles. This strategy does not apply only to binary metal oxides, which are well represented in the literature because their chemistry is better understood, but also to materials such as aluminum nitride on silica or ternary LaFeO<sub>3</sub> on MgAl<sub>2</sub>O<sub>4</sub><sup>[117,172]</sup>. The latter case represents an important example of ALD-enabled perovskite utilization in realistic catalytic conditions.



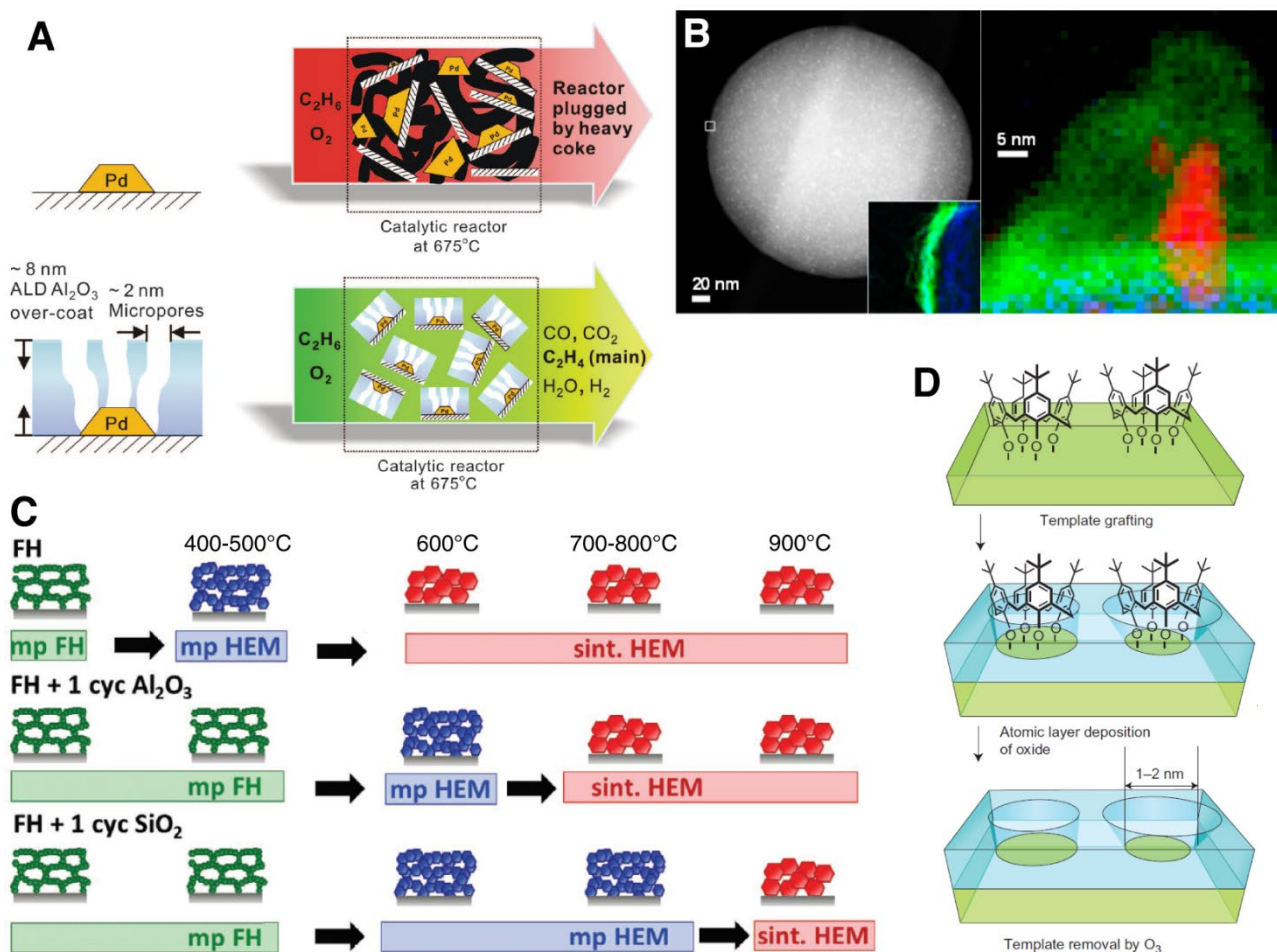


**Figure 1.5:** Examples of ALD utilization in the field of heterogeneous catalysis. (A) ALD was used as a protective overcoat on a supported Pd catalyst to avoid the formation of coke. (B) ALD was used to stabilize supported nanoparticles against sintering and the picture highlights the deposited layer surrounding the nanoparticle. (C) The scheme depicts an example where a thin overcoat stabilized a mesoporous material and prevented phase transition. (D) ALD is used with templating for improving the selectivity of the active surface beneath by creating a size-selective molecular overcoat. These figures were reproduced and adapted with the permission of the publishers<sup>[141,141,143,149]</sup>.

### Nanoparticles

Atomic layer deposition has also been useful specifically for active site preparation. Metallic nanoparticles can notably be grown by ALD with a very homogeneous spatial distribution and a narrow particle size distribution<sup>[173,174]</sup>. The size of the nanoparticles can be easily controlled as it is proportional to the number of ALD cycles. The narrow particle size distribution can increase for the stability the active material. As described previously, the driving force of Ostwald ripening is a disparity in particle size and this deactivation mechanism has been shown to be nearly absent when the particle size distribution is narrow<sup>[175]</sup>. Additionally, bimetallic nanoparticles can also be prepared by ALD, providing great control not only on the composition but also on the structure of the active site<sup>[176,177]</sup>. For instance, bimetallic core-shell, alloys with homogeneous or gradients of concentrations can be easily prepared<sup>[178]</sup>. Finally, the formation of nanoparticles and their metal-oxide shell can be performed within a single ALD process using an ABC sequence, promoting the nucleation of particles rather than their growth<sup>[179]</sup>.

## *Single Atom Catalysts*

As ALD relies on the grafting of organometallic precursors at each cycle, it is a natural candidate for use in the preparation of single-atom catalysts<sup>[180]</sup>. In contrast with previous cases, the preparation of SACs by ALD requires only one cycle. In other words, only one atomic layer is deposited. The ALD approach features the absence of other species such as solvents or counter-ions that can complicate the grafting. Chemically, the deposition occurs in a very similar way as single-site grafting using organometallic precursors in solution. The most common examples are palladium deposition onto partly oxidized carbon<sup>[181]</sup>, platinum on nitrogen doped carbon<sup>[182]</sup> and transition metals deposited on highly dehydroxylated silica<sup>[183]</sup>. More recently, the cycling properties of ALD were used to prepare isolated dimers made of one atom of Pt and one of Ru supported by nitrogen-doped carbon<sup>[184]</sup>.

### 1.4.3 The difficult transition from wafer to powder

The library of materials and structures deposited by ALD on wafers keeps expanding, driven by technological improvement of apparatuses and improved reactant design. However, ALD on high surface area materials and powders still remains mainly a deposition method for simple metal oxides and, increasingly, for metals, which are deposited on previously synthesized/engineered particles. The delay between the advances for microelectronics side and those for catalysis is largely due to difficulties in the transfer of methods from those designed for wafer substrates to those for powders.

Part of the difficulty is due to the ALD apparatus. For deposition on wafers, the reaction chamber is relatively simple (**Figure 1.6**). A wafer lies flat in a temperature-controlled chamber at low pressure. In the most common set-ups, there is an inlet and an outlet for the gases (reactive or not). Variations from one model to another rely on the position of these connections, influencing the direction of the flow (**Figure 1.6 A and B**)<sup>[185]</sup>. We also make a distinction between pumping reactors and purging reactors. In the first case, the excess of precursor is pumped out by particularly low vacuum while in the second case, it is mainly flushed out by an inert gas (still below 1 Torr). Since reagents A and B should not be mixed, precise and expensive electronic valves are used to keep reagents separate. In the case of wafers, a pulse length is typically on the order of a millisecond. To make ALD economically more attractive, an alternative approach has been developed based on spatial separation of the reagent rather than timed separation (**Figure 1.6 C and D**). In practice, reagents are both continuously feed to the substrate through several, spaced, inlets (one per chemical). The alternation of exposure is done by moving the substrate to the different zones or the sources on the substrate. Hence, a cycle is no longer defined by timed pulses but by a frequency of substrates moving through the chamber<sup>[186–188]</sup>.

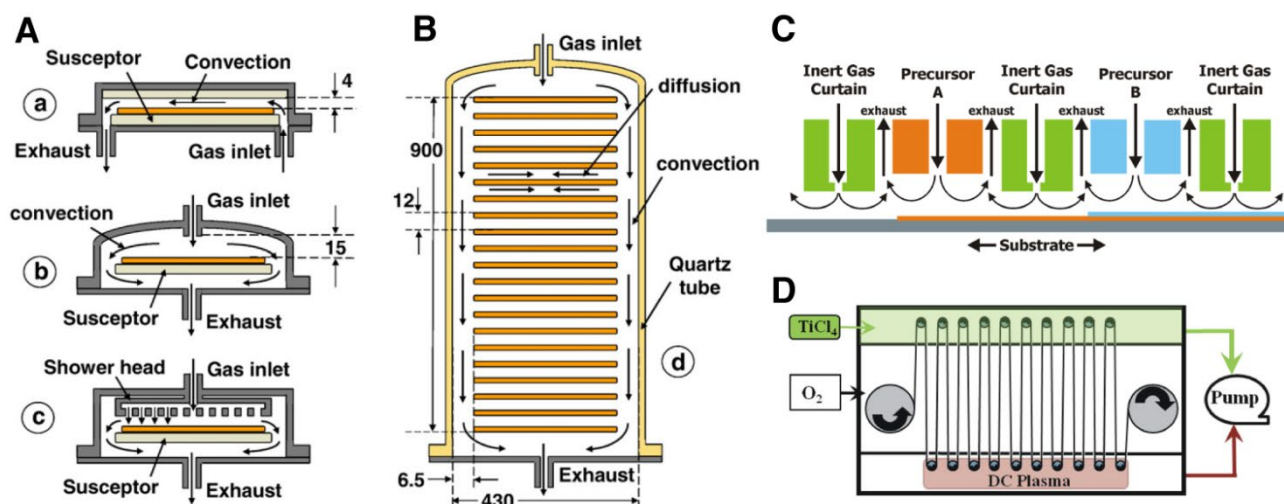


**Figure 1.6:** Example of ALD reactors for coatings on flat (wafer) substrates. (A) The most common reactor family for wafers where the main variation is in the position of inlet and outlet. (B) Batch ALD reactor where several wafers are loaded in same time. (C) Continuous ALD reactor with spatial separation of the processes, where the substrate moves from one zone to the next. (D) An alternate design of a continuous ALD reactor with spatial separation of the processes specifically designed for soft substrates that can be rolled from one zone to another. These figures were reproduced with the authorization of the publisher<sup>[185,186]</sup>.

When powders are coated, a whole new set of problems arises. First, flushing the powder with the gases is complicated. Blowing gas can lead to sample loss. Moving particles can lead the machinery to suffer from abrasion. Another issue is the agglomeration of the substrate. If the process is not specifically designed to avoid this, the deposition might envelope several particles, leading to losses in active surface, blocking of pores or to the powder turning into a large chunk of material. In the case of porous and high surface material, the diffusion of reactants can quickly become limiting and requires much longer pulses (up to several minutes). These long pulses are also needed to reach full coverage as the surface area to coat in the reactor is much larger compared to deposition on wafer and the feed rate of precursor is physically limited by the low pressure. Consequently, developing processes that ensure a full utilization of the expensive precursors becomes a key priority as wastes are potentially much greater<sup>[189]</sup>.

A series of ALD reactors have been developed for deposition on powders, each of them having their advantages and drawbacks. ALD on powder is not only being developed for catalysis, and even among the catalysis community, academia and industry do not have the same objectives. Therefore, the diversity in ALD reactors has mirrored the diverse objectives targeted by these various stakeholders.

To illustrate the challenge, one can consider calculations performed for a simple reactor with unstirred powder in a crucible, with gases flowing over the substrate<sup>[190]</sup>. The reactor could not be simpler nor less efficient. The authors considered a crucible (2 cm height, 5 cm diameter) containing nonporous silica powder (100 nm diameter) on which alumina was to be grown using TMA at 1 mbar (a typical ALD pressure). Under these conditions, 271 hours were required to reach full coverage of TMA. This time was mainly due to the diffusion time of TMA between the particles. This time can be reduced

to only 27 hours if the pressure is increased to 10mbar, but then other processing issues occur notably related to purging between cycles, the volatility of compounds etc.

To address these challenges, four main reactors (described in **Figure 1.7**) are used for ALD on powders: the fixed-bed reactor, the fluidized-bed reactor (FBR), the rotary reactor (and its derivatives), and the pneumatic (or spatial) reactor<sup>[191]</sup>.

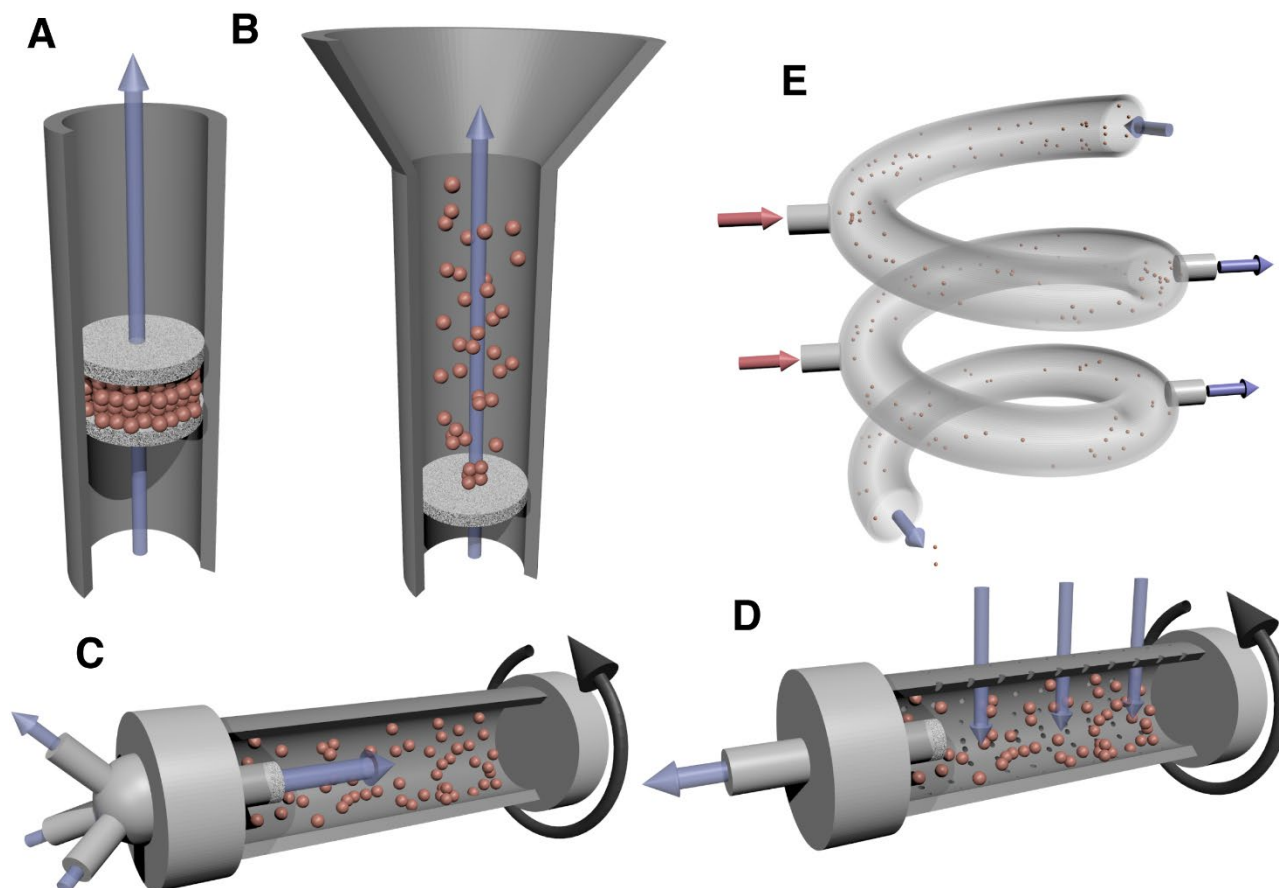


**Figure 1.7:** Different ALD reaction chamber configurations representing the different strategies for processing powders. (A) the fixed bed reactor, (B) the fluidized bed reactor, (C) the rotary reactor, (D) flow through rotary reactor and (E) spatial (or pneumatic) reactor.

*The fixed-bed reactor (Figure 1.7 A)* is a convenient method for lab-scale ALD on powder catalysts. The idea is to prepare the catalyst in the same reactor that will subsequently be used for catalysis. Such systems are generally home-made with valves that are opened manually. The powder is held in position by quartz wool plugs on either side, preventing its dispersion by the flow of gases going through. Overall, the system is not efficient as there is little control of the precursor consumption and the amount of substrate is generally small (milligram to gram scale). Still, this relatively simple system can be easily used to provide access heterogeneous catalysis labs to ALD without purchasing a full commercial apparatus.

*The fluidized bed reactor (Figure 1.7 B)* may be the most highly used and studied system<sup>[192–194]</sup>. Fluidization is a well-characterized phenomenon that is used at industrial scale for various catalytic applications. In this case, the fluidization of the particle that are to be coated greatly improves their

dispersion, limits their agglomeration and maximizes the mass transfer of the precursor through the bed. The agitation is generally assisted by mechanical stirring or a vibrator that shakes the overall reactor and helps induce fluidization. The powder is held in the reactor by a filter at the bottom and at the top (where sometimes only a simple enlargement of the tube is used to drop gas velocity and stop fluidization). Compared to the previous case, the FBR requires a dedicated and bigger set-up, but the quality of the overcoat is far better as the powder is agitated. A great deal of theoretical work has been done in order to maximize the separation of the particles and optimize the precursor use. Today, this system is arguably the most present in the industrial landscape.

*The rotary reactor* (**Figure 1.7 C and D**) is a system in which the powder is agitated by the rotation of the whole chamber<sup>[195]</sup>. One of the great advantages of this reactor is that it can be used in batch mode, maximizing precursor utilization independently of the kinetic of reaction. The reactants are added by pulses so that it is possible to calibrate the number of pulses needed to reach full coverage simply by tracking pressure variation. This technique has also been extended to plasma-enhanced ALD, facilitating the deposition of more challenging materials such as nitride<sup>[196]</sup>. Additionally, rotary reactors have been adapted for flow deposition. In this conformation, the gas enters through the walls of a rotating drum and is flushed out through a filter<sup>[197,198]</sup>.

*The spatial reactor* (**Figure 1.7 E**) for ALD on powders works on the same principles as reactors for wafers<sup>[199]</sup>. The system, free of expensive valves, is based on the continuous flow of reactants while the substrate is moving from one reactive zone to another. In the case of powder, the displacement of the substrate is performed by pushing it down a tube using a flow of gas. This tube contains zones where inlets are connected perpendicularly. The number of cycles is then defined by the length of the reactor. One additional cycle simply means one additional increment pipe. This type of reactor has only recently been developed and thus its potential and limitations are not yet as well-understood as for the other reactors. Given that the reactor has to be precisely sized to accommodate the kinetics of the desired process, it has more limited flexibility and is directed towards specific industrial application.

## 1.5 Objectives of this work

### 1.5.1 Layer-by-layer growth of metal oxides in solution

The first objective of my PhD is to deposit a metal oxide film, grown layer by layer in solution, on a catalyst surface.

The chemistry of metal oxide deposition both in solution and gas phase is rather well understood making it an ideal first target for developing liquid-phase ALD. The use of ALD in heterogeneous catalyst preparation is largely dominated by the deposition of oxides. This creates the opportunity to compare new liquid-phase metal oxide deposition methods with previously reported results that used gas phase methods.

Achieving layer-by-layer growth is necessary to gain sufficient control over the structure of the overcoat, and approach atomic accuracy as much as possible. In contrast with sol-gel deposition where

growth occurs by kinetically-controlled continuous processes, layer-by-layer growth offers the possibility to stop (or pause) the growth as desired. Furthermore, by carrying out the synthesis in solution, agglomeration of the substrate can be prevented.

The most common use of metal oxide ALD in catalysis is arguably the deposition of a protective layer that prevents deactivation phenomena. As catalysts almost always undergo structural changes during reaction, there is a critical need to facilitate the deposition of a shield layer. I will target this application first.

### 1.5.2 Matching liquid-phase atomic layer deposition's quality and versatility

After fulfilling the first objective, efforts will be made to improve the overcoat quality and versatility.

First, to match ALD, I wanted to develop a system where reactions were truly self-limited. Otherwise, a rough porous film will likely be deposited (if deposition occurs at all, as the absence of self limiting reactions could lead to solution phase reactions). The quality of the coating should match that of materials prepared with state-of-the-art gas-phase ALD equipment.

Second, the robustness of the method must be demonstrated. Two parameters can be a source of issues: changes in the substrate and changes in the chemical nature of the layer. The substrate's surface functionality, nanostructure and total area are features that may complicate the deposition. Examples of liquid-phase ALD on extreme cases must be performed to demonstrate robustness. With regards to the composition of the deposited layer, the vastness of possibilities of gas-phase ALD are partly due to the fact that it is not limited to metal oxide deposition. Therefore, to demonstrate that liquid-phase ALD is equally versatile, methods to develop non-metal oxide deposition should be developed.

### 1.5.3 Overcoming gas phase limitations

The next step in liquid-phase ALD development is to go beyond what is possible with gas-phase methods. Concretely, the objective is to prepare supported, isolated metal oxide clusters with controlled composition and structure by tracking the amount of precursor being deposited.

Such materials are technically challenging to prepare because small, supported entities are rather unstable and tend to agglomerate as they are formed. In general, heterogeneous nucleation phenomena are complicated to control. The mild deposition temperature associated with the inherently self-limited ALD reactions might make liquid-phase ALD an efficient strategy to prepare such clusters. In addition, because our liquid phase methods involve tracking the amount of precursor being deposited, these methods can inherently be used to monitor cluster growth.

In terms of catalysis, enabling atomic control of the composition of surface structures creates a unique opportunity to investigate interactions between individual atoms in a cluster, especially their cooperativity during catalysis.

# Chapter 2 Layer-by-layer growth of a metal oxide in solution

This chapter presents a first attempt to mimic ALD in liquid phase. While the method presented here does not meet the requirements to be considered ALD, it represents the groundwork that will be useful for the next chapter. This method also demonstrates that porous layers can be sufficient to stabilize metal nanoparticles on catalyst surfaces, despite being of lower conformality than those prepared by gas phase ALD.

Working in liquid phase allowed us to improve the dispersion of the support and use low volatility precursors. The chemistry of sol-gel precursors is often used to prepare metal oxides in solution, thus we used an aluminum alkoxide as an aluminum source. To better approximate ALD conditions, we chose to work without a complexing agent that would slow down the reaction and we implemented a system of liquid injections to mimic ALD pulses.

In terms of catalysis, we decided to assess the influence of the overcoat on catalyst stability in a case where deactivation was expected: supported transition metals (susceptible to sintering) transforming bio-sourced compounds (frequent fouling, overreaction, and promotion of metal nanoparticle leaching) while dispersed in a relatively polar liquid (which promotes physico-chemical deactivation).

## Catalyst stabilization by stoichiometrically limited layer-by-layer overcoating in liquid media.

*Florent Héroguel<sup>‡</sup>, Benjamin P. Le Monnier<sup>‡</sup>, Kristopher S. Brown, Juno C. Siu, Jeremy S. Luterbacher*

<sup>‡</sup>These authors contributed equally.

### Contributions:

Dr. Heroguel and I both contributed to the design of the method. I prepared all the materials presented in the article and co-supervised our interns (Kristopher and Juno) who assisted in the optimization of the synthesis. I also ran half of the catalytic tests, all of the physi- and chemisorption experiments, and all of the TEM analysis except the one presented in **Figure A-3**

**Abstract:** The use of metal oxide overcoats over supported nanoparticle catalysts has recently led to impressive improvements in catalyst stability and selectivity. The deposition of alumina is especially important for renewable catalysis conditions due to its robustness in liquid-phase conditions. However, there are limited reports of work on alumina deposition and stabilization that goes beyond



atomic layer deposition (ALD). Here, we present a layer-by-layer deposition technique for the controlled formation of conformal alumina overcoats in the liquid phase. This technique is easy to perform in common wet chemistry conditions. Alternated exposure of the substrate to stoichiometric amounts of aluminum alkoxide and water in liquid-phase conditions leads to the formation of a porous overcoat that was easily tunable by varying synthesis parameters. The deposition of 60  $\text{Al}_2\text{O}_3$  layers onto  $\text{Al}_2\text{O}_3$ -supported copper nanoparticles suppressed irreversible deactivation during the liquid-phase hydrogenation of furfural – a key biomass-derived platform molecule. The porous overcoat leads to highly accessible metal sites, which significantly reduces the partial site blocking observed in equivalent overcoats formed by ALD. We suggest that the ease of scalability and the high degree of control over the overcoat’s properties during liquid-phase synthesis could facilitate the development of new catalyst overcoating applications.

## 2.1 Introduction

Stability has a huge influence on the industrial viability of catalytic materials. Catalyst deactivation incurs significant costs due to the need for material regeneration and eventual replacement, and therefore has been a major focus in petrochemical research <sup>[200]</sup>. Reversible deactivation is often due to coverage of the active site by chemical binding (e.g. poisoning) or coverage of the active site (e.g. coking) <sup>[200,201]</sup>. These forms of chemical deactivation can often be reversed by thermal treatment such as calcination with air. Irreversible deactivation is much more costly and is often due to physical or thermal processes <sup>[13,201]</sup>. Prominent irreversible deactivation mechanisms include support collapse, and coalescence or leaching of metal nanoparticles. Coalescence refers to the loss of active surface by metal nanoparticle aggregation through Ostwald ripening or sintering. Leaching refers to metal dissolution and occurs principally in solution.

Because most fossil-derived molecules are volatile, refineries largely rely on gas phase catalysis. The shift to renewable substrates often involves liquid-phase catalytic processing. Such conditions are required because biomass-derived molecules usually have low volatility and are produced by biomass depolymerization or biological transformation in dilute aqueous or solvent streams <sup>[202–204]</sup>. Irreversible deactivation, including by sintering and leaching, tends to be more pronounced in liquid-phase conditions, which makes catalyst stability even more critical <sup>[200,201,205]</sup>.

Catalyst overcoating by deposition of a metal oxide layer is a promising method to curtail irreversible deactivation. Several overcoating methods have been shown to protect metal nanoparticles against thermal deactivation, and in some cases, coking. These methods include the use of atomic layer deposition (ALD) of alumina <sup>[145,151,206]</sup> and silica deposition by sol-gel <sup>[144,207,208]</sup>. Atomic layer deposition of alumina involves the subsequent exposure of the substrate to reactive alumina precursors or water in near-vacuum conditions. Each cycle leads to the deposition of an atomically thick layer of alumina, which allows very accurate control of the overcoat’s thickness. However, the near-vacuum conditions lead to high set-up costs and limit scale-up possibilities. Furthermore, ALD conditions lead to the formation of a dense overcoat, which completely blocks access to the metal. Catalytic activity is only recovered after a calcination step that crystallizes and cracks the overcoat <sup>[206]</sup>. However, even after calcination, access to the metal is typically significantly reduced. In comparison, overcoating with  $\text{SiO}_2$  by sol-gel chemistry is low-cost and easy to scale up. Although the degree of



control does not match ALD's, the overcoat's thickness can be kinetically controlled within a few nm due to the low reactivity of siloxide precursors<sup>[209,210]</sup>. The utility of silica overcoating is nevertheless limited by silica's low stability in high temperature liquid-phase conditions, which lead to rapid structural collapse<sup>[211]</sup>.

Alumina is much more resistant in liquid-phase conditions, but the reactivity of its alkoxy precursors make its deposition difficult to control kinetically. Because of this, there are few practical liquid-phase synthesis methods for producing alumina overcoats. Instead, attempts to deposit alumina using sol-gel techniques have focused on mimicking the layer-by-layer approach and purge sequences of ALD. Such methods have been reported for several oxides including titania<sup>[212–214]</sup>, alumina<sup>[215,216]</sup> and zirconia<sup>[216]</sup> and involve the subsequent exposure of the catalyst to metal precursor and aqueous solutions. Multiple washes are performed between exposures to avoid precipitation of material off the surface. The powder is then dried and calcined to obtain a single molecular layer of oxide. These steps are repeated multiple times to achieve a conformal overcoat. This method is precise but extremely time-consuming, and its multiple steps make it as difficult to scale-up as ALD. Furthermore, calcination between each deposition step prevents tuning of the overcoat.

Here, we present a simple method for the liquid-phase deposition of conformal alumina overcoats. Our technique is based on the alternated exposure of the substrate's hydroxyl groups to metal oxide precursors and water. Instead of purging excess precursor, we subsequently inject stoichiometric amounts of reactants to avoid side-reactions with unreacted excess precursor. This method enables fast and straightforward cycling and overcoat deposition. We demonstrate that, like ALD, our overcoat stabilizes a supported Cu/Al<sub>2</sub>O<sub>3</sub> catalyst during the liquid-phase hydrogenation of biomass-derived furfural. This stabilization occurs despite the fact that the overcoat is significantly more porous than that obtained with ALD, thus retaining high copper accessibility.

## 2.2 Experimental

### *Chemicals and materials*

All commercial chemicals were analytical reagents, and were used without further purification unless otherwise noted. Copper nitrate trihydrate (99.999-Cu %) was purchased from ABCR. The concentrated hydrochloric acid aqueous solution (*ca.* 37%) was purchased from Merck. The concentrated nitric acid aqueous solution (*ca.* 68%) was obtained from Sigma-Aldrich. Synthetic air (99.999%), hydrogen (99.999%), helium (99.9999%), N<sub>2</sub>O (99.99%)/helium (99.999%) 1/99 vol./vol. and nitrogen (99.999%) were obtained from Carbagas. Silicon carbide (100 mesh) was purchased from Strem. Furfural (99%) was purchased from Acros organic, purified by distillation under reduced pressure and stored under inert atmosphere. Aluminum sec-butoxide (97%) was purchased from Merck, purified by distillation under reduced pressure and stored over 4 Å molecular sieves (Merck) under inert atmosphere. Alumina (37 m<sup>2</sup>/g, Nano Arc) was purchased from Alpha Aesar and calcined for 12 hours at 500°C (5°C/min) under a flow of air (100 mL/min). 1-butanol (99.5%) was purchased from Acros. 2-butanol (99%) was purchased from Sigma-Aldrich, dried over magnesium, distilled, stored over 4 Å molecular sieves (Merck) and degassed under vacuum. Water was purified using a Millipore Milli-Q Advantage A10 water purification system to a resistivity higher than 18 MΩ.cm.

## *Catalyst preparation*

### *Preparation of alumina-supported copper NPs by incipient wetness impregnation*

The alumina support was pretreated under vacuum ( $< 10^{-3}$  mbar) at 150°C (heated to temperature with a 5°C/min ramp) for 12 hours and stored in a nitrogen filled glovebox prior to impregnation. A suitable amount of copper nitrate trihydrate was dissolved in a 0.1M nitric acid aqueous solution and added dropwise to the support until incipient wetness was reached. The resulting powder was dried for 12 hours at 95°C in air, reduced for 5 hours under H<sub>2</sub> flow (300°C, heated to temperature with a 1°C/min ramp) and finally passivated at room temperature with air pulses carried by a flow of N<sub>2</sub>.

### *Deposition of porous alumina overcoat*

The catalysts were pretreated under vacuum ( $< 10^{-3}$  mbar) at 300°C for 5h and kept under inert atmosphere using Schlenk techniques and a nitrogen-filled glovebox (typically  $< 0.5$ ppm H<sub>2</sub>O and  $< 0.5$ ppm O<sub>2</sub>). The powder was dispersed by magnetic stirring in anhydrous 2-butanol and the mixture was heated to 60°C. A solution was prepared for each precursor in a Schlenk flask by dissolving the appropriate amounts of water and aluminum sec-butoxide, respectively, in 2-butanol. 0.5 mL of the precursor solution (corresponding to coverage by a single monolayer) were alternatively injected every 15 min using syringes. The coverage of a single monolayer was estimated by a volume projection of the precursor molecule. This projected area was estimated using the MarvinSketch ChemAxon software. The quantity of material needed for a single layer per catalyst surface was calculated from this calculated area for a single complex.

Typically, cycles were repeated 15, 30, 45 or 60 times to obtain different overcoat thicknesses. The overcoated catalyst was separated by centrifugation (4000 rpm, 5 min), washed twice with 2-butanol (40 mL) and twice with water (40 mL). Finally, the collected powder was dried in an oven for 12 hours at 150°C (heated to temperature with a 2°C/min ramp).

## *Catalytic testing*

Furfural hydrogenation was investigated using a packed bed down flow tubular reactor (i.d = 4.5 mm). Typically, 0.2 g of catalyst were diluted into a bed of silicon carbide within the heated zone of the reactor, which was delimited by conductive aluminum blocks placed within the oven. The reactor was leak-tested under 30 bar of nitrogen pressure.

Before the first run, the catalyst was pretreated under air flow (100 mL/min) for 1 hour at 300°C (heated to temperature with a 2°C/min ramp), cooled down to 30°C under nitrogen flow (100 mL/min) and reduced under H<sub>2</sub> flow (100 mL/min) for 5 hours at 300°C (heated to temperature with a 1°C/min ramp). After cooling down to the reaction temperature (130°C), hydrogen flow was set to 35 mL/min using a Brooks mass flow controller and pressure was adjusted to 23 bars using a Tescom back pressure regulator. A furfural solution (70 g/kg in 1-butanol) was then pumped through the reactor using SSI Series II HPLC pump at 0.10 mL/min. Liquid samples were collected using a gas-liquid separator. Gas phase analyses were performed on an Agilent Technologies 7890 A gas chromatography apparatus equipped with a flame ionization detector (FID) and a HP-5 column (50 m, 0.32 mm).

After reaction, furfural flow was stopped and the catalyst was regenerated by calcination under a flow of air (400°C, 1 h, heated to temperature with a 2°C/min ramp, 100 mL/min) and reduction under hydrogen flow (300°C, 5 h, heated to temperature with a 1°C/min ramp, 100 mL/min).

#### *Catalyst characterization*

##### *Inductively coupled plasma optical emission spectrometry (ICP OES).*

Elemental analyses were performed at the EPFL Central Environmental Laboratory using inductively coupled plasma optical emission spectrometry (ICP OES) ICPE-9000 multitype, Shimadzu. Metals were carefully dissolved using a mixture of concentrated nitric and hydrochloric acids (1:2 vol:vol).

##### *Transmission electron microscopy (TEM)*

The overcoat's morphology was characterized by Transmission Electron Microscopy and High-Angle Annular Dark-Field Scanning Transmission Electron Microscopy (HAADF-STEM) on a FEI Talos with a 200 kV acceleration voltage. Lacey carbon grids were prepared by directly 'dipping' the grid into the alumina powder. The particle size distribution was estimated by statistical analysis of *ca.* 200 particles. Metal dispersion, defined as the ratio between surface and total metal atoms, was calculated back from particle size distribution assuming a spherical geometry. Elements were mapped using energy dispersive X-ray spectroscopy (EDX).

##### *Physisorption and chemisorption*

Brunauer-Emmett-Teller (BET) surfaces and Barrett-Joyner-Halenda (BJH) pore volumes were measured by N<sub>2</sub>-physisorption on a Micromeritics 3Flex apparatus at liquid nitrogen temperature. Samples were dried at 120°C under vacuum ( $< 10^{-3}$  mbar) for 4 h prior to analysis.

Quantification of surface copper was performed on a Micromeritics Autochem II 2920 using N<sub>2</sub>O as a reactive probe selective to surface atoms according to the method described by Vannice *et al.* <sup>[217]</sup>. Typically, 0.2 g of sample were reduced in situ (300°C, 1 hour, heated to temperature with a 10°C/min ramp) and contacted with 0.5 mL N<sub>2</sub>O pulses using a sampling loop carried by a flow of helium at 90°C while N<sub>2</sub> evolution and N<sub>2</sub>O consumption were quantified by monitoring masses 28 and 44 using MKS Cirrus 2 mass spectrometer.

## 2.3 Results and discussion

Alumina spheres (50 nm,  $S_{\text{BET}} = 34 \text{ m}^2/\text{g}$ ) were used as a support to facilitate overcoat conformity analysis by microscopy. Aluminum tri-sec-butoxide (Al(OsBu)<sub>3</sub>) was selected as an aluminum source for overcoating due to its high solubility in alcohols and reactivity with water. Prior to overcoating, copper nanoparticles were formed by calcination and reduction of alumina impregnated with a solution of copper nitrate. High-Angle Annular Dark-Field Scanning Transmission Electron Microscopy (HAADF-STEM) pictures showed that the resulting nanoparticle size was  $3.4 \pm 0.7 \text{ nm}$  or a 32% metal dispersion assuming spherical geometry <sup>[218]</sup> (**Figure 2.1A**, histogram **Figure A-1**).

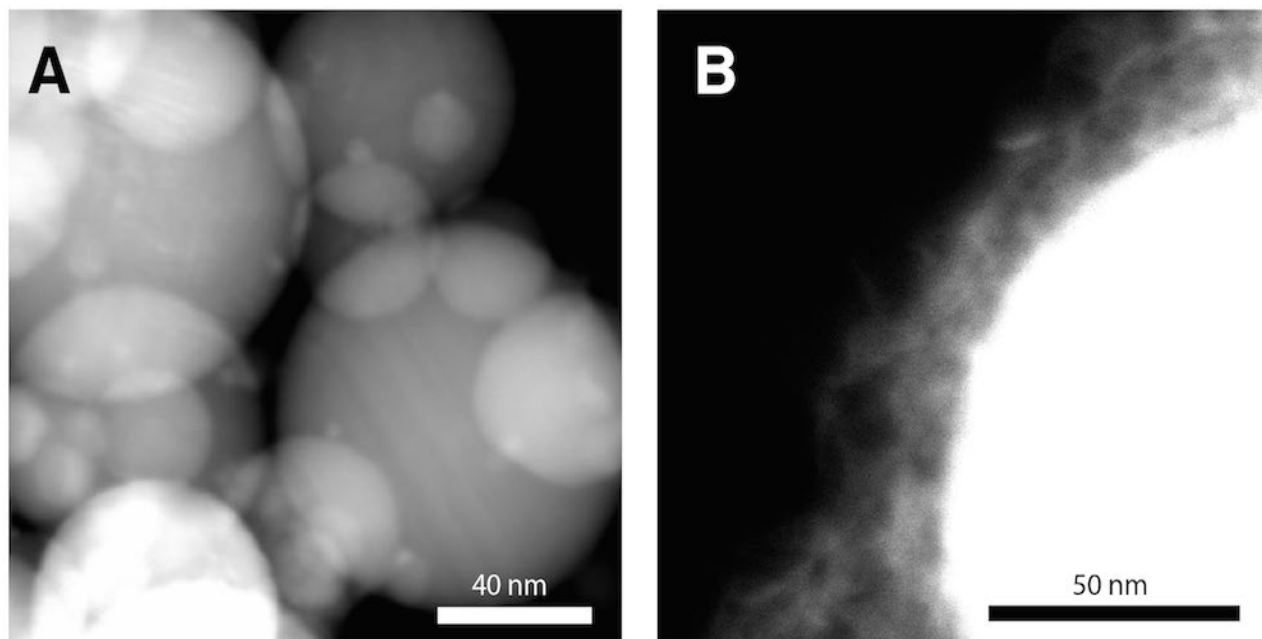


**Figure 2.1:** STEM HAADF images of (A) Copper nanoparticles supported on alumina spheres ( $\text{Cu}/\text{Al}_2\text{O}_3$ ); (B)  $\text{Cu}/\text{Al}_2\text{O}_3$  after deposition of an amorphous alumina overcoat (60 cycles, using a water-to-aluminum molar ratio of 2.0).

Our technique is based on an accurate determination of precursor stoichiometries. Any excess precursor left in solution after reaction led to homogeneous nucleation during the subsequent half-cycle. This occurrence then created a seed for undesired heterogeneous nucleation throughout the process, which resulted in the creation of additional support, diluting the active site without any stabilization. In contrast, the addition of insufficient amounts of precursor left the surface partially uncovered, with some unprotected metal particles. Therefore, precise determination of the initial amount of precursor was essential to ensure conformal surface coverage. The support was treated at a relatively low dehydroxylation temperature ( $300^\circ\text{C}$ ) in order to create a high surface hydroxyl density ( $> 6 \text{ OH}/\text{nm}^2$ )<sup>[219]</sup>. In these conditions, the large size of aluminum tri-sec-precursors prevented full occupancy of surface hydroxyl groups. Therefore, monolayer coverage could be calculated assuming a surface fully packed with precursor molecules according to a projection of their van der Waals volume (Fig. 2A) (calculated as  $0.65 \text{ nm}^2$ ). The  $\text{Al}_2\text{O}_3$  sphere surface area was measured by physisorption ( $S_{\text{BET}} = 34 \text{ m}^2/\text{g}$ ) and was divided by the precursor's projected surface area to calculate a monolayer coverage stoichiometry of  $87 \text{ }\mu\text{mol}$  of precursor per gram of  $\text{Al}_2\text{O}_3$  spheres.

The supported catalyst was carefully suspended in anhydrous sec-butanol using sonication to avoid any diffusion transfer issues with large agglomerates. Then, coating was done by alternatively injecting  $0.5 \text{ mL}$  of a sec-butanol solutions containing the calculated amounts of either aluminum tri-sec-butoxide or water every 15 minutes through an air-tight septum (Figure 2.2 B and C). A blank test was performed in the absence of the support to ensure that a full reaction between precursors occurred within the alternate injection time frame. We also performed a coating with a reaction time between injections of 60 min, but this did not affected the properties of the overcoat, demonstrating that the reaction was largely over within 15 min. After completion of the targeted number of cycles, the material was washed with sec-butanol to eliminate any unreacted precursor and with water to ensure complete hydrolysis of alkoxide ligands. The resulting substrate was then dried for storage.

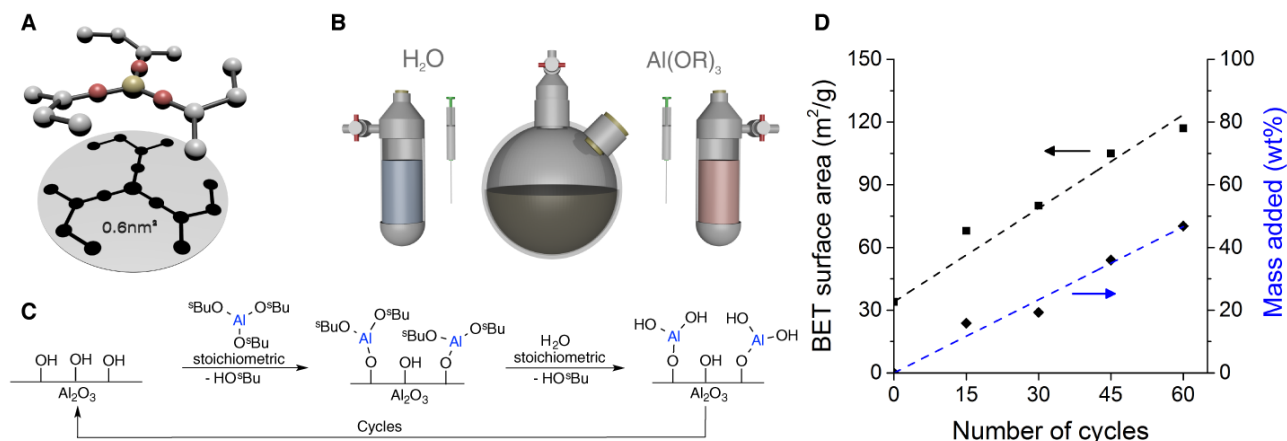


**Figure 2.2:** (A) Schematic representation of the aluminum precursor ( $\text{Al}(\text{OsBu})_3$ ) and its projected surface area. (B) Experimental setup for the stoichiometrically limited layer-by-layer overcoating. (C) Two-reaction sequence of a single overcoating cycle. (D) Evolution of BET surface area and additional catalyst mass as a function of the number of overcoating cycles (using a water to aluminum molar ratio of 2).

STEM-HAADF revealed the presence of a low-density overcoat surrounding the dense spherical substrate after 60 cycles (**Figure 2.1 B**). Conformality did not match that achieved with ALD, but the surface was largely overcoated, as confirmed by subsequent nanoparticle characterization. The high porosity observed by TEM was confirmed by nitrogen physisorption measurements, which showed a linear increase of BET surface area from  $34 \text{ m}^2/\text{g}$  for  $\text{Al}_2\text{O}_3$  spheres to 68, 80, 105 and  $117 \text{ m}^2/\text{g}$  after deposition of 15, 30, 45 and 60 cycles, respectively (**Figure 2.2 D**,  $\text{N}_2$  adsorption and desorption isotherms are presented in **Figure A-2**). Accessibility of the copper nanoparticles was assessed by titration of  $\text{Cu}^0$  sites using  $\text{N}_2\text{O}$  after reduction at  $300^\circ\text{C}$ . Surface copper before overcoating was  $38 \mu\text{mol/g}$  and dropped to  $21 \mu\text{mol/g}$  after deposition of 30 cycles confirming partial coverage of the metal. Nevertheless, about half of the surface copper was still accessible after coating, confirming the relatively high porosity of the overcoat and suggesting that the access to the metal and associated catalytic activity could be preserved. Interestingly, the number of deposition cycles has no significant influence on the Cu surface accessibility ( $19$  and  $23 \mu\text{mol/g}$  of surface Cu sites were measured for 15 and 50 cycles, respectively). In contrast, the dense overcoat deposited by ALD covered the metal surface completely and required calcination and cracking to restore access to the catalytic sites <sup>[206]</sup>. No further cracking or etching of the overcoat was required using the present method.

The influence of the assumed coverage stoichiometry was studied by varying the quantity of alkoxide precursor injected at each cycle. Quantities corresponding to 0.5, 1 and 2 monolayers per injection as calculated by volume projection were used in coatings with 30 cycles (**Figure 2.3 A**). The average thickness and shape irregularity of the overcoat were measured and calculated to allow for a quantitative comparison of the materials. The irregularity parameter was calculated as the standard deviation based on 10 measures of the overcoat thickness for each particle (see Section S3 for a detailed description of the calculation). A smaller irregularity value corresponds to a more conformal coating. When quantities of alkoxy precursor corresponding to 0.5 monolayers per cycle were injected, the resulting overcoat had a similar thickness to that observed when quantities corresponding to 1 monolayer were injected (**Figure 2.3 A**, **Table A-1**). However, the irregularity in shape was significantly higher with 0.5 monolayer equivalents per cycle. This increase in irregularity is consistent with the

formation of a partially coated substrate, and with subsequent cycles preferably growing on the recently formed low-density overcoat (**Figure 2.3 A I**). As expected, the use of an amount of alkoxy precursor corresponding to 2 monolayers per cycle led to an average overcoat thickness that was twice as large as when 1 monolayer was used (**Figure 2.3 A**). However, the irregularity was twice as high as when a single monolayer was targeted at each cycle (**Figure 2.3 A III**). This could be explained by the deposition of large alumina clusters on the surface after they were formed in solution by homogeneous nucleation. Overall, the ideal precursor to surface stoichiometry appeared to be the amount of precursor estimated to form a single monolayer (**Figure 2.3 A II**). This result supported the assumption that this amount can be calculated using a simple volume projection of the alkoxy precursor on the surface of the support.

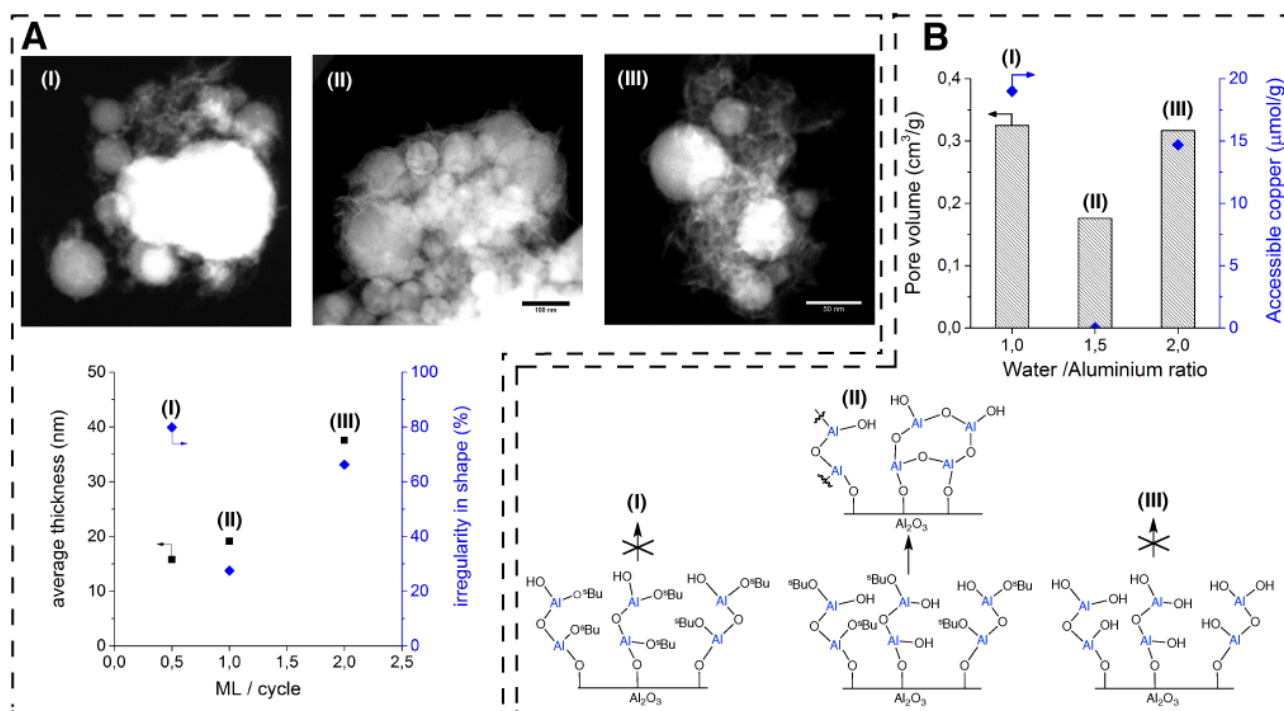


**Figure 2.3:** Influence of the stoichiometry on the structural properties of the catalysts after deposition of 30 cycles. (A) Impact of the aluminum precursor quantity added per cycle (reported in number of equivalent monolayers or ML per cycle) on the thickness and conformality of the overcoat (using a water-to-aluminum molar ratio of 2.0). (B) Influence of water-to-aluminum ratio on the overcoat's density and on copper's accessibility.

The reaction of an alkoxy precursor with hydroxyl groups on the surface of the support led to the formation of a population of mono, bis and tris-grafted species by substitution of 1, 2 or 3 monodentate sec-butoxy ligands with surface hydroxyl groups and the associated release of sec-butanol in solution (**Figure 2.2 C**). The remaining ligands had to be hydrolyzed by the addition of water, which repopulated the surface with hydroxyl groups. Therefore, the amount of water required to hydrolyze any remaining ligands depends on the connectivity of the grafted alkoxy group. A lower amount of required water will be associated with a higher connectivity and, thus, a denser overcoat. We tested several water-to-aluminum ratios (1.0, 1.5 and 2.0 H<sub>2</sub>O:Al(OsBu)<sub>3</sub> mol:mol). Using water-to-alkoxy ratios of 1.0 and 2.0 led to larger pore volumes (both 0.32 cm<sup>3</sup>/g, calculated according to Barrett, Joyner and Halenda - BJH - model) and high accessibility of copper after coating (19 and 15 μmol/g, respectively) (**Figure 2.3 B**). In contrast, a denser layer (0.18 cm<sup>3</sup>/g) preventing access to copper (0

$\mu\text{mol/g}$ ) was formed using a water-to-aluminum ratio of 1.5 (**Figure 2.3 II**). This result suggests that aluminum atoms could react with up to an average of 1.5 surface grafted hydroxyl groups, and could thus require 1.5 water molecules to be hydrolyzed. Lower water ratios could leave non-hydrolyzed sec-butoxide ligands behind, which would act as spacers, favoring porosity (**Figure 2.3 I**). Higher water ratios favored over-hydrolyzing the alkoxy precursor, preventing it from cross-condensing with other grafted hydroxyl groups, which could also favor increased porosity (**Figure 2.3 III**). This proposed effect is illustrated in **Figure 2.3**, and demonstrates the control that sol-gel synthesis parameters can exert over the overcoat – notably, to tune the accessibility to the metallic active sites.

The catalytic performances of the uncoated and coated catalysts (60 cycles, using a water-to-aluminum molar ratio of 2.0) were tested in the liquid-phase hydrogenation of furfural in 1-butanol (23 bar  $\text{H}_2$ , 130°C). Furfural is a key biomass-derived platform molecule and its transformation to furfuryl alcohol is highly relevant for biomass valorization to certain fuels and bulk chemical intermediates [6, 25–27]. Recent studies have shown that furfural production is favored in organic solvents as opposed to aqueous conditions, and is often produced at relatively dilute concentrations (i.e. <10 wt%) making its separation energy intensive [204,220,223,224]. Therefore, its direct conversion in the liquid phase would be both economically and energetically advantageous. However, such liquid-phase conditions can often lead to rapid irreversible deactivation of the catalyst by sintering and/or leaching.

Indeed, the uncoated catalyst rapidly deactivated with time-on-stream, showing a 9-fold activity decrease over 48 hours (**Figure 2.4 A**). Some of this activity could be recovered by regeneration of the catalyst by calcination at 400°C. This demonstrates that the deactivation was partially due to the deposition of carbonaceous residues on the surface of the catalyst. However, each regeneration cycle led to an irreversible loss of activity, until only about 16% of the initial activity was recovered after the 5<sup>th</sup> regeneration. This decrease indicated that significant irreversible deactivation had occurred over the course of several reaction/regeneration cycles. The low conversion (*ca.* 7%, ~100% selectivity to furfuryl alcohol) measured at the end of run 6 equals conversion measured in the absence of copper and hydrogen, and hence could be entirely attributed to transfer hydrogenation by  $\text{Al}_2\text{O}_3$  support (see further discussion in Section S4). Leaching of the copper in solution was not significant, as determined by inductively coupled plasma optical emission spectrometry (ICP OES) analysis of the collected samples after concentration, which showed the presence of < 0.10% of the total original copper (see **Table A-2** for detailed leaching calculations). Mapping using energy dispersive X-ray spectroscopy (EDX) revealed the presence of large copper clusters (> 200 nm) after reaction (**Figure A-3**). The mean particle size was increased to  $47 \pm 46$  nm (**Figure A-4**), corresponding to 4% metal dispersion assuming spherical geometry compared to the original 32%. This 8-fold decrease in dispersion corresponded very closely to the 6.5-fold decrease in activity observed after 5 regeneration cycles. Therefore, the loss of activity was largely attributed to sintering, confirming previous findings [225].

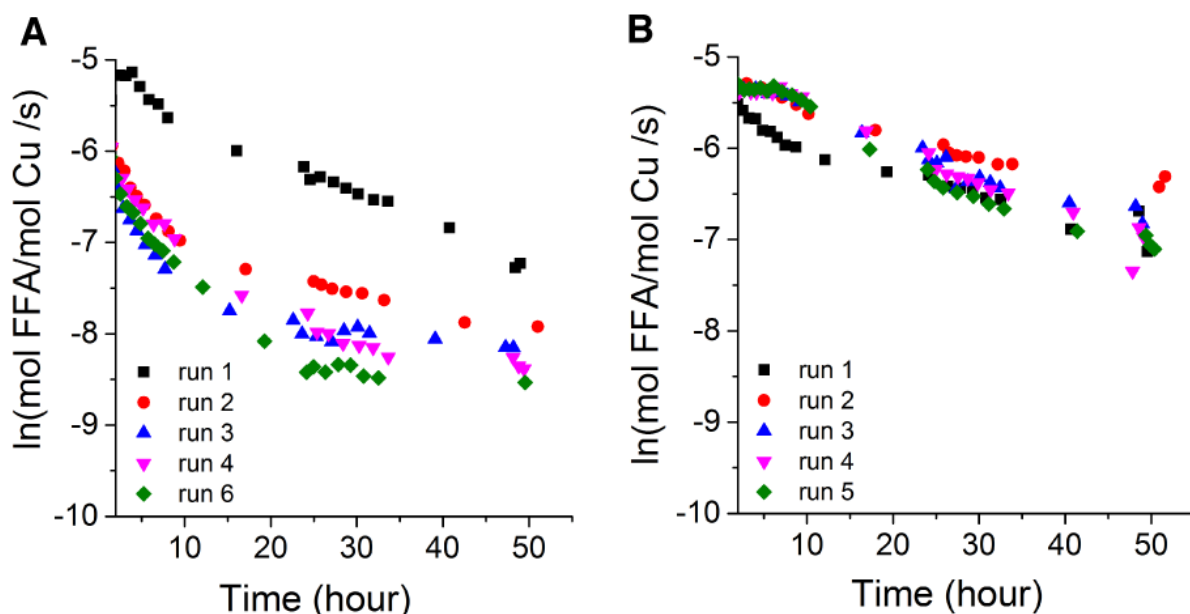


**Figure 2.4:** Catalytic activity per total moles of Cu of (A) Cu / Al<sub>2</sub>O<sub>3</sub> and (B) Cu / Al<sub>2</sub>O<sub>3</sub> after deposition of an amorphous alumina overcoat (60 cycles, using a water-to-aluminum molar ratio of 2.0) during the catalytic conversion of furfural into furfuryl alcohol in 1-butanol (130°C, 22 bar, 35 mL/min H<sub>2</sub>). Catalysts were calcined at 400°C under air flow and reduced at 300°C under H<sub>2</sub> flow between each run.

When using the catalyst overcoated with 60 cycles, the initial activity was within 20% of the activity of the uncoated material, confirming the excellent accessibility of copper surface sites through the porous overcoat (**Figure 2.4 B**). In contrast, ALD overcoating with 45 cycles led to significant blockage of copper surface sites even after calcination and cracking of the dense Al<sub>2</sub>O<sub>3</sub> overcoat<sup>[206]</sup>. This ALD overcoat led to a highly stable catalyst in liquid-phase conditions but also to an activity that was 10 times lower than that of the uncoated catalyst before deactivation. In fact, despite having a copper loading that was almost 3 times higher, the number of surface copper sites accessible on the ALD-overcoated was 20% higher compared to our overcoated material (21 vs. 16  $\mu\text{mol. Cu g}^{-1}$ )<sup>[206]</sup>.

Similar to the uncoated material, catalytic activity decreased with time-on-stream (**Figure 2.4**). However, unlike the uncoated material, initial activity was fully recovered (and sometimes exceeded) after regeneration by calcination, demonstrating that only reversible deactivation had occurred (**Figure 2.4 A**). This stable activity was maintained for 6 reaction runs and 5 regeneration cycles over the course of a 3-week period, showing that irreversible loss of metal surface area is suppressed by the presence of the stoichiometrically deposited overcoat. No leaching (< 0.15% total Cu, see **Table A-2**) was detected, while sintering of copper particles was negligible. The contrast between small copper and alumina in microscopy was poor for overcoated samples due to the small density differences between the support, metal particles, and overcoat. This prevented an accurate determination of the metal dispersion by microscopy before and after catalysis. However, the large particles (>10 nm) that were observed after reaction in the uncoated catalyst (**Figure A-4**) would have been visible by EDX mapping despite these imaging limitations for the overcoated catalyst. However, no such large particles were observed, further confirming that sintering had been successfully curtailed.



## 2.4 Conclusions

The effective stabilization of the catalyst indicates that the stoichiometrically limited liquid-phase deposition of alumina could be an effective alternative to ALD for catalyst overcoating applications. The use of stoichiometrically limited deposition allowed us to overcome the difficulties of depositing alumina in a controlled fashion in the absence of excessive precursor purging or washing. In addition, this method is particularly sensitive to synthesis parameters, which can be changed to control the overcoat's porosity and access to the metal site. This particular control over the overcoat's nanoarchitecture is absent in gas phase methods and could facilitate further tailoring of the active site's nanoscale environment. Efforts to use these properties to control the catalyst's activity and selectivity are currently underway.

### 2.4.1 Supplementary data

Supplementary data can be found in A. Supporting Information of chapter 2.

### 2.4.2 Acknowledgements

We thank the EPFL interdisciplinary center for electron microscopy for support during electron microscopy measurements. We acknowledge funding from the Swiss National Science Foundation through grant PYAPP2\_154281; and by EPFL. K. B. was supported by funding from the James B. Reynolds Scholarship for Foreign Study through Dartmouth University.



# Chapter 3 Developing a new method for liquid-phase ALD

This chapter is the preprint version of a communication accepted in *Advanced Materials* reproduced with the permission of the publisher.

In this communication, I outline a procedure for liquid-phase atomic layer deposition (ALD). The method presented in Chapter 2 gave good catalytic results. However, instead of exploring additional catalyst synthesis possibilities, I explored ways to improve the quality of the coating. Creating a liquid-phase deposition technique for overcoats with a level of conformality that matches that of materials made with ALD could open the field of catalysis to building active-sites with atomic accuracy.

Specifically, I tried to develop a method that would mimic the surface phenomena of ALD. As the alcohol released by the condensation and hydrolysis of an alkoxide could adsorb to the surface and direct measurement of aluminum in the solution would not be convenient, an alkyl precursor was used instead. The precursor volatility offered the possibility to track its release, and hence the reaction by gas chromatography. Previously, the water-to-aluminum ratio used in the sol-gel synthesis had been estimated, which led to decent coatings but this approach was likely insufficient to achieve atomic control. In this chapter, I discuss the importance of tracking these reaction in achieving precise conformal coatings.

# Atomic Layer Deposition on Dispersed Materials in Liquid Phase by Stoichiometrically Limited Injections

*Benjamin P. Le Monnier, Frederick Wells, Farzaneh Talebkeikhah, and Jeremy S. Luterbacher*

## Contributions:

- Frederick Wells: performed optimization of the tri octyl aluminum grafting, results were used in Figure B-19 and Figure B-20. His contribution was important regarding the demonstration of the method reproducibility.
- Farzaneh Talebkeikhah: ran the blank test, the result of which were used in **Figure B-17** (right graph).
- Solid-state NMR, XPS and XRD measurements were performed by the EPFL services (see acknowledgements).
- I designed the methods (with trioctyl aluminum, trimethyl aluminum, deposition of sulfide and phosphate), and ran all experiments other than the one previously mentioned, including synthesis (liquid-phase ALD and fluidized bed), characterizations (physi- and chemisorption, electronic microscopy), data processing and analysis of NMR, XPS, and XRD.

## 3.1 Abstract

Atomic layer deposition (ALD) is a well-established vapor-phase technique for depositing thin films with high conformality and atomically precise control over thickness. Its industrial development has been largely confined to wafers and low-surface area materials because deposition on high-surface area materials and powders remains extremely challenging. Challenges with such materials include long deposition times, extensive purging cycles and requirements for large excesses of precursors and expensive low-pressure equipment. Here, a simple solution phase deposition process based on subsequent injections of stoichiometric quantities of precursor is performed using common laboratory synthesis equipment. Precisely measured precursor stoichiometries avoid any unwanted reactions in solution and ensure layer-by-layer growth with the same precision as gas-phase ALD, without any excess precursor or purging required. Identical coating qualities are achieved when comparing this technique to fluidized-bed reactor ALD (FBR-ALD) with  $\text{Al}_2\text{O}_3$  deposition. The process was easily scaled up to coat >150g of material using the same inexpensive laboratory glassware without any loss in coating quality. This technique was extended to sulfides and phosphates and can achieve coatings that are not possible using classic gas-phase ALD, including the deposition of phosphates with inexpensive but non-volatile phosphoric acid.

## 3.2 Introduction

Atomic layer deposition is a layer-by-layer deposition technique that relies on two half reactions that occur between a vapor phase and a solid substrate. The first reaction involves precursor exposure

followed by purging with an inert gas to remove the excess of reactant. Second, the substrate is exposed to a counter-reactant also followed by a purge cycle. The key feature of this process is that both surface reactions with the precursor and counter-reactant are self-limited, which prevents deposition of more than an atomic monolayer per full cycle.<sup>[105]</sup> During this process, the reactor is typically maintained below atmospheric pressure within a temperature window that allows vaporization of the reactants without thermal decomposition.

Elemental zinc and elemental sulfur were the first precursor and counter-reactant, respectively, used for ZnS atomic layer deposition.<sup>[226]</sup> Since then, processes for depositing a range of materials including oxides, nitrides, hybrids and even metals have been developed.<sup>[124,128,227]</sup> This wide variety of materials combined with its atomic-level precision has made ALD a formidable tool for the fabrication of nanostructured materials such as transistors, solar cells and fuel cells<sup>[99]</sup>.

More recently, processes have been developed to apply ALD to high-surface area materials ( $>10$  m<sup>2</sup>/gram), including powders for various applications, from passivation of photoactive material to catalyst preparation.<sup>[228,229]</sup> With such materials, long exposure time (minutes vs. milliseconds for wafers), both for purge and reaction cycles, must be coupled with effective dispersion techniques to overcome mass transfer limitations. Setups typically include rotating reaction chambers or fluidized beds to disperse the particles, and will require extensive precursor recycling schemes at the industrial scale. The complexity of these installations has limited the application of this technique in research and, up to now, prevented its industrial implementation despite exciting published results.<sup>[189,191]</sup>

In this context, new strategies using deposition in liquid phase are emerging. Notably, we have used continuous injection of sol gel precursors to deposit reasonably conformal but systematically porous coatings<sup>[230,231]</sup>. Other work has focused on subsequent liquid-phase injections of ALD or sol gel precursors, but the coating quality was systematically much less conformal than that obtained with gas-phase ALD, likely because they involved oligomerization-precipitation mechanisms.<sup>[232–234]</sup> Other self-limited layer-by-layer liquid phase deposition processes such as successive ionic layer adsorption and reaction (SILAR) or microfluidic ALD on plates have been developed<sup>[235,236]</sup>, but, like gas-phase ALD, they use huge precursor (and solvent) excesses and cannot be used to coat dispersed substrates like powders. Liquids could greatly facilitate deposition on dispersed high-surface area substrates such as powders due to their higher density and viscosity compared to gas, which can effectively disperse these nanostructured materials without extensive mixing or fluidization.

Here, we designed an ALD procedure requiring only common inorganic chemistry laboratory equipment that avoids any excess of precursors and is simple to scale up, all while achieving similar coating qualities to gas-phase ALD. The basic principle (**Figure 3.1**) involves the dispersion of the powder substrate in a solvent and determination of the exact quantities of reactants to inject by titration of the precursor (and counter-reactant) prior to deposition, which is crucial to ensure high-quality coatings. Therefore, the deposition can be performed in a simple round-bottom flask at room temperature and pressure.

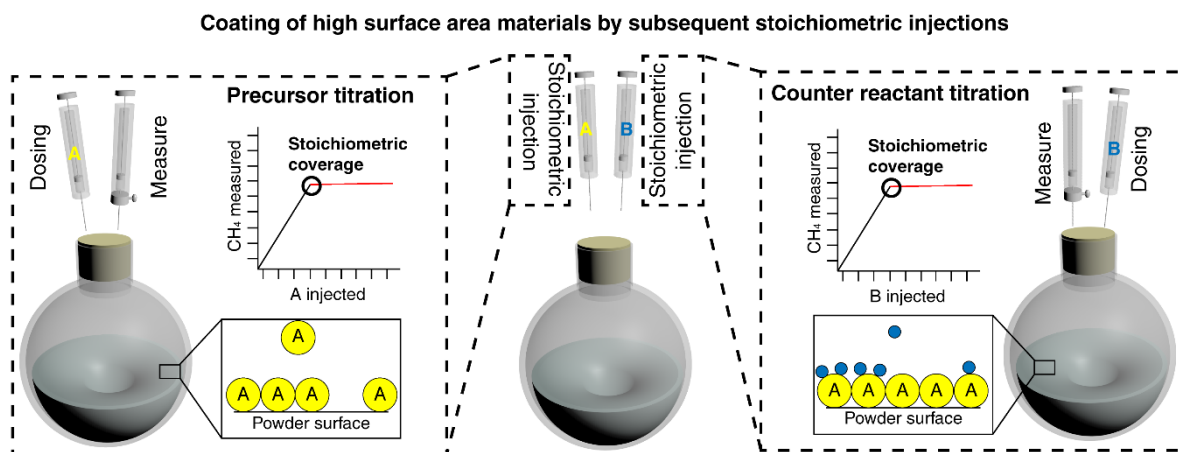


**Figure 3.1:** Process of the liquid phase ALD by stoichiometric injection based on precursor and counter-reactant titration of dispersed powder substrate.

We extensively studied alumina growth on silica using trimethyl aluminum (TMA) and water as the precursor and counter-reactant, as it was a well-studied system in gas-phase ALD<sup>[109]</sup> and we could also rely on work involving the grafting of alkyl aluminum in liquid phase on silica.<sup>[237,238]</sup> Nevertheless, we tested and showed that the approach is compatible with precursors releasing a non-volatile side like tri-octyl aluminum (see section S3).

### 3.3 Results and discussion

In our procedure, we first have to titrate the surface with the precursor, and then titrate a precursor-saturated surface with the counter-reactant. In both cases, the reactions between the precursor or counter-reactant are followed by the release of methane (**Figure 3.2**). The injected TMA reacted with surface hydroxyl groups on the dispersed catalyst and released methane (**Figure 3.2 A**). A remarkable benefit of this titration approach is that it allows for the in-situ monitoring of surface reactions and provides insight into the nature of these reactions. The slope of the methane released vs. TMA added reveals the number of methane atoms released per aluminum (**Figure 3.2 A and B**). Because the reaction is self-limiting, once the surface is saturated with TMA, a slope close to zero is observed as no more reaction occurs (**Figure 3.2 A**). Depending on the hydroxyl group density, each TMA molecule can react once or more with the surface, forming pending or bridging aluminum surface species (**Figure 3.2 B**).<sup>[239]</sup>

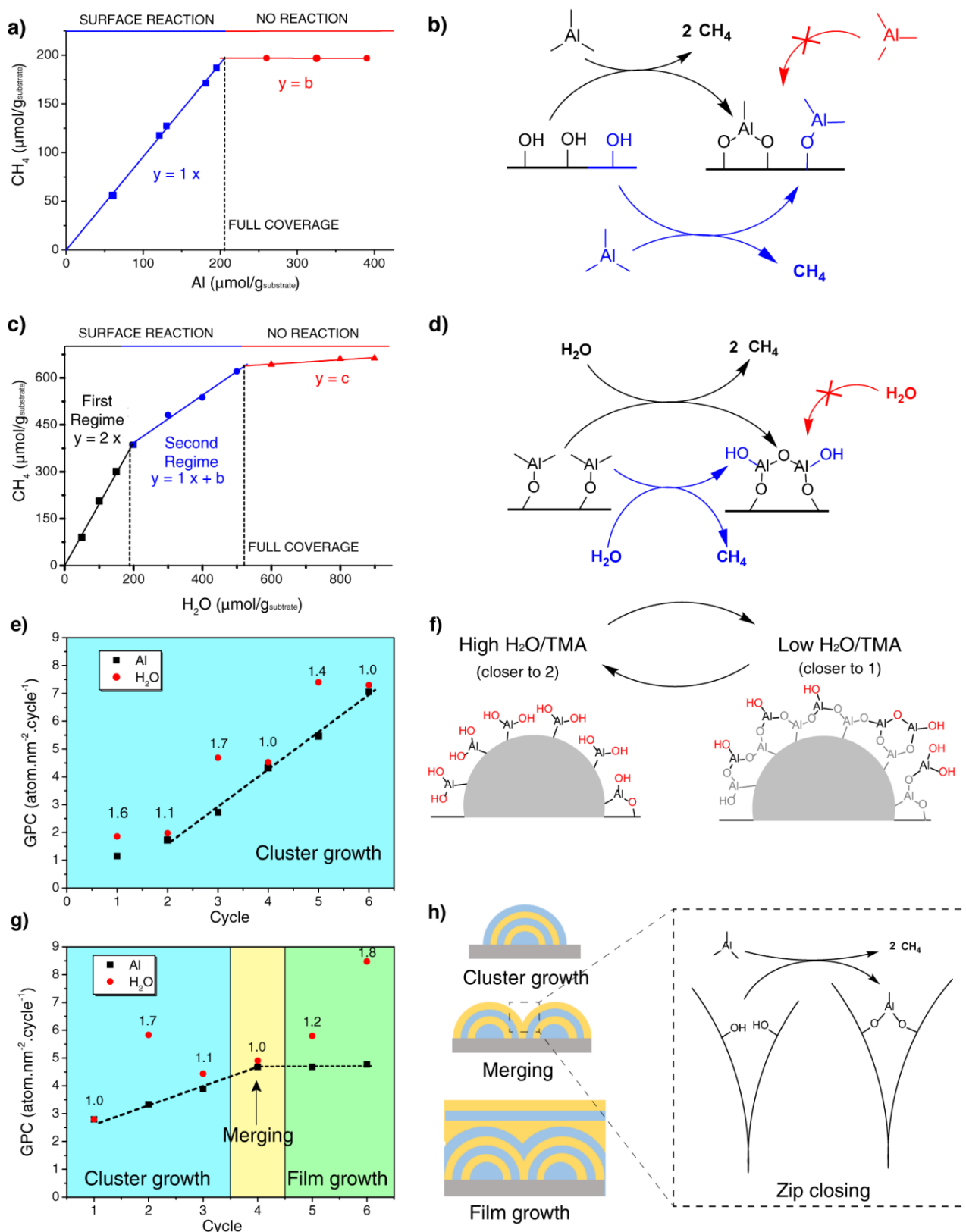


**Figure 3.2** Surface titration by released methane quantification and mechanisms of alumina growth. a) Surface titration of available hydroxyl groups during TMA addition normalized by initial mass of substrate. b) Reaction schemes for TMA and a hydroxylated surface leading to the release of one or two molecules of methane per TMA. c) Surface titration of hydrolysable methyl groups after deposition of a stoichiometric quantity of TMA. d) Reaction schemes for water and an alkyl aluminum-

covered surface leading to the release of one or two molecules of methane per molecule of water. e) and g) Growth per cycle (GPC), (i.e. quantity added at saturation) determined by TMA and water surface titration at each cycle on silica nanospheres, normalized by surface area with a starting hydroxyl density of e) 2 OH/nm<sup>2</sup> and g) 8 OH/nm<sup>2</sup>. The numerical labels above the water points refer to the water/aluminum ratio. f) Schematic representation of cluster growth showing, alternatively, a surface covered by pending aluminum, or bridging aluminum, leading to alternating high (up to 2) and low (as low as 1) water-to-aluminum ratios during each cycle. h) Sketches illustrating the various steps of ALD growth that were observed: the nucleation and growth of clusters, their merging, and continuous film growth.

Once the saturation point of TMA is established, a batch of catalyst could be covered with exactly one monolayer of aluminum in order to perform the water titration on the aluminum-covered surface. Similarly, water was added and the methane release was monitored (**Figure 3.2 C**). Different slopes were observed depending on the reactions involved, which include the formation of a pending hydroxyl group or of an oxo bridge (**Figure 3.2 D**).<sup>[240]</sup> Two separate regimes were observed in one titration (**Figure 3.2 C**). In such cases, when water was injected, it appeared to react more favorably with dense populations of adsorption sites by forming bridges, leading to the release of two methane molecules (slope of 2). Following the consumption of dense sites, water reacted with the remaining isolated sites, releasing 1 molecule of methane per molecule of water (slope of 1). A similar effect was previously suggested by McCormick et al., when using a rotary ALD reactor.<sup>[195]</sup> These results are highly analogous to plots showing growth rate versus pulse time in ALD studies, which demonstrates the self-limited deposition of both reactants on the surface.<sup>[107,111]</sup> The closed methane balance at each cycle confirmed the accuracy of each subsequent titration (**Figure B-1**).

The growth per cycle (GPC) for both aluminum and water was determined by dosing the amount of aluminum and water required to saturate each layer. When starting with a silica surface with a low density of hydroxyl groups (**Figure 3.2 E**), the quantity of aluminum grafted at each cycle kept increasing. This phenomenon is known in the ALD literature as being characteristic of a nucleation growth.<sup>[133]</sup> Isolated hydroxyl groups on the silica surface are the seeds for nucleation, from which each particle grows from cycle to cycle. We can measure, at each cycle, an average number of aluminum atoms per cluster on dispersed silica by simply using gas chromatography. Interestingly, the water-to-aluminum ratio alternates between  $1.1 \pm 0.1$  and  $1.6 \pm 0.2$ , which suggests that the alternate formation of mostly bridge (ratio of 1) or a mixture of bridge and pending (ratio of 2) functional groups. This sequence can be explained by a simple model (**Figure 3.2 F**). When a substrate is covered with a low density of individual hydroxyl groups, adsorbed aluminum will be mostly mono-grafted, and two water molecules are then required to hydrolyze the two pending methyl group on each aluminum (high water-to-aluminum ratio). As a consequence, the next layer is made of a denser layer of available hydroxyl groups, favoring the formation of a large majority of bridging aluminum, leading to a water-to-aluminum ratio of close to 1.

When starting with silica that contained a higher density of OH groups and a bit of physisorbed water (8 OH per nm<sup>2</sup>, **Figure 3.2 G**), the aluminum GPC initially increased but stabilized after the 4<sup>th</sup> cycle. As opposed to nucleation growth, a stable GPC is indicative of a relatively flat film growth, as each added layer contains the same quantity of aluminum. To inject the exact quantities of precursor to achieve one monolayer of coverage, we repeated our reactant and counteractant titration at each cycle until the film growth phase was achieved. During film growth, the ratio of water to aluminum that is



grafted still alternated between high and low as this does not depend on the shape of the previous layer (which was also observed for high surface silica, see **Figure B-2**). The regime between nucleation and continuous film growth is characteristic of merging nuclei, which features a notable increase in bridging oxygens as two nuclei merge (**Figure 3.2 H**).

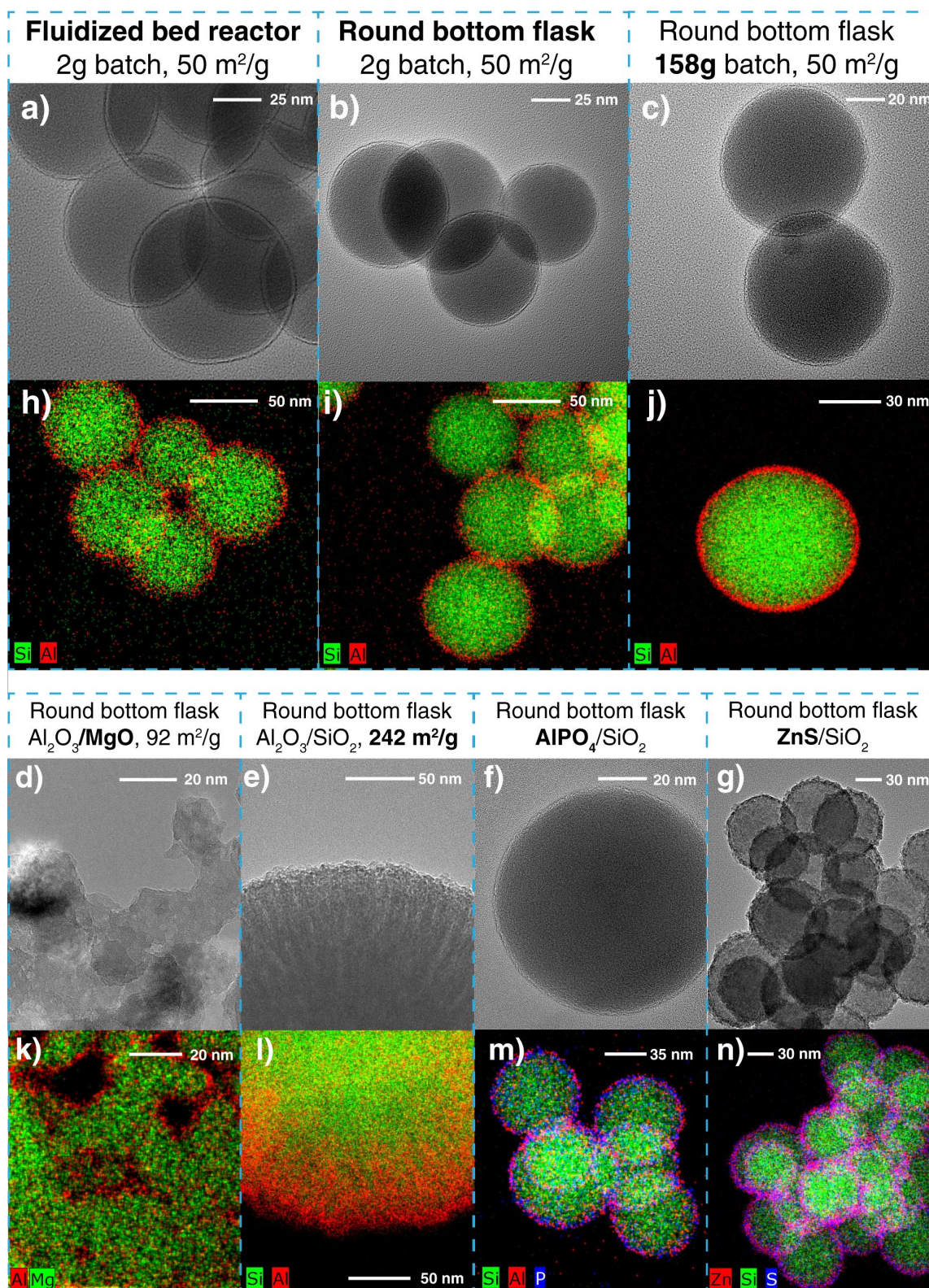


**Figure 3.3** a-c) Bright field transmission electron microscopy images of silica spheres coated with 10 cycles of TMA/water deposition using a) a commercial fluidized bed reactor ALD (2g batch) b) a round bottom flask (2g batch) c) the same procedure up-scaled to 158g. d) the same deposition method but on a basic substrate (MgO) with slightly higher surface area and e) using a high surface area silica as a substrate. f) AlPO<sub>4</sub> deposited onto silica particles using the same method but replacing H<sub>2</sub>O

by  $\text{H}_3\text{PO}_4$  as a counter-reactant. g) ZnS deposited onto silica spheres by the same liquid phase method using diethyl zinc and hydrogen sulfide as reactants. h-n) Elemental mapping of the corresponding coated samples above using scanning transmission electron microscopy with an energy disperse X-ray detector.

A series of materials was prepared by performing several cycles with saturating quantities of TMA and water as measured by the results of the aforementioned titrations (**Figure 3.3**), using a round-bottom flask under a fumehood (**Figure B-3**). Silica nanospheres were coated with 10 TMA/water cycles in order to clearly assess the overcoating density and conformality (**Figure 3.3 A-C**). As a benchmark, we performed a conventional gas-phase ALD coating in a fluidized bed reactor (FBR) at  $140^\circ\text{C}$  under reduced pressure ( $<1$  torr) (**Figure 3.3 A**). The coating quality and conformality were identical with no uncoated or partially coated particles being observed in either case. We always observed an absence of agglomeration and did not observe any alumina on the surface (additional images comparing the methods are shown in **Figure B-4**). Interestingly, the layer deposited in solution was actually thinner (1.5 nm versus 3 nm) and closer to what would be expected for 10 monolayers of alumina ( $\sim 1$  nm) deposited by TMA/ $\text{H}_2\text{O}$  cycles.<sup>[234]</sup> The thicker layer in FBR-ALD could be indicative of a CVD growth mechanism occurring in the FBR where the water was likely not fully desorbed between the cycles at  $140^\circ\text{C}$ .<sup>[97]</sup> The two materials were also compared by solid state NMR, X-ray diffraction (XRD) and X-ray photoemission spectroscopy (XPS) (**Figure B-5**, **Figure B-6**, **Figure B-7**). These chemical and structural analyses confirmed that, in both cases, amorphous alumina was present and that the aluminum was in the same chemical environment.

Importantly, scaling up the coating procedure using our method was simple and inexpensive. We prepared a batch of 158g of coated silica, using the same conditions with a bigger round-bottom flask and more concentrated injections. The quality of the coating was completely unaffected (**Figure 3.3 C**) and no unattached aluminum or agglomeration was observed by STEM-EDX (**Figure 3.3 H-J**). The stoichiometrically limited method can be applied to numerous materials, both for coatings and supports. We used the same approach applied for alumina growth on silica to coat higher surface area and basic material such as magnesia (**Figure 3.3 d** and **Figure B-8**) with alumina.

The aforementioned materials were prepared by injections separated by 30 min, without any purging or drying steps. After further optimization, we were able to reduce the time between injections to 10 min while maintaining coating quality (**Figure B-9**). The material prepared by FBR-ALD followed this sequence: TMA injection (4min), purge (40min), water injection (4min) and purge (40min). The optimal FBR-ALD sequence can depend on the setup, but in our case, shorter injection times led to incomplete coverage. This sequence corresponds to a huge excess of precursor and large amounts of purging gas. In contrast, stoichiometric injections, regardless of the time between injections, use no excess of precursor, which could tremendously reduce ALD processing costs. The disadvantage of the method presented here is that it does require an initial sacrificial titration run to characterize the quantities required for injection. However, this would quickly become worthwhile for a large batch of precursor. Gas-phase ALD coatings on wafers are significantly shorter ( $< 1$  sec per cycle) and thus are much easier to scale up compared to gas-phase ALD on high surface area substrates.

To further demonstrate the versatility of our method, a high surface area silica (KCC-1) that is typically used in heterogeneous catalysis was also coated with 10 cycles of TMA/water. STEM-EDX mapping (**Figure 3.3 L** and **Figure B-10**) confirmed the deposition of alumina within pores, and once

again no freestanding alumina was detected. N<sub>2</sub> physisorption analysis (**Figure B-11**) showed an expected decrease of the BET surface area from 356 to 242 m<sup>2</sup>/g due to the reduction in pore size, but also a preservation of some micro- and mesoporosity. The remaining porosity confirmed that the deposition did not simply occur on the outer shell and did not clog pores, which could negatively affect catalysis.

We also wanted to demonstrate that certain coatings that cannot be achieved in the gas phase can be done using liquid-phase stoichiometrically limited injections. One such example is the deposition of phosphates including aluminum phosphates. This can be done in conventional ALD, but requires 6 steps with 3 reactants to perform self-limited reactions, including more expensive sources of phosphorus such as trimethylphosphate or triethylphosphate.<sup>[121,241,242]</sup>

Phosphate deposition in gas phase is challenging due to the low volatility of many phosphate precursors. Sol-gel approaches are easier but do not provide the same degree of accuracy.<sup>[242]</sup> Here, we were able to deposit high-quality aluminum phosphate coatings on silica using our conventional two injections with TMA and inexpensive phosphoric acid (**Figure 3.3 F and M** and **Figure B-12**). The phosphate structure was confirmed by solid state aluminum and phosphorous NMR as well as by XPS (**Figure B-13** and **Figure B-14**).

Finally, we demonstrate that this method is not limited to aluminum chemistry by depositing zinc sulfide (ZnS) using alternating injections of a solution of diethyl zinc and a solution of hydrogen sulfide. The resulting deposition on silica spheres showed a conformal coating, without external precipitation or agglomeration (**Figure 3.3 G and n** and **Figure B-15**). However, the coating featured multiple homogeneously dispersed ZnS crystallites surrounded by an amorphous phase (**Figure B-15**), leading to a rougher coating. Both the presence of a rougher coating and the presence of crystallites were systematically observed in gas-phase ALD when depositing ZnS, showing that the liquid-phase method leads to comparable results.<sup>[243–245]</sup>



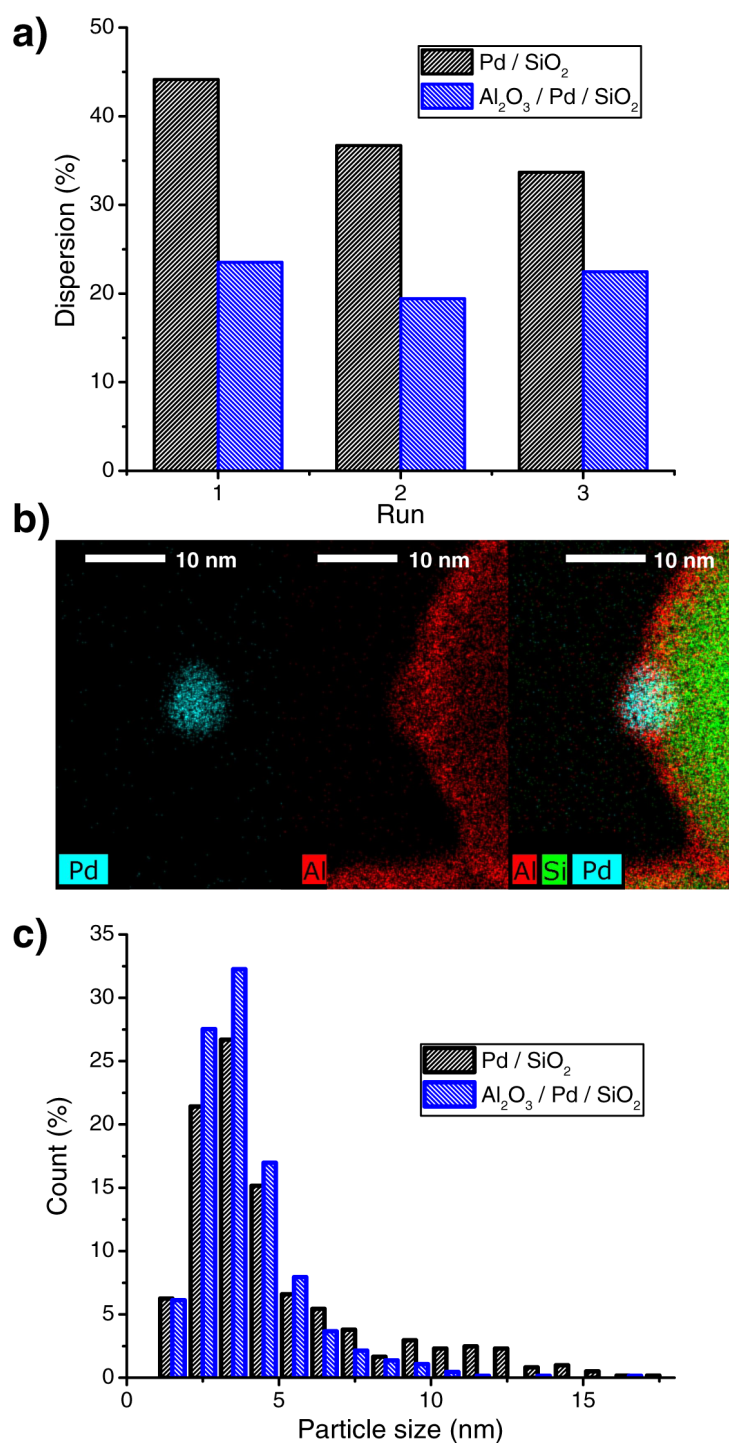


**Figure 3.4** a) Evolution of the dispersion measured by pulse CO chemisorption and Temperature Programmed Reduction (TPR) of bare and coated Palladium catalyst during several thermal aging cycles (oxidation/reduction). b) STEM-EDX pictures of supported palladium nanoparticles on silica coated with 20 cycles of stoichiometrically injected alumina. c) Particle size distribution of both protected and unprotected catalysts, measured by TEM.

To illustrate this concept for use in catalysis, a model catalyst of palladium nanoparticles supported on silica was prepared to study the ability of the overcoat to prevent nanoparticle sintering, which is a common deactivation mechanism in catalysis that has been hindered in several studies by gas-phase

ALD processes.<sup>[140,145]</sup> To test the effectiveness of our method for this application, cycles of oxidation and reduction were repeated on coated (20 cycles) and uncoated catalysts. The uncoated palladium catalyst started with a relatively high quantity of accessible palladium but its dispersion decreased with each thermal treatment, which was the result of sintering (**Figure 3.4 A**). In comparison, the coated catalyst had fewer accessible palladium sites due to overage by the overcoat (**Figure 3.4 B**), but this accessibility remained unaffected by thermal treatments, indicating that sintering had been curtailed. These results were also supported by the particle size distribution after the third thermal treatment measured over 600 particles per sample (**Figure 3.4 C**). By comparing protected and unprotected catalyst, the population of 2.5-5 nm particles is lower in the case of bare catalyst, and a significant number of particles above 10 nm are visible, while almost none are visible when the catalyst is protected. This particle size distribution indicates that, contrary to the protected catalyst, the bare catalyst suffered from the thermally activated merging of its nanoparticles (also visible in **Figure B-16**).

### 3.4 Experimental Section

All chemicals were purchased anhydrous or dried over molecular sieves (4 angstroms, Merk) and stored in a glovebox (typically <0.5ppm H<sub>2</sub>O and <.5ppm O<sub>2</sub>). Dibutyl ether (DBE) 99+%, tetraorthosilicate (TEOS, 98%) and methyl magnesium bromide (3M in ether) were purchased from Acros organic. Anhydrous dioxane 99.8% was purchased from ABCR. Trimethyl aluminum (TMA, 2M in heptane), phosphoric acid, HCl (2M in ether), diethyl zinc (1M in heptane) and hydrogen sulfide (0.8M in THF) were purchased from Sigma Aldrich. MgO was purchased from Fluka. High-surface area silica was purchased from Strem. Silica spheres were prepared using a previously described method adapted from Stöber<sup>[231,246]</sup>. The density of hydroxyl groups was measured by methyl magnesium bromide titration as previously described.<sup>[247-249]</sup> The supported palladium catalyst was prepared according to a published method.<sup>[145]</sup> A short description of the methods is provided in Chapter 2B.2.

Surface titration with the precursors was performed as follows. A round bottom flask (250mL) and a Schlenk tube (25mL) were put in a glovebox, in which the powder, the solvent and a magnetic stirrer were loaded. A TMA solution was prepared by diluting the commercial solution into DBE using a volumetric flask. Then, the solution was transferred to the Schlenk tube. All glassware was sealed by a rubber septum and taken out of the glovebox to a fume hood equipped with a Schlenk line. The reactor was stirred for 15 min to ensure dispersion of the powder. The titration sequence consisted of the addition of the precursor solution by injection with a syringe to the stirred powder at room temperature, followed by 40 min for reaction. After this time, gas samples were taken with a gas tight syringe and injected into a GC-FID for methane quantification. The sequence was repeated until the saturation point was clearly reached. A slight increase of methane after saturation (0.01-0.3 CH<sub>4</sub>/Al) was attributed to vapors of TMA caught by the gas syringe, which then hydrolyzed inside the GC's injector (the resulting minor slope was discounted during the determination of the saturation point, Figure B-17). This vapor pressure of TMA is only present when titration was carried out beyond stoichiometric saturation and thus is not present during the actual overcoating.

The same titration procedure that was used for TMA was followed for water titration, except that the water solution was prepared out of the glovebox, where typically 0.2 mL of water was added to a Schlenk tube containing 40 mL of dry dioxane. Further experimental considerations for the aluminum precursor selection, choice of solvent and water titration are discussed in chapter B.

Multiple liquid-phase cycles of atomic layer deposition on powders were performed by simply extending the surface titration procedure. Solutions of TMA in DBE and water in dioxane (in case of alumina deposition) were prepared in Schlenk tubes. The powder was loaded in a glovebox and the calculated volume of the precursor solution necessary to reach the stoichiometric saturation quantity measured by titration was injected at each cycle. Evacuation of the resulting methane was facilitated through a bubbler connected to a second neck of the round-bottom flask, or simply released by syringe depending on the quantity of methane expected (**Figure B-3**). For the deposition of aluminum phosphate, we used DBE to disperse the substrate and as the solvent for both the TMA and phosphoric acid injections. For experiments involving H<sub>2</sub>S, the substrate was dispersed in DBE and solutions of diethyl zinc in heptane and H<sub>2</sub>S in THF were used for injections. The latter procedure was carried out entirely inside a glovebox.

Fluidized Bed Reactor ALD (FBR-ALD) was performed using a Beneq TFS 200 instrument, the reactor chamber was set at 140 °C under reduced pressure (<1 mbar) and shaken with vibrations. Typical exposure and purge time was: 6 min TMA injection – 40 min purge – 4 min H<sub>2</sub>O injection – 40 min purge for a single cycle with 2g of substrate being coated.

Electron microscopy was performed on a FEI Talos with 200 keV acceleration voltage, where samples were dry impregnated on Lacey carbon grids.

Methane was systematically quantified using a Perkin Elmer Autosystem GC with a plot Q column and Flame Ionisation Detector (FID). N<sub>2</sub> physisorption was performed using a Micromeritics 3 flex at 77 K, where the measurement was preceded by *in situ* drying at 120°C. CO titrations (at 30°C) and TPRs (600°C, 20 °C/min) were recorded on a Micromeritics Autochem II with a Thermal Conductivity Detector (TCD). Solid state NMR was performed at 9.4 T on a Bruker AVIII HD spectrometer with a 2.5mm triple channel solid state probe set at a spinning speed of 30kHz recording 4096 scans. The XPS measurements were performed on a Phi Versa Probe II with an aluminum anode at 50 W. The C1s peak at 284.8 eV was used as a reference and the spectra were recorded with steps of 0.2 eV. The data were processed using CasaXPS.

### 3.5 Conclusion

In summary, atomic layer deposition (ALD) on high-surface area dispersed materials was performed using stoichiometrically limited injections in liquid phase, at room temperature and pressure without any gas-phase ALD apparatus. Coating qualities were maintained despite the simple conditions that were employed. We also avoided the use of any excess precursor, counter-reactants or purging fluid. Liquid-phase conditions also allowed us to perform several coating operations that are not possible in gas phase. We also demonstrated the applicability of this method to heterogeneous catalysts because this method could greatly democratize the use of ALD on dispersed materials; both at laboratory scale and, notably, for industrial catalyst preparation.

### 3.5.1 Supporting Information

Supporting Information are available in chapter B.

### 3.5.2 Acknowledgements

This work was supported by the European Research Council (ERC) under the European Union's Horizon 2020 research and innovation program (Starting grant: CATACOAT, No. 758653) and by EPFL. This work was also accomplished within the framework of the Swiss Competence Center for Bioenergy Research (SCCER-BIOSWEET). The authors also thank EPFL's interdisciplinary center for electron microscopy for support during electron microscopy measurements. The authors thank Aurelien Bornet for help with solid state NMR measurements, Pascal Schouwink for PXRD and Mounir Mensi for help with XPS measurements. The authors also thanks Professor Kevin Sivula for his guidance.



# Chapter 4 Atom-by-atom design of catalytic clusters

In this chapter, I focus on the early stages of liquid phase ALD nucleation. As observed in the previous chapter, controlling the hydroxyl density of a silica surface is a straightforward way to switch from film growth to island growth. In the case of island growth, the size and composition of the clusters can be controlled simply and with atomic accuracy by the number of cycles deposited and the nature of the precursor.

In the field of heterogeneous catalysis, controlling nucleation with such precision offers many possibilities. It would notably allow, for instance, to maximize the interface between the support and the deposited material. Supported clusters are extremely challenging to prepare, as their small size makes them relatively unstable and tools for controlling nucleation are limited. This is an opportunity where the atomic accuracy of ALD combined with the mild conditions of a liquid phase synthesis can be fully exploited.

This work aims to go beyond the limitations of gas-phase ALD. While nucleation is a known phenomena, it is generally uncontrolled and unwanted<sup>[133]</sup>. New approaches, such as “area-selective ALD” are used to limit the size of nanoparticles and/or prevent the formation of a continuous layer. However, these methods cannot reach atomic accuracy<sup>[134,250]</sup>. Surface dihydroxylation is difficult to use in gas phase ALD as water would rehydroxylate the surface at high temperature or simply adsorb to the surface at lower temperatures<sup>[97]</sup>.

Contributions:

- Raphael Schnyder participated in the optimization of the synthetic procedure as well as some of the catalytic tests.
- Louisa M. Savereide participated in the data processing of catalytic results.
- Mounir Mensi conducted XPS measurement and participated in their interpretation.
- Experimental and material design, material preparation, most of the catalytic tests in stainless steel and quartz reactor, DRIFTS measurements, and the electron microscopy were performed by me.

# Atom-by-atom heterogeneous catalyst design for a better understanding of individual and collective behaviors

Benjamin P. Le Monnier, Raphael Schnyder, Louisa M. Savereide, Mounir Mensi and Jeremy S. Luterbacher

École Fédérale Polytechnique de Lausanne, Switzerland

## 4.1 Abstract

We present a new approach for preparing and studying multi-atom active sites in heterogeneous catalysts. The principle relies on the controlled nucleation of hetero metal oxide clusters on a silica surface by liquid-phase atomic layer deposition (ALD). Starting with a model single-atom zinc catalyst, we were able to prepare a series of catalysts, each of them with a different, well-defined atomically precise structures. Comparisons between these materials allowed us to draw conclusions regarding the beneficial effects of aluminum and silicon within the second coordination sphere of the active zinc on activity and stability catalytic propane dehydrogenation. The influence of the surrounding environment on the zinc behavior was thoroughly studied by diffuse reflectance infrared Fourier transform spectroscopy (DRIFTS), X-ray photoelectron spectroscopy (XPS), transmission electron microscopy (TEM), and extensive catalytic testing.

## 4.2 Introduction

Heterogeneous catalyst surfaces are complex environments characterized by a great diversity of compositions and structures that are not yet fully understood. For example, a catalyst made of supported nanoparticles on a porous support contains many different active atoms, each potentially behaving in a different way (atoms embedded within a crystallographic plane, at a corner, at the metal-support interface, etc.)<sup>[57,59,251]</sup>. This broad distribution of behaviors is due to the varied and usually unknown surroundings of the active atom that control its properties<sup>[252]</sup>.

The chemical environment can play many roles depending on its elemental composition, structure, the nature of the active center, and the catalytic reaction involved<sup>[153,157]</sup>. Support effects have notably been leveraged in several systems to increase activity and/or selectivity even before they were truly characterized<sup>[253]</sup>. These phenomena have been described as support-metal interactions (and characterized as weak, medium or strong)<sup>[157]</sup>, promotion effects<sup>[254,255]</sup>, synergy<sup>[256–258]</sup> and cooperativity<sup>[87,259,260]</sup>.

Thanks to progress in characterization techniques including X-ray absorption spectroscopy<sup>[261]</sup>, density functional theory<sup>[262]</sup>, solid-state NMR<sup>[263,264]</sup>, electron and microscopy<sup>[265]</sup>, the effects of the support on the active site are slowly being better understood. However, two main issues complicate the characterization of these sites, namely: differentiating atoms based on their surrounding and/or the low concentration of the active site of interest within the overall material.

The aim of this project is to develop a synthesis approach to prepare uniform well-defined active sites containing more than one element. In contrast to a typical catalyst containing multiple types of active sites due to lack of control during the preparation, the goal here is to prepare a series of catalysts, each with only one type of site. Synthesizing a homogeneous catalytic cluster with a controlled structure will allow us to individually test certain atomic effects including promotion and cooperativity effects. Such systems could greatly facilitate the elucidation of structure-function relationships and ultimately better design future catalysts.

The synthesis strategy for highly uniform multinuclear sites relies on liquid phase atomic layer deposition (ALD). This technique, traditionally used in the microelectronic field, is increasingly used in electrode preparation (batteries, fuel cells, solar cells) and encapsulation (quantum dots and heterogeneous catalysts)<sup>[99–101,110]</sup> and is especially well suited for this objective as it offers control of both the structure and composition of the surface species (**Figure 4.1**).

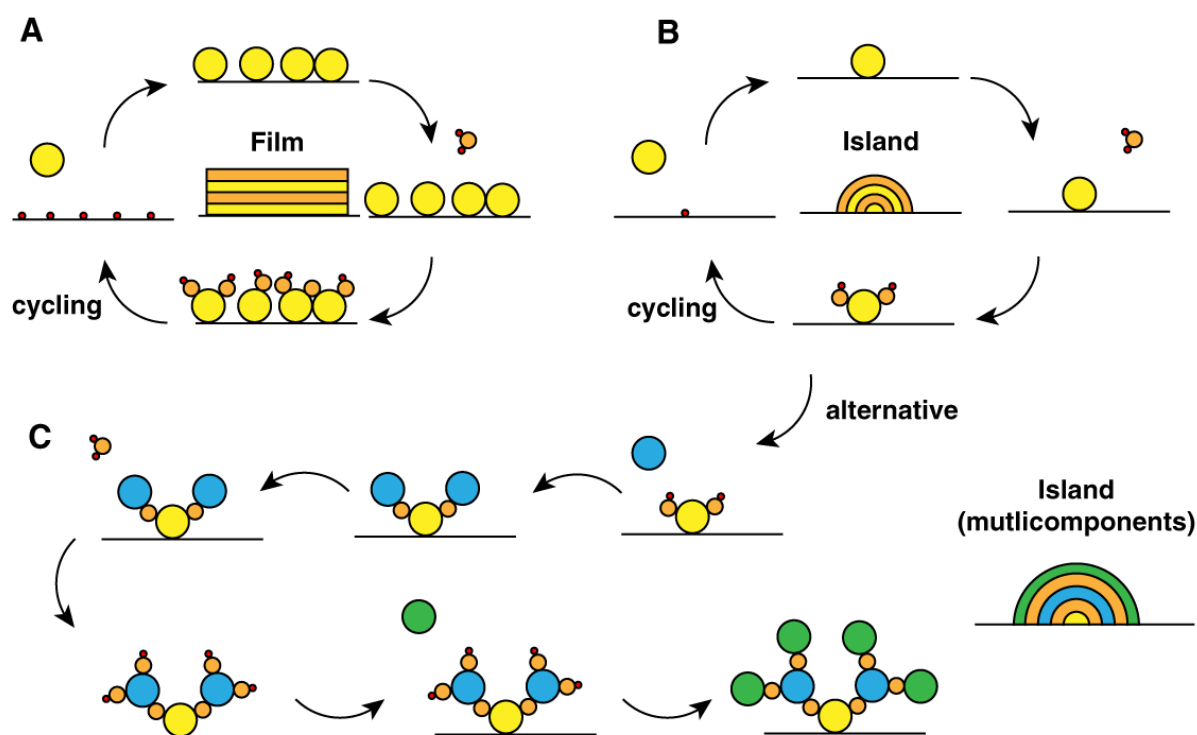


**Figure 4.1:** Schematic representation of different types of growth modes in atomic layer deposition (ALD) that could be leveraged in heterogeneous catalyst preparation. (A) ALD cycles on a surface densely covered with nucleation sites. A compact monolayer can be grafted on a surface, leading to a film growth<sup>[105]</sup>. (B) ALD cycles on a surface with a low concentration of nucleation site. In this case, a relatively large distance separates the grafted precursors leading to island formation<sup>[133]</sup>. (C) ALD “island” growth when injecting different precursor at each cycle. In this case, the sequence is not a binary loop. Instead, each cycle can feature a different component.

In a previous study, we demonstrated that ALD can be performed in liquid phase on heterogeneous catalysts<sup>[266]</sup>. Benefits of this technique include that it requires only low-cost equipment, a small amount of precursor, and is conducted at room temperature. Additionally, results of this previous work indicated that nucleation on sufficiently dehydroxylated silica can be controlled as the mild

reaction temperature seemed to prevent the formation of new nucleation sites. The current study aims to take advantage of these features.

### 4.3 Results and discussion

The starting point of cluster growth is a nucleation site where the first precursor will attach. In the case of silica, these nucleation sites are the surface hydroxyl groups. Their concentration can be easily tuned by vacuum treatment at high temperature. The fully saturated hydroxyl density of silica is  $4.9 \text{ OH/nm}^2$ , which can be decreased to  $0.6 \text{ OH/nm}^2$  by treating the silica at  $800^\circ\text{C}$  under vacuum<sup>[97]</sup>. The hydroxyl surface concentration is equivalent to an average distance between sites of  $0.7 \text{ nm}$ , which is usually considered sufficient to assume the sites are distant enough to not interact with each other.<sup>[267]</sup>

These assumptions can be confirmed by measuring the stoichiometry of the deposition. Specifically, surface titration of the anchoring sites using diethyl zinc and trimethyl aluminum (**Figure 4.2 A**) was performed by measuring ligand release upon surface reactions when adding aluminum or zinc precursors. The results confirm the quantity of available hydroxyl groups measured by the well-established Grignard titration. All titrations led to the same measured anchoring site density, and the slope of one methane per aluminum confirms that hydroxyl groups are too far apart to form a bridging complex with a single precursor.

After titration, the full coverage was further confirmed by Diffuse Reflectance Infrared Fourier Transform Spectroscopy (DRIFTS) (**Figure 4.2 B**). Before deposition, a sharp peak at  $3750 \text{ cm}^{-1}$  was attributed to isolated hydroxyl groups. This result is consistent with the low hydroxyl concentration previously measured. After injection of a stoichiometric amount of trimethyl aluminum (determined from the titration), the peak corresponding to hydroxyl groups almost completely disappears. When normalizing the spectra to the peaks of bulk  $\text{SiO}_2$  ( $1190 \text{ cm}^{-1}$ )<sup>[268]</sup>, we calculated that more than 97% of the hydroxyl groups were consumed. The 3% remaining can be both attributed to small errors in the titration, inaccessible hydroxyl groups, or imprecisions in the injection volume.

Further titrations with water and zinc precursors provided values consistent with a branched structure (**Figure 4.2 C**). On a theoretical basis, if the aluminum reacts once with the surface, two methyl groups remain hydrolysable. This is confirmed by a water titration that led to a water/aluminum ratio of 2. The stoichiometry of water needed to fully hydrolyze the grafted aluminum also indicates that no water is consumed by potential surface rehydroxylation by cleavage of Si-O-Si bridges. The two resulting pending groups can then react with more added zinc precursors. From the quantity of zinc added, and the ratio methane over zinc of one before saturation, we can assume only linear growth is occurring (e.g. no ring formation).

Based on these values, several Zn and Al-based catalysts were prepared (**Figure 4.2 D**). Such a library enables us to separate composition and structural effects. The single site “Zn” catalyst is well known and was prepared by grafting diethyl zinc on dehydroxylated silica.<sup>[183]</sup> The “Al” catalyst was the equivalent single atom catalyst made exclusively of grafted aluminum from trimethyl aluminum. “Zn/Al” was prepared by the deposition sequence that features trimethyl aluminum – water – diethyl

zinc, hence, Zn represent a second layer on top of Al. The catalyst “Al/Zn” was prepared by the deposition sequence that features diethyl zinc – water – trimethyl aluminum. For the later deposition, titration of water and aluminum were performed to confirm the stoichiometry. In this case, the zinc atom was directly connected to the silica surface and, thus there was half as much zinc compared to the “Zn/Al” case. Finally, the “Si/Zn/Al” catalyst was prepared by the deposition sequence that features trimethyl aluminum – water – zinc – water – silicon precursor. The silicon precursors were not titrated, but were chosen so as to be able to react only once with a hydroxyl group (i.e. they contained only one hydrolysable function). Knowing the quantity of the pending hydroxyl group, a stoichiometric equivalent of silicon precursor was added. Silicon hydrolysis and condensation is known to be slower than aluminum or zinc, so the catalyst was stirred overnight at room temperature after injection of the Si precursor. Three precursors were investigated in this study: trimethyl chlorosilane, trimethyl methoxysilane and trimethyl methoxysilane using anhydrous pyridine as the catalyst.

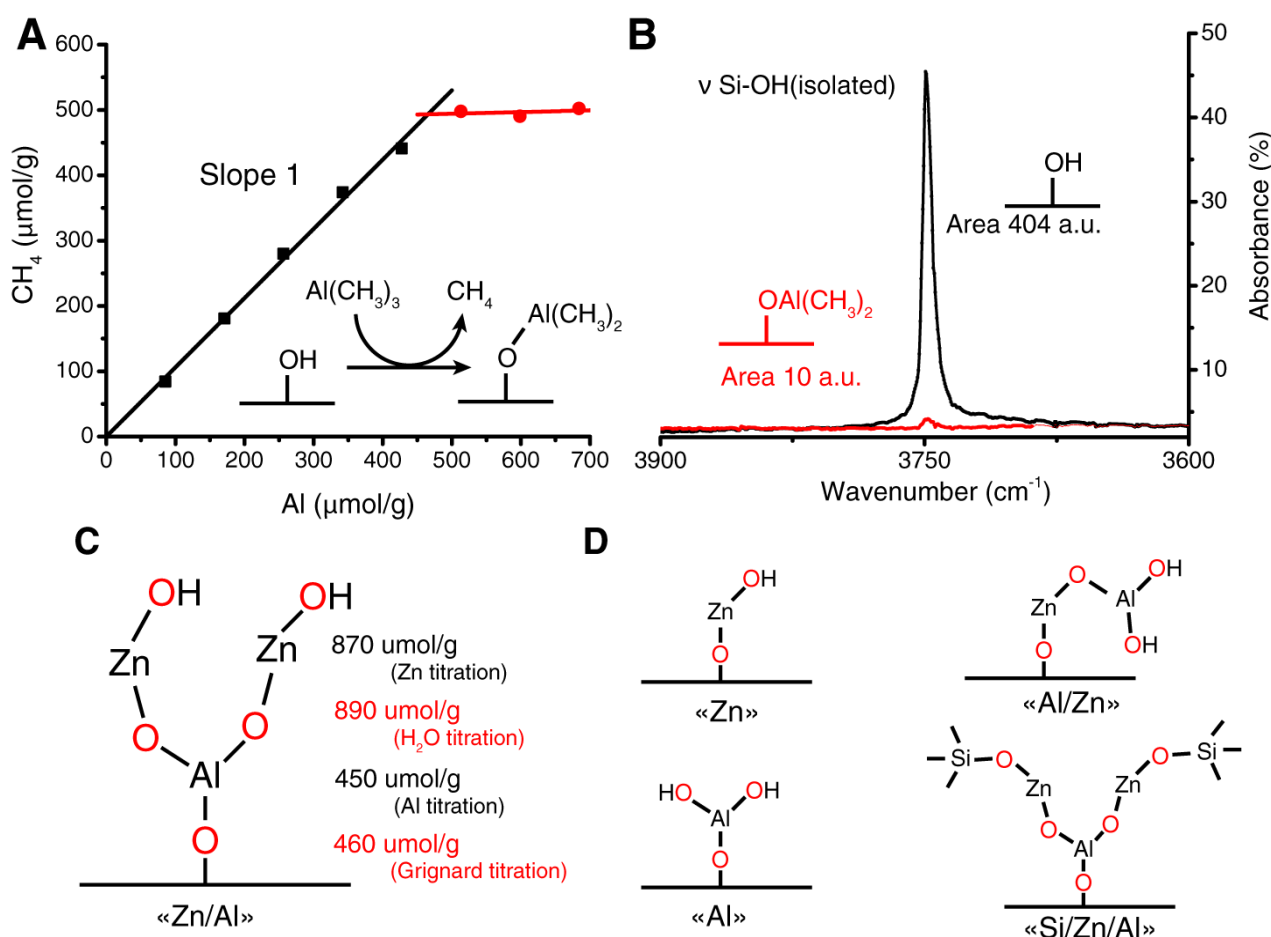


**Figure 4.2:** (A) trimethyl aluminum titration plots showing methane release following hydrolysis of the methyl ligands until full conversion of the surface hydroxyl groups. (B) DRIFTS spectra of dehydroxylated silica (black curve) and the same material after injection of exactly one aluminum monolayer (red curve). The full spectra are shown in **Figure C.1** (C) Schematic representation of the “Zn/Al” catalyst with the stoichiometries determined using Grignard, aluminum, water and zinc titrations, these results were confirmed by XPS (Zn/Al ratio of 1.9). (D) Schematic representation of the various catalysts, as prepared, at room temperature and in solvent. Considering the high temper-

ature of reaction (550°C) and the consequent removal of solvent, all atoms are considered to be directly bond to the surface by covalent or dative bond during the catalytic run. The methyl groups on the silicon atoms are also expected to be burnt off.

The presence and the homogenous distribution of Zn and Al in the catalyst were confirmed by XPS and scanning transmission electron microscopy with an energy dispersive X-ray detector (STEM-EDX) (**Figure 4.3** and **Figure C.2**).

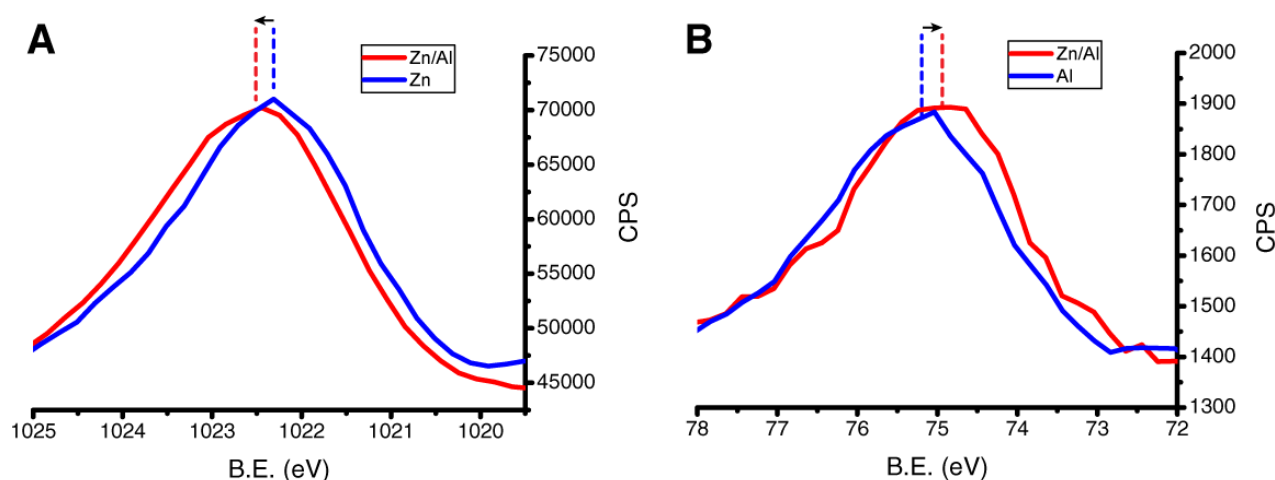


**Figure 4.3:** X-ray Photoelectron Spectra of Zn, Al and Zn/Al catalysts. (A) Zn 2p peak showing a shift from lower to higher binding energy when both metals are present within the cluster on the silica surface. (B) Al 2p peak showing a shift from higher to lower binding energy when both metals are present within the cluster on the silica surface.

Confirming by the proximity of Al and Zn elements in “Zn/Al” or “Al/Zn” is technically challenging. The metal concentrations are very low due to the required low density of anchoring sites, and there is a relatively large distance between the two elements (second coordination sphere). XPS analysis (**Figure 4.3**) provides some information on the surface structure, as the binding energy of electrons is related to the chemical environment. When comparing the Zn binding energy of the orbital 2p in case of “Zn” and “Zn/Al”, a small but significant shift towards higher binding energies. This shift would be consistent with the donating of electronic density to a close neighbor<sup>[269]</sup>. In contrast, a comparison of the “Al” and “Zn/Al” spectra shows a shift towards lower binding energies, indicating a higher electronic density on Zn. From the data that for the “Zn/Al” material, the Zn appears to have a lower electron density and the Al appears to have a higher electron density, which appears to indicate that these two elements are close enough to interact with each other electronically.

Catalytic tests were performed to understand the influence of the clusters’ structure on their activity. Propane dehydrogenation to propylene was selected as a model reaction, as Zn is a known catalyst for this reaction<sup>[183,270]</sup>. The choice of a gas-phase reaction was also made because single-atom catalysts are relatively fragile and prone to leach in liquid phase.

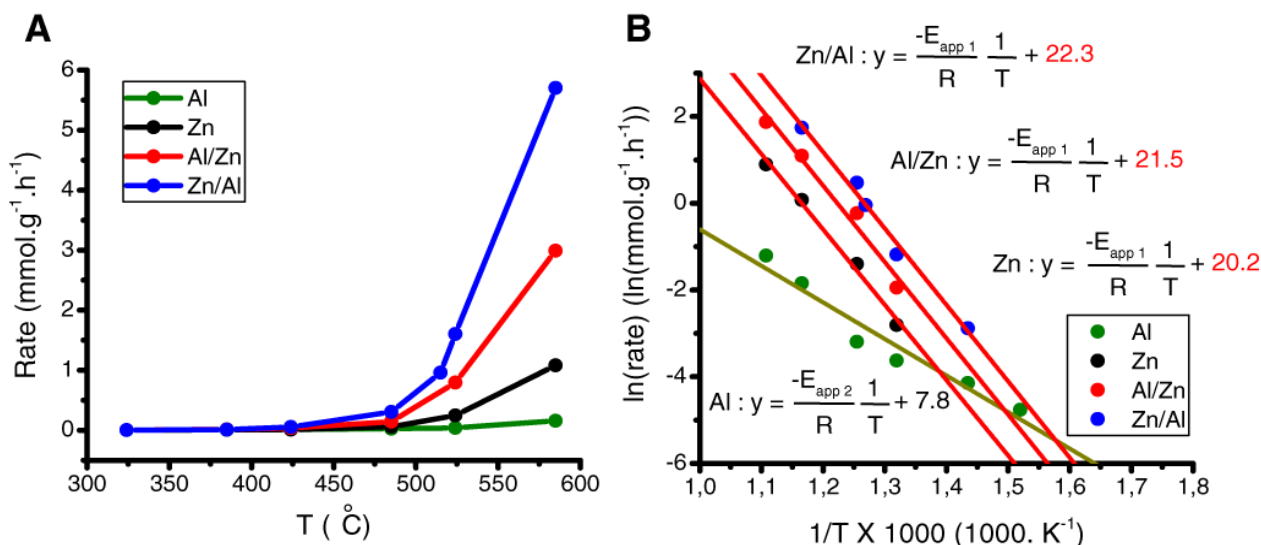


**Figure 4.4:** (A) Temperature Programmed Reaction (TPR) of aluminum- and zinc- based catalysts showing the rate of propylene production versus temperature. (B) Arrhenius plots corresponding to the activity between 325 °C and 580 °C.

The initial activity of the catalysts (**Figure 4.4A**) was compared by measuring dehydrogenation activity at temperatures ranging from 325 °C and 580 °C. Notably, we found that single atoms of aluminum are barely active for propane dehydrogenation. The activity of “Al/Zn” was measured to be 3 times higher than “Zn” catalyst despite having the same quantity of Zn atoms. Three hypotheses could explain such a rise in activity: the activity of Zn was increased by the presence of Al, the activity of Al was (drastically) increased by the presence of Zn or the proximity of Al and Zn led to the formation of a specific site, which was more active than either isolated Zn or Al sites. Interestingly, the activity of “Zn/Al” was almost exactly twice as high as “Al/Zn”. Considering that the amount of Al was the same in both case, this result is incompatible with the activity being linked to an Al active site. However, this observation was compatible with the two other hypotheses as both the number of Zn are doubled, and the number of Al-O-Zn pair are doubled (with one Al atom being involved in two pairs).

To further understand the reason behind this improvement in catalytic activity, we used Arrhenius plots to compare the apparent activation energy ( $E_{app}$ ) and pre exponential factor of the different catalysts (**Figure 4.4 B**). From these measurements all Zn-containing catalyst, “Zn”, “Al/Zn” and “Zn/Al” appeared to have the same apparent activation energy (i.e. the same slope). This strongly suggests that the mechanism was the same in every case, and that the reaction happened on the zinc atom, the activity of which could be increased by the presence of a nearby aluminum. What differed in these three cases was the frequency factor. A higher pre exponential factor in the case of “Zn/Al” compared to “Al/Zn” was expected as one had twice as many active sites. However, the increase of in pre exponential factor from “Zn” to “Al/Zn” occurred despite the same quantity of Zn sites being present. From the transition state theory, a higher pre-exponential factor is related to higher entropy of the transition state<sup>[271]</sup>. This result indicates that the aluminum had an entropic effect, acting on the geometry (or mobility) of the transition state linked to the Zn atom. This could mean that zinc atoms are more loosely attached to the aluminum than silicon ones<sup>[271]</sup>.

The catalytic activities have also been measured over 24 hours of continuous reaction in quartz plug flow reactors (**Figure 4.5**). For those tests, the catalyst were calcined *in situ* at 550°C followed by a purge and a reduction (activation) step prior to catalysis. As expected from the TPRs, the initial activity decreased with the order “Zn/Al” > “Al/Zn” > “Zn”, and this order remained unchanged over time (**Figure 4.5A**). However, the ratio of activities was strongly affected by time on stream. While the activity of “Zn/Al” was initially 5 times greater than Zn, it ended up being “only” 3 times higher after 24 hours on stream. If we look at the relative final activity compared to initial activity (**Figure 4.5 B**), we observed that the two catalysts containing both aluminum and zinc deactivated similarly and faster than the “Zn” catalyst alone. One hypothesis would be that the Al-O-Zn is a weaker bridge than Si-O-Zn, hence the mobility of Zn on the surface would be increased and the production of less active ZnO agglomerates increased<sup>[183]</sup>. ZnO particles have been reported to be easily reduced into metallic Zn which could then leach off due its low melting point and relative volatility<sup>[272]</sup>. In such cases, we observed deposition of metal zinc downstream of the catalyst (**Figure C.3**). The agglomeration of Zn atoms was observed by STEM-EDX (**Figure C.4**) as well as emptied areas. Importantly, the aluminum distribution remained homogeneous after the catalytic run, indicating that the aluminum atoms were strongly attached to the surface but appeared to promote zinc mobility. This observation supports the hypothesis of a weaker oxygen bridge between the Zn and Al than Zn and Si.

We concluded that the activity was not dropping because of the formation of carbonaceous deposits formation because the catalyst remained white after the run and no carbon was found by STEM-EDX. When the reaction was run in stainless-steel tubing instead of quartz, iron leached from the inner wall to the catalyst and produced a large quantity of carbon (**Figure C.4**).

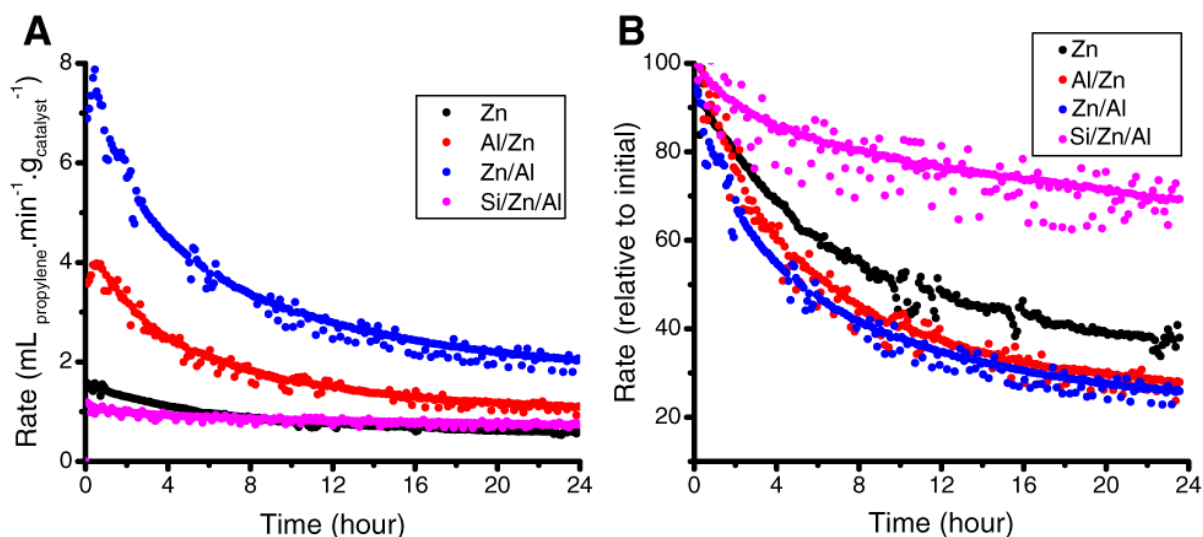


**Figure 4.5:** Catalytic tests in a quartz plug flow reactor at 1 atm, 50 mL/min flow rate (30% propane in He) at 550°C, with 100 mg of catalyst diluted in 0.5g of silicon carbide. (A) Rate of propylene production per time and mass of catalyst as a function of time on stream used to compare the absolute activity of the catalysts over time. (B) Relative rate normalized by the maximum initial activity to compare relative catalyst stability.



Following the hypothesis that a Zn is better attached by oxygen bridge to Si than Al, we attempted to anchor the clusters by grafting an extra layer of silicon. Stabilization of active site by adding an extra, thin and inert, layer is a common strategy in ALD used for heterogeneous catalysis<sup>[273–275]</sup>.

The first precursor we used was chloro trimethylsilane, which we selected because it is often used for silylation of organic compounds, and thus was assumed to be sufficiently reactive with pending hydroxyl groups on zinc atoms. In this case, the resulting catalytic results were identical as for “Al/Zn” (**Figure C.4**). Considering that two chlorinated compounds were added per cluster,  $\text{ZnCl}_2$  species could have been formed by ligand exchange. Zinc chloride is highly volatile, and considering the Cl/Zn ratio of two, it is possible that, starting from two Zn per Al, only one Zn per Al remained on the surface<sup>[276]</sup>. The next precursor we tested was trimethyl methoxysilane. The resulting condensation released methanol that should not bind strongly to zinc. The silicon precursor was left to react overnight with the pending hydroxyl group on top of the Zn grafted to Al. The catalytic activity results were unchanged compared to “Zn/Al”, indicating that the grafting likely did not occur because of the slow kinetics of the silicon precursor reaction (**Figure C.4**). Finally, this methoxy-based precursor was tested again but this time the grafting was assisted by pyridine, which was known to promote the condensation of a silicon alkoxide<sup>[277]</sup>. Pyridine catalysts have also been used in gas-phase ALD processes to catalyze silica deposition from silicon tetrachloride and water<sup>[278]</sup>. The advantages of pyridine were its solubility in the organic solvent and the fact that it can be burned off (in contrast to inorganic bases). The material prepared from methoxy-based silicon precursor assisted by pyridine was labeled “Si/Zn/Al”.

The behavior of “Si/Zn/Al” significantly differed from that of previous materials as it displayed the lowest initial activity and the highest stability (**Figure 4.5A and B**). While this catalyst started with a lower activity than the simple “Zn” catalyst, its final activity was higher. The evolution of its relative activity (**Figure 4.5 B**) followed a very different rate from that of all other catalysts. We suggest that two effects are causing the improvement in stability. First, the hypothetical stronger interaction Zn-O-Si should limit the Zn mobility but also sterically hinders the access of the propane to the Zn atom. Together, these effects increase stability but lower activity.

## 4.4 Conclusion

We demonstrated a route for the synthesis of supported, isolated, catalytic clusters using liquid-phase ALD. The procedure offers great control of both cluster structure and composition. We used this technique to synthesize different clusters based on a zinc single-atom catalyst. Addition of Aluminium in the second sphere of coordination around the active Zn center increased activity significantly which, using XPS and catalytic tests, highlighted the importance of this second sphere. The presence of Al-O-Zn bridge was found to have a positive effect on activity and a negative one on stability while Si-O-Zn had the inverse effect. Transmission electron microscopy revealed that the main mechanism of deactivation was caused by the irreversible gathering of Zn atoms followed by their leaching. In overall, it was demonstrated that, beyond being a tool for film deposition, liquid phase ALD is an asset for exploring structure-activity relationships of heterogeneous catalysts.

## 4.5 Experimental section

### *Support preparation*

High surface area silica was purchased from Strem chemicals dried in a quartz tube at 250°C (ramp 5°C/min, hold 2 hours) under dynamic vacuum (about  $1.10^{-2}$  mbar) to remove most of the physisorbed water. The dihydroxylation was driven by ramping the temperature to 800°C (ramp 2.5°C/min, hold 8 hours). The silica was then stored in a glovebox (typically <0.1ppm H<sub>2</sub>O and <.01ppm O<sub>2</sub>).

### *Surface titration*

A detailed description of the liquid-phase ALD procedure is given in the previous chapter and only a brief summary of the procedures is provided below.

Grignard titration was performed by adding an excess of methyl magnesium bromide (3M in ether, Sigma Aldrich) to a sealed round bottom flask containing the prepared silica. The methane released was measured by sampling with gas tight syringe and injected in a Perkin Elmer gas chromatography system equipped with a flame ionization detector (GC-FID).

Trimethyl aluminum and diethyl zinc titrations were performed as follows. In the glovebox, solutions of the target concentration were prepared by diluting commercial solutions with anhydrous dibutyl ether (purchased at Sigma Aldrich and dried over sodium/benzophenone) using a volumetric flask. The solution was transfer into sealed Schlenk tubes. The silica (typically 2g) was loaded into a round bottom flask with 20 mL of dibutyl ether before being capped with a septum.

The water solution was prepared from deionized water that was degassed for one hour by nitrogen bubbling. Typically 0.5 mL of water was added to a Schlenk tube containing 40 mL of anhydrous dioxane (purchased from Sigma Aldrich and dried with sodium/benzophenone).

All the glassware were transferred from the glovebox to a fumehood where the round bottom flask was held on a stirring plate (300 rpm) and the Schlenk tubes connected to a Schlenk line. A small volume of precursor solution was added to the round bottom flask and every 40 min, a gas sample was taken and measured by GC-FID to measure the methane released.

Before full coverage, a linear increase of methane released per reactant added is observed (slope of 1). After equivalence, a second slope (about 0.1 methane or ethane/precursor) is observed due to the vapor pressure of the reactant. The crossing point of these two lines gives the equivalent point.

### *Material preparation*

The setup for material preparation is the same as for the titration: round bottom flask containing dispersed support and Schlenk tubes containing precursor solutions. Each 40 min, reactants were added from the Schlenk tubes to the round bottom flask. After completion, the catalyst was collected by adding 5 mL of DI water and separated by centrifugation (3000 rpm, 3 min). The powders were washed twice with absolute ethanol to remove dibutyl ether prior to drying overnight at 120°C in a ventilated oven.

### *Catalytic tests*

The catalytic tests using a quartz reactor were performed using an Autochem II chemisorption setup (micromeritics). Typically, 100mg of catalyst were diluted in 0.5g of silicon carbide (purchased from...) to avoid overpressure. The catalyst were calcined in situ (using a ramp of 10 °C/min up to 550°C, and then held at 550°C for 30 min). Then, the air was purged out with He (30 min, 50mL/min) and the sample was reduced under 10% H<sub>2</sub> under argon flow (30 min, 50mL/min) and purged again with He (30 min, 50mL/min). The feed was then changed to the reactive mixture, at a total flow of 50 mL/min of 30% propane in He for 24 hours.

The reaction was monitored by an Agilent GC-FID connected to the outlet of the Autochem, injecting every 5 minutes. The data processing of the chromatograms was done using Matlab.

### *Characterizations*

Transmission electron microscopy was done using a Talos (FEI) transmission electron microscope working at 200 keV acceleration voltage. Samples were loaded on Lacey carbon grid by dry mixing.

Diffuse reflectance infrared Fourier transformed spectroscopy was performed using a Perkin Elmer IR with a sealed sample holder with KBr windows. The samples were loaded into the cell within the glovebox. The cell was then sealed and taken out for analysis.

The X-ray photoelectron spectroscopy (XPS) measurements were carried out on an Axis Supra (Kratos Analytical) using the monochromated K $\alpha$  X-ray line of an Aluminium anode. The pass energy was set to 40eV with a step size of 0.2eV. The samples were electrically insulated from the sample holder and charges were compensated. Spectra were referenced at 103.5eV using the SiO<sub>2</sub> bound of the Si2p transition.

Inductively couple plasma atomic emission spectroscopy (ICP-AES) was used to quantified metal loading and relative ratio. The sample was digested in concentrated nitric acid overnight to leach out grafted Al and Zn. The solution was filtered to remove particles of silica and analyzed without further treatment.

#### 4.5.1 Supplementary information

Supporting Information are available in chapter C.

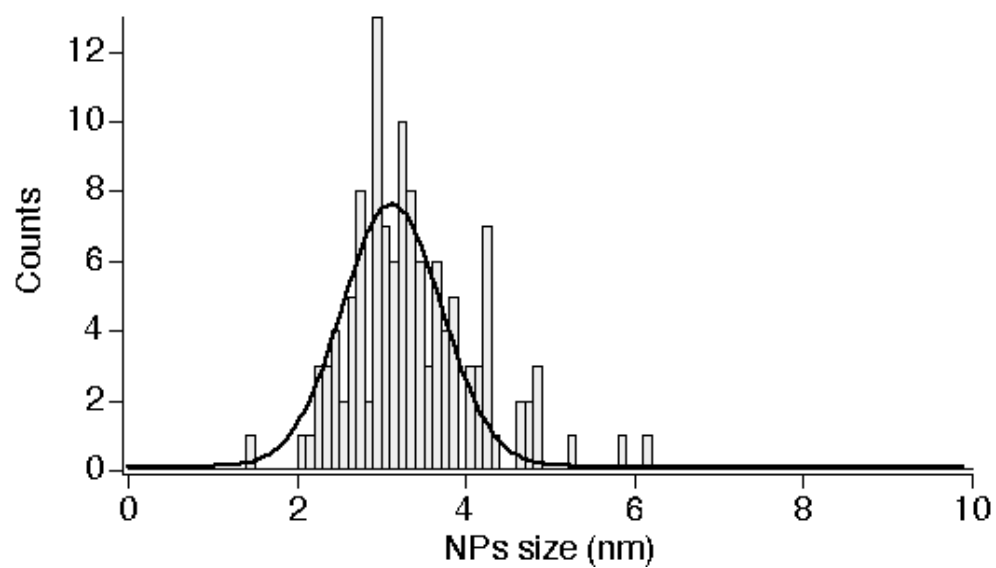
#### 4.5.2 Acknowledgements

This work was supported by the European Research Council (ERC) under the European Union's Horizon 2020 research and innovation program (Starting grant: CATACOAT, No. 758653) and by EPFL. This work was also accomplished within the framework of the Swiss Competence Center for Bioenergy Research (SCCER-BIOSWEET).

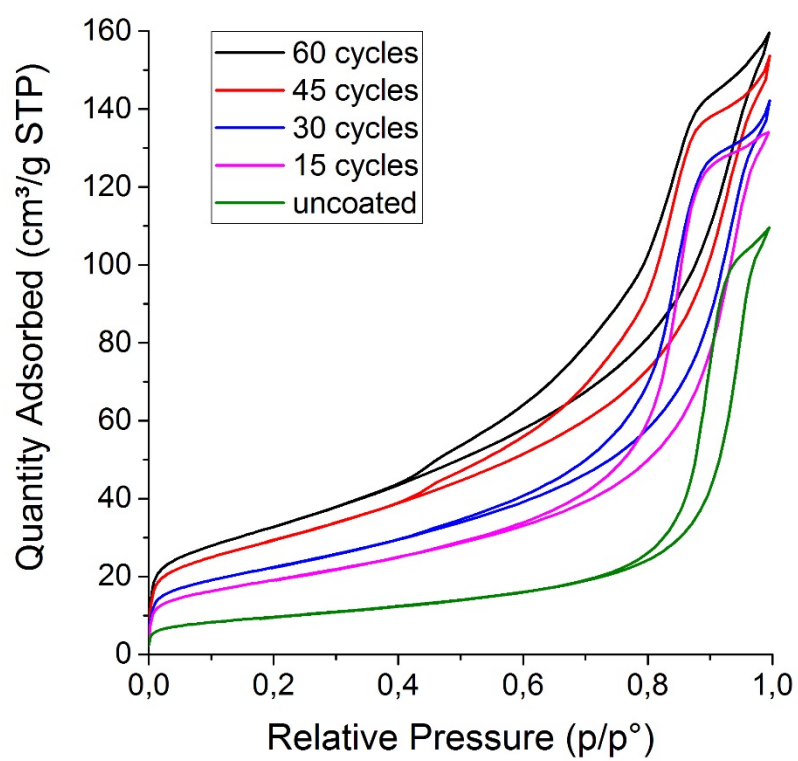


# ASupporting information of chapter 2

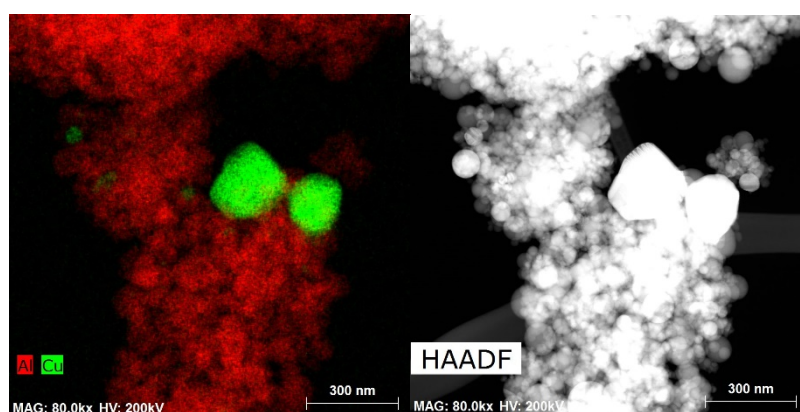
## A.1 Figures



**Figure A.1:** Particles size distribution for Cu/Al<sub>2</sub>O<sub>3</sub>.



**Figure A.2** :N<sub>2</sub> adsorption and desorption isotherms for Cu/Al<sub>2</sub>O<sub>3</sub> after deposition of 0, 15, 30, 45, and 60 Al<sub>2</sub>O<sub>3</sub> layers.



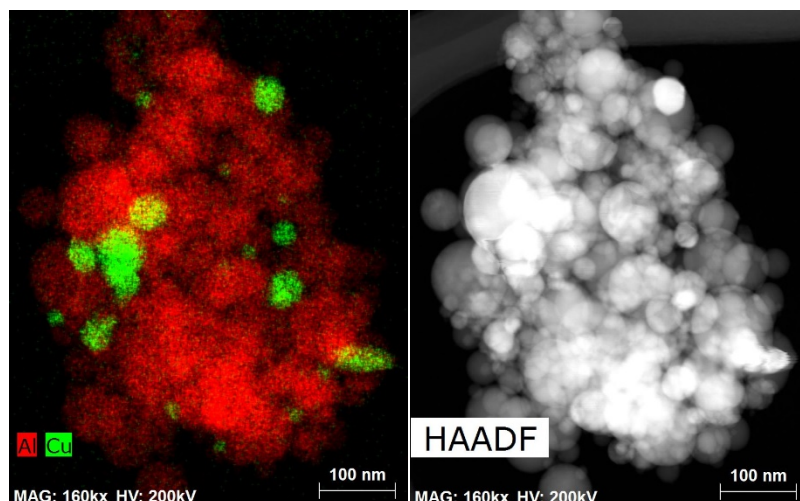


**Figure A.3:** HAADF STEM pictures and EDX maps for Cu/Al<sub>2</sub>O<sub>3</sub> after 5 catalytic cycles (during the liquid phase hydrogenation of furfural) showing copper sintering.

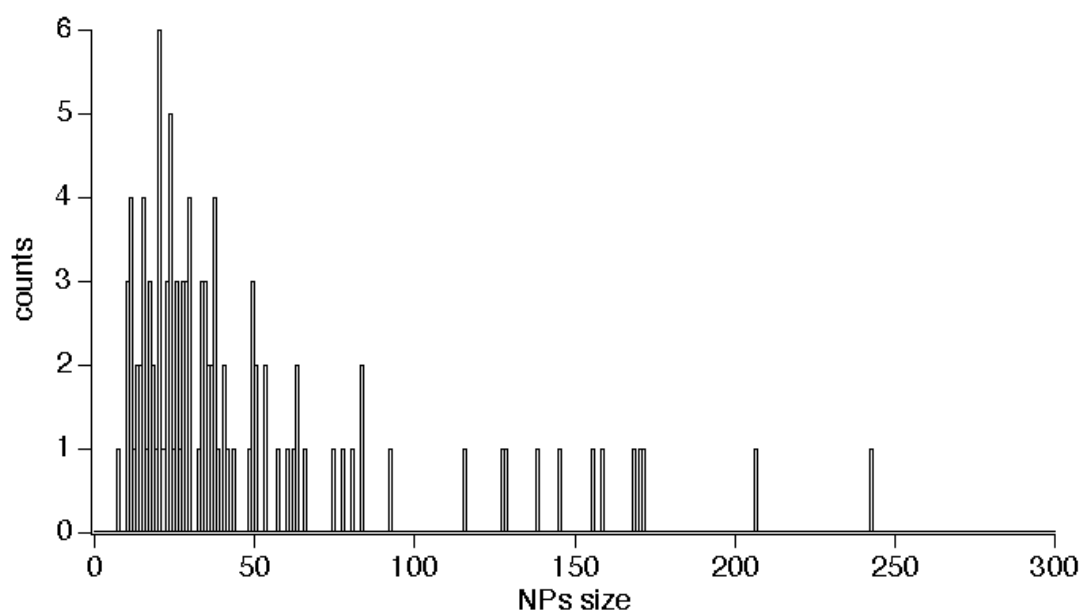


**Figure A.4:** Particles size distribution for Cu/Al<sub>2</sub>O<sub>3</sub> after 5 catalytic cycles (during the liquid phase hydrogenation of furfural).

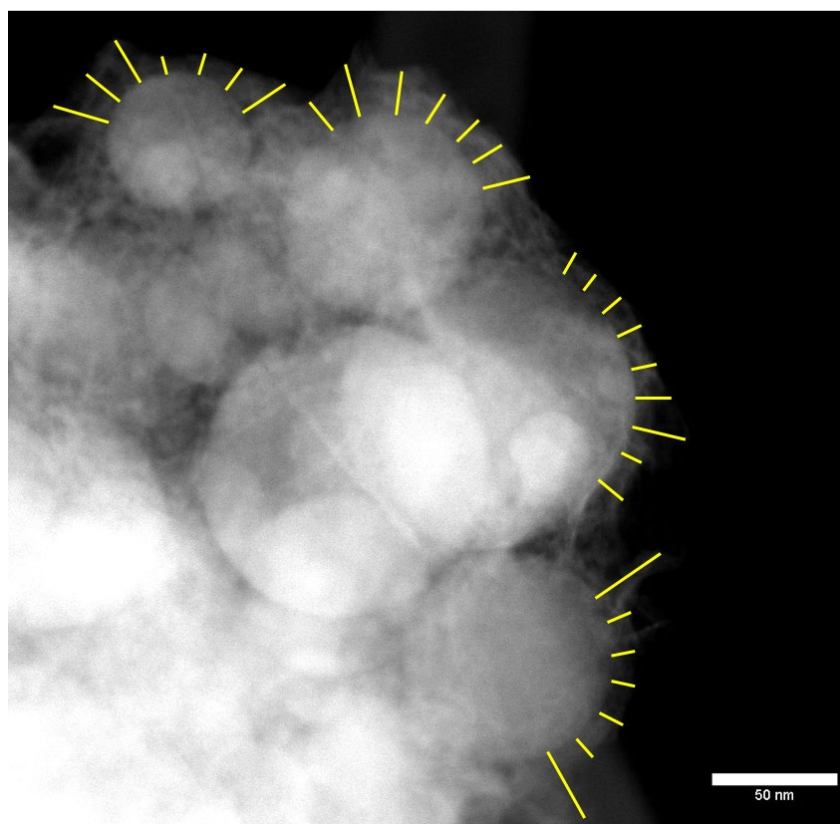


**Figure A.5:** Example of overcoat thickness measurements for irregularity factor determination (30  $\text{Al}_2\text{O}_3$  cycles on  $\text{Cu}/\text{Al}_2\text{O}_3$ )



## A.2 Tables

**Table A-1:** STEM-HAADF analysis of overcoated catalysts by 30 cycles with 0.5, 1 and 2 aluminum sec butoxide monolayers per cycle.

Sample	0.5 ML/injection	1 ML/injection	2 ML/injection
Number of measurements	345	269	213
Irregularity	80	27	66

**Table A-2:** ICP OES analysis of samples collected during furfural hydrogenation (after concentration).

Catalyst	Initial loading (%wt)	Mass catalyst (g)	Cu initial ( $\mu\text{mol}$ )	Cu leached ( $\mu\text{mol}$ )	%Cu leached
Cu/Al <sub>2</sub> O <sub>3</sub>	2.8	0.402	178	0.2	0.10
60 cycles Al <sub>2</sub> O <sub>3</sub> on Cu/Al <sub>2</sub> O <sub>3</sub>	2.1	0.478	156	0.2	0.15

**Table A-3:** Parameters for furfural hydrogenation control experiments.

Entry	Catalyst	Mass (g)	Gas	Conversion
1	Al <sub>2</sub> O <sub>3</sub>	0.3	H <sub>2</sub>	7 %
2	Al <sub>2</sub> O <sub>3</sub>	0.3	N <sub>2</sub>	7 %
3	Cu/Al <sub>2</sub> O <sub>3</sub>	0.3	N <sub>2</sub>	7 %

## A.3 Calculation of irregularity factor

We defined an irregularity factor to quantify the conformality of the coating from STEM images independently of the size of support, thickness of the layer and distribution of the layer thickness. For each particle, we delineated the zones that did not overlap with other particles and took 7 to 10 evenly spaced measurements of the overcoat thickness (see Fig. S5). The relative standard deviation of the measurements was calculated from a minimum of 7 measurements as follows:

$$\text{Rel. Std. deviation} = \frac{\text{std deviation of the thickness on the particle}}{\text{average thickness on the particle}} \times 100$$

**Equation A-1:** relative standard deviation

The irregularity factor was then calculated as the average of the standard deviation of between 25 and 35 particles:

$$\text{Irregularity factor} = \text{Average}(\text{Rel. Std. deviation for 25 – 35 particles})$$

**Equation A-2:** irregularity factor

## A.4 Control experiments

We performed several control experiments to quantify the extent of transfer hydrogenation of furfural by the alumina support. Three catalytic tests were carried out using the same conditions described in the experimental section, varying the catalysts and gas used as summarized in table S3. Those 3 tests gave the same result: a furfural conversion of 7 % (stable over 24 hours), with > 99 % selectivity to furfuryl alcohol. This demonstrated that the alumina support is able to perform transfer hydrogenation in the absence external hydrogen and in the absence of Cu. We presume that the source of hydrogen is the solvent (butanol) though no butanone was detected.

## A.5 Determination of mass transfer effects

Mass transfer effects were assessed using the Weisz-Prater criterion<sup>[279]</sup>:

$$\frac{r_{obs}(R_p)^2}{D_{TA}^e C_{AS}} < 1$$

### Equation A-3: Weisz-Prater criterion

Where:  $r_{obs}$  is the observed reaction rate

$R_p$  is the spherical particles radius

$D_{TA}^e$  is the effective transition diffusivity

$C_{AS}$  is the concentration at the surface of the catalyst particle

Bulk diffusivity of furfural into 1-butanol was calculated using Wilke-Chang equation<sup>[280]</sup> as followed:

$$D_{AB} = 7.4 \times 10^{-8} \frac{T (x M_B)^{1/2}}{\mu V_A^{0.6}}$$

### Equation A-4: Wilke-Chang equation for bulk diffusivity

The Wilke-Chang equation where

$D_{AB}$  is the bulk diffusivity (cm<sup>2</sup> s<sup>-1</sup>)

$T$  is the absolute temperature (403 K)

$x$  is the association parameter (taken as 1)

$M_B$  the molecular weight of the solvent (74 g/mol)

$\mu$  is the dynamic viscosity of the solvent (0.36 cP or mPas<sup>[281]</sup>)

$V_A$  is the molar volume at boiling point (90 cm<sup>3</sup> mol<sup>-1</sup>)

$V_A$  was calculated using the method presented by Sastri et al<sup>[282]</sup>.

This gives us a  $D_{AB}$  of  $4.8 \times 10^{-5} \text{ cm}^2 \text{ s}^{-1}$ .

Using the following equation from P. Harriot<sup>[280]</sup>, a size ratio of solute over pore diameter was calculated. This ratio can be used to calculate the internal diffusivity within the pores of the catalyst particles with respect to that of the bulk for liquid phase conditions.

$$\lambda = \frac{d_s}{d_p}$$

**Equation A-5** : solute over pore diameter size ratio

Where  $d_s$  is the diameter of the solute and  $d_p$  the diameter of the pore.  $d_s$  was estimated using Marvin sketch, where the longest distance between two atoms in the molecule was taken as the solute diameter (4.5 Å). The pore diameter (20 nm) was assessed using the BJH method using the isothermal adsorption of nitrogen.

$$\frac{D_{AB,pore}}{D_{AB}} = (1 - \lambda)^4 = 0.91$$

**Equation A-6** : relative coefficient of diffusivity

The variation of diffusivity being less than 10%,  $D_{AB}$  was used directly as  $D_{AB}$ . The diffusivity was converted into the effective diffusivity using the porosity ( $\epsilon$ ) and the tortuosity ( $\tau$ ) as follows:

$$D_{TA}^e = D_{AB}^e = \frac{\epsilon}{\tau} D_{AB}$$

**Equation A-7** : Effective diffusivity

According to Davis and Davis<sup>[279]</sup>, in absence of experimental data,  $\epsilon$  and  $\tau$  can be estimated respectively to 0.5 and 4.

This leads us to:  $D_{TA}^e = 6 \times 10^{-6} \text{ cm}^2 \cdot \text{s}^{-1}$ .

The observed rate of reaction was calculated from the first run of the overcoated catalyst, at 26 % conversion.

$$r_{obs} = - \frac{\Delta C_{furfural}}{\tau}$$

**Equation A-8** : observed rate of reaction

Where  $\tau$  is the residence time calculated as the ratio of the bed volume over the flow.

We obtained  $r_{obs} = 1 \times 10^{-7} \text{ mol L}^{-1} \text{ s}^{-1}$

The surface concentration,  $C_{AS}$ , was calculated using the mass transfer coefficient ( $k_c$ ) as followed:

$$r_{obs}^{surf} = k_c (C_{AB} - C_{AS})$$

**Equation A-9** : surface observed rate of reaction

This  $r_{obs}^{surf}$  is expressed in  $\text{mol m}^{-2} \text{s}^{-1}$  unlike  $r_{obs}$ , which is expressed in  $\text{mol L}^{-1} \text{s}^{-1}$ .

$k_c$  was calculated using the following correlation involving the Sherwood, Schmidt and Reynolds numbers:  $Sh = 2 + 0.6Re^{1/2}Sc^{1/3}$

We found a  $C_{AS} = 4.45 \times 10^{-1} \text{ mol L}^{-1}$

The particle radius was estimated to 65 nm based on imaging.

With all these numerical values, a value for the Weisz-Prater criterion of 0.025 is found which is far below one. This confirms that we are working in kinetic regime.

## B Supplementary information of chapter 3

### B.1 Figures

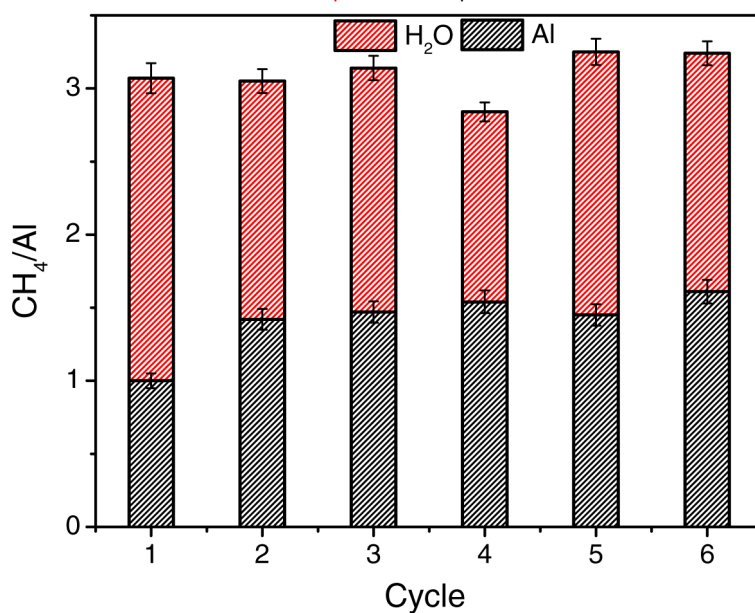


**Figure B.1:** Total methane released at each cycle after both aluminum and water injections. The results (which correspond to those shown in Figure 2e) show that the overall  $\text{CH}_4/\text{Al}$  on each cycle is close to 3, indicating that the mass balance is closed. A 5% error was measured when repeating the experiments.

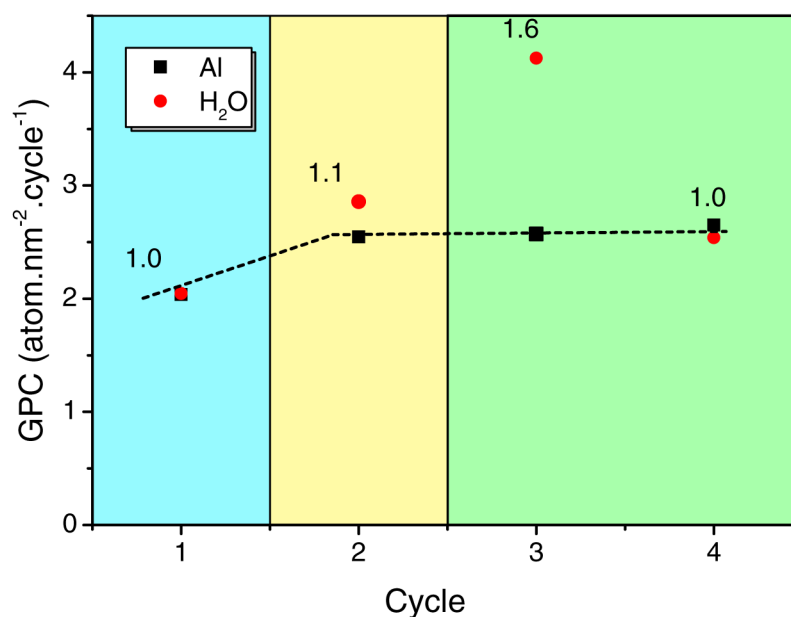


**Figure B.2:** Growth per cycle (GPC) measured on high surface area silica ( $>350\text{m}^2/\text{g}$ ) showing a short cluster growth phase, a cluster merging phase and a film growth phase. As discussed in the main text, a low water-to-aluminum ratio is observed when clusters meet and alternating additions of higher ( $\text{H}_2\text{O}$  to Al ratios  $>1$ ) and lower ( $\text{H}_2\text{O}$  to Al ratios  $<1$ ) water-to-aluminum ratios are observed during film growth.

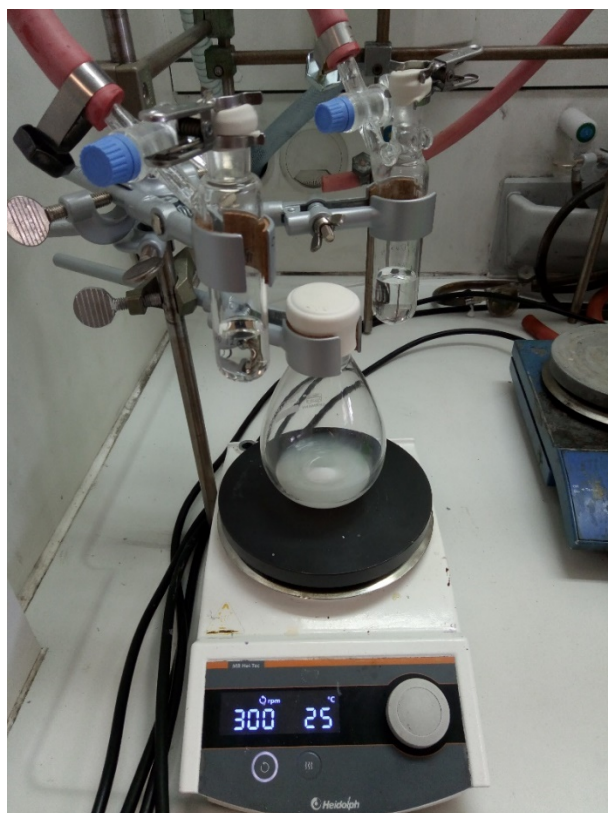


**Figure B.3:** Picture of the setup for surface titration and atomic layer deposition, which highlights the simplicity of the procedure and equipment along with its limited footprint. The Schlenk tube on the left-hand side contained the precursor solution while the tube on the right-hand side contained the

counter reactant solution. The septum-caped round bottom flask contained the dispersed catalyst in the solvent of interest.

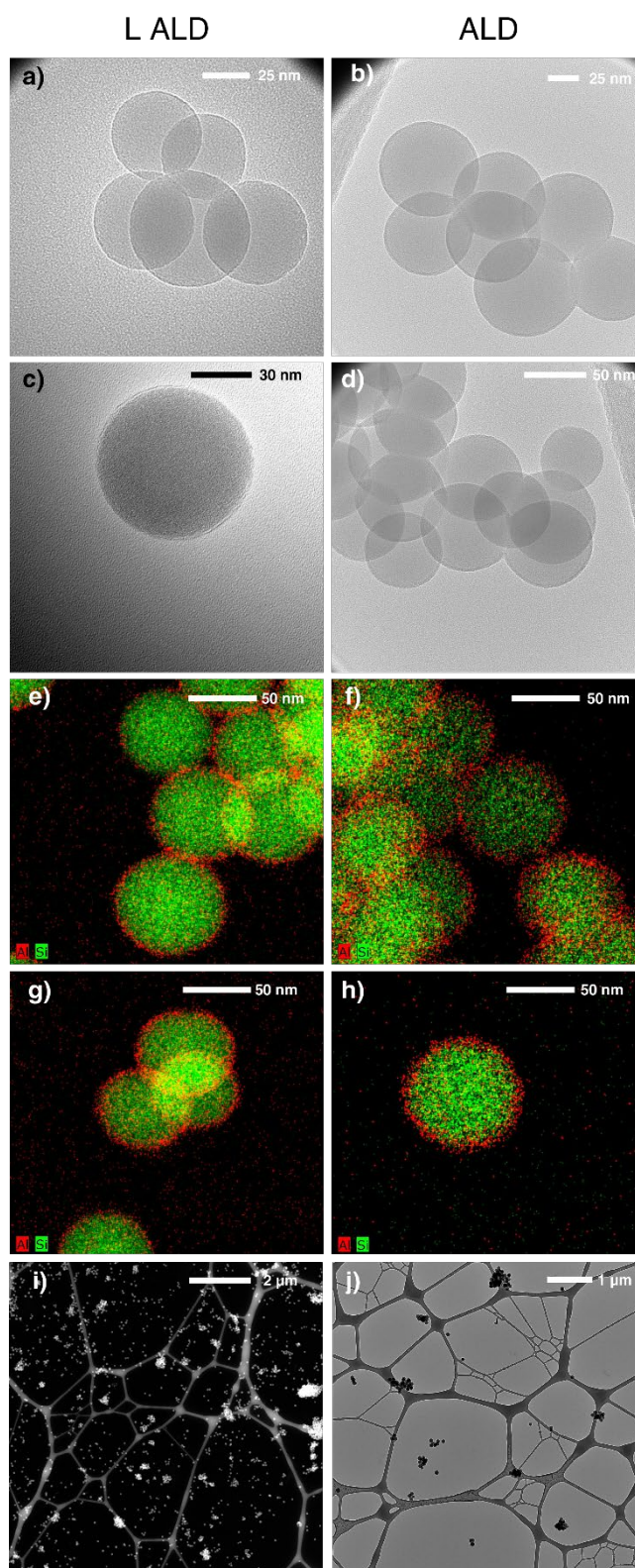


**Figure B.4:** Comparison between alumina coatings on silica nanospheres using our Liquid phase ALD method and gas phase ALD using a fluidized bed reactor. In both cases, the silica spheres were coated with TMA/water 10 cycles. a-d) TEM bright field images showing that both coating are thin and conformal. e-h) STEM EDX elemental mapping highlighting the presence of alumina on silica

surface, without free standing alumina nor uncoated particles. j and j) STEM-HAADF and TEM bright field images at low magnification, showing that the particles are well dispersed on the grid and not glued all together by the coating.

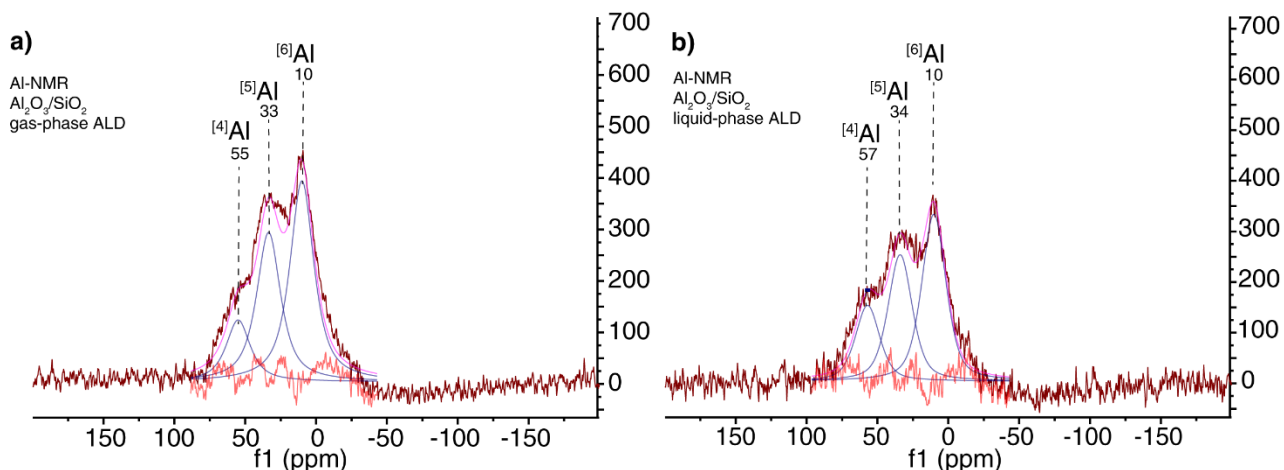


**Figure B.5:** Solid state nuclear magnetic resonance spectroscopy of: a) 10-cycles of alumina deposited on silica spheres by gas-phase ALD and b) 10-cycles of alumina deposited on silica spheres by the liquid-phase ALD presented in this work. Both spectra are very similar and feature an important peak corresponding to penta-coordinated aluminum, which indicates an amorphous phase.<sup>[283]</sup>

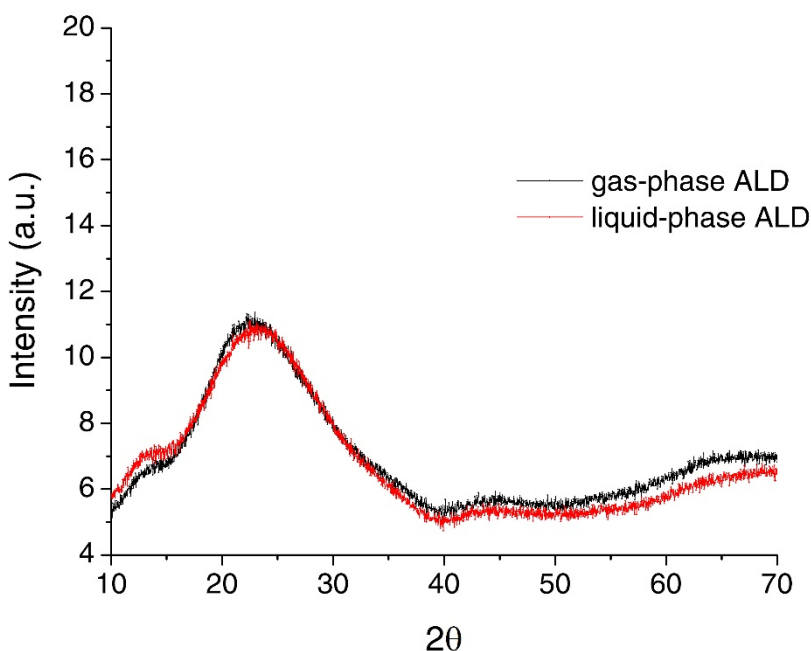


**Figure B.6:** Powder X-ray diffraction pattern of 10-cycles of alumina deposited on silica spheres by gas-phase and liquid-phase ALD. Both are identical and only display a large peak around  $22^\circ$ , which corresponds to the silica core.<sup>[284]</sup>



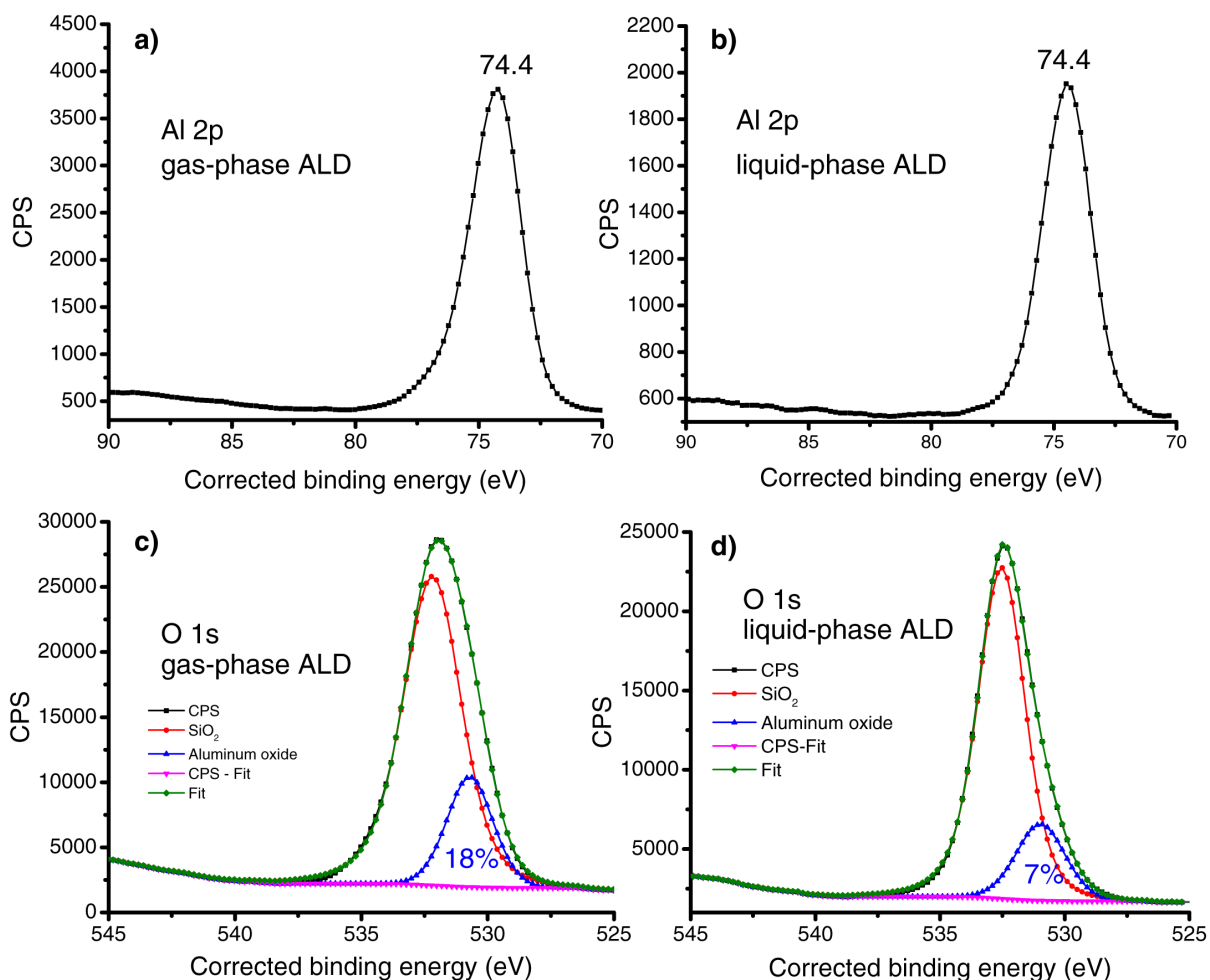


**Figure B.7:** X-ray photoelectron spectroscopy (XPS) of 10-cycles of alumina deposited on silica spheres. a) Alumina peak shown for samples prepared by gas-phase ALD, b) Alumina peak shown for samples prepared by liquid-phase ALD. c) Oxygen peak shown for samples prepared by gas-phase ALD. d) Oxygen peak shown for samples prepared by liquid-phase ALD. The Peaks of aluminum have the same energy for the samples resulting from both liquid and gas phase preparation methods, indicating that the phase is the alumina same in both cases. Oxygen peaks can be deconvoluted into the alumina and silica contributions. The oxygen from the alumina phase has the same energy in both cases, confirming that the structure of the overcoat is the same for both preparation method. The higher total contribution of the oxygen from the silica in the case of preparation by liquid phase ALD is indicative of a thinner layer, which is consistent with what was observed by electron microscopy.<sup>[285,286]</sup>

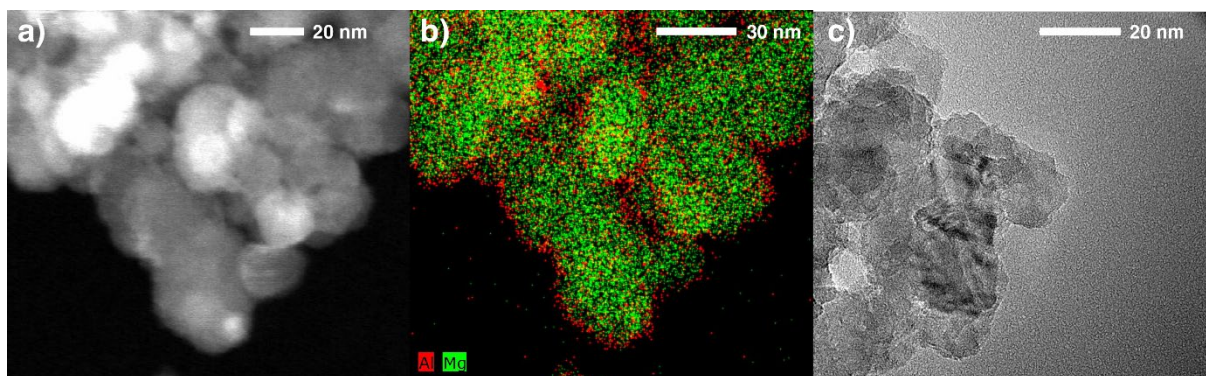


**Figure B.8:** Transmission electron microscopy images of commercial magnesium oxide coated with 10 TMA/water cycles in liquid phase. a) and d) are STEM HAADF images showing no traces of free alumina. b) and e) are EDX pictures showing that the alumina coating systematically follows the surface of the support. c) and f) are bright field pictures showing that alumina follows to a degree where its visualization is difficult.

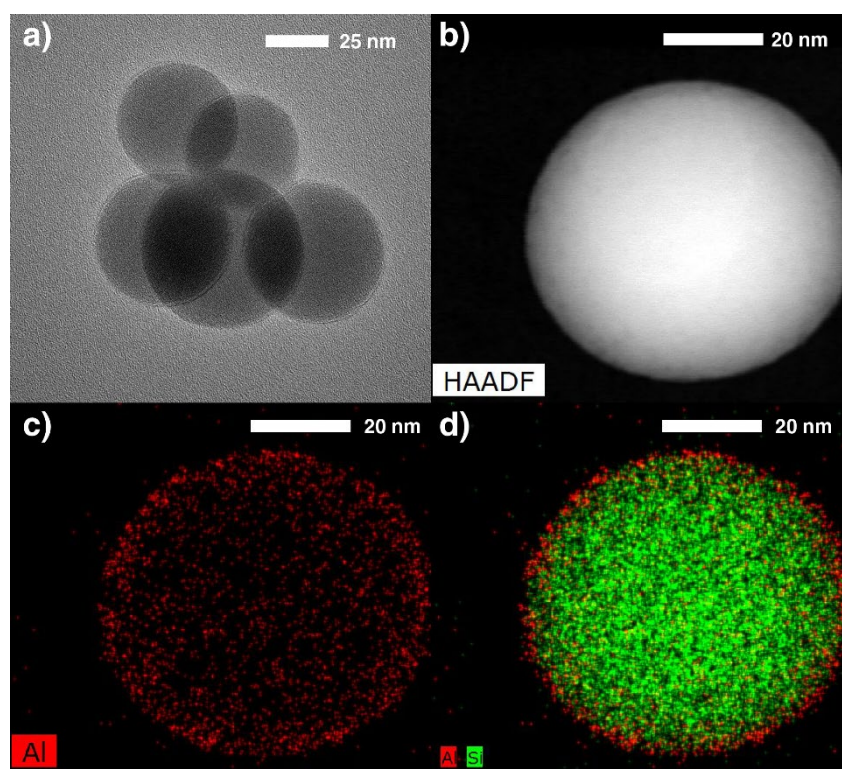


**Figure B.9:** Transmission electron microscopy images of silica nanospheres coated with 10 TMA/water cycles in liquid phase using a reaction time of only 10 min between injections. a) Bright field image b) HAADF image c) and d) are the elemental mapping corresponding to the HAADF image.

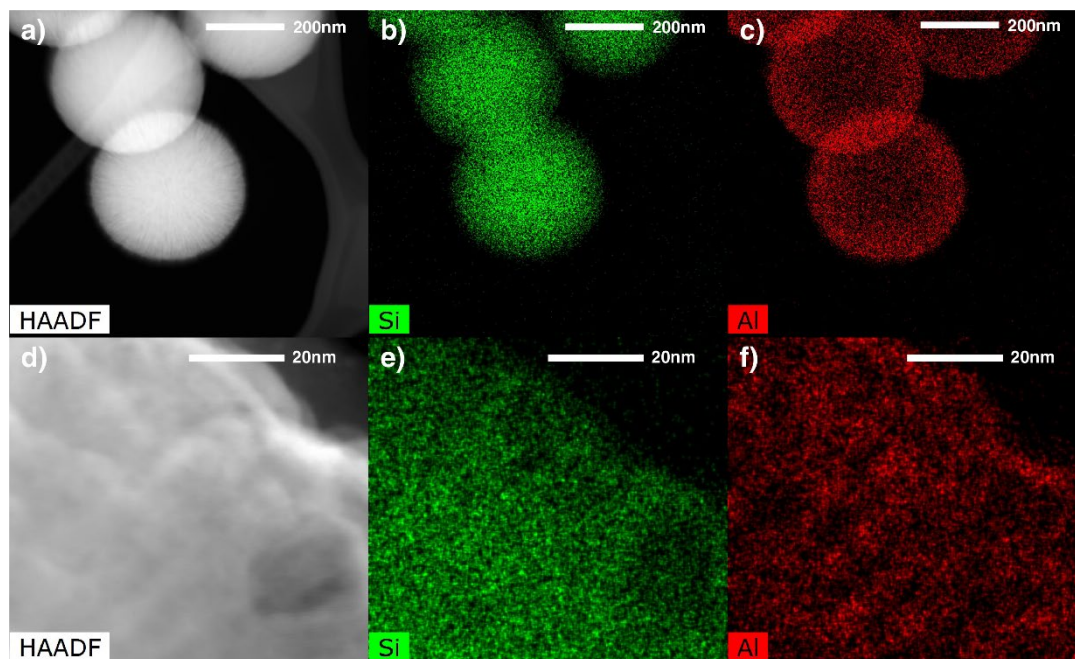


**Figure B.10:** Scanning transmission electron microscopy images of high surface area silica KCC (“hairy” spherical porous particles), coated with 10 TMA/water cycles in liquid phase. a-c) Imaging of the entire particle showing that aluminum is detected inside the porous ring of the material and not just on its outer surface. d-f) A close-up of the outer ring showing “stripes” of aluminum following the silica pores.

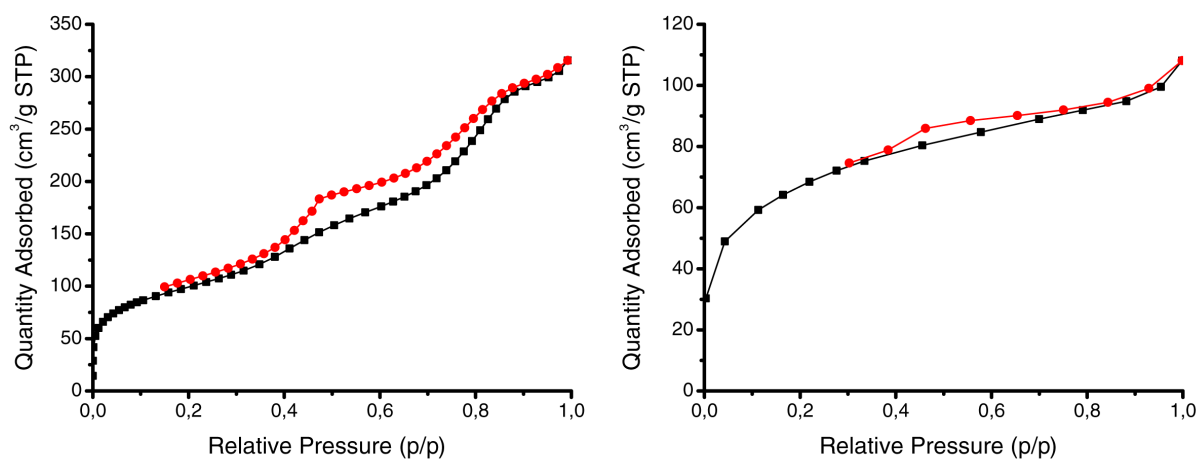


**Figure B.11:** N<sub>2</sub> adsorption isotherm at 77 K of a) bare high surface area silica b) the same material coated with 10 cycles of stoichiometric TMA/H<sub>2</sub>O.

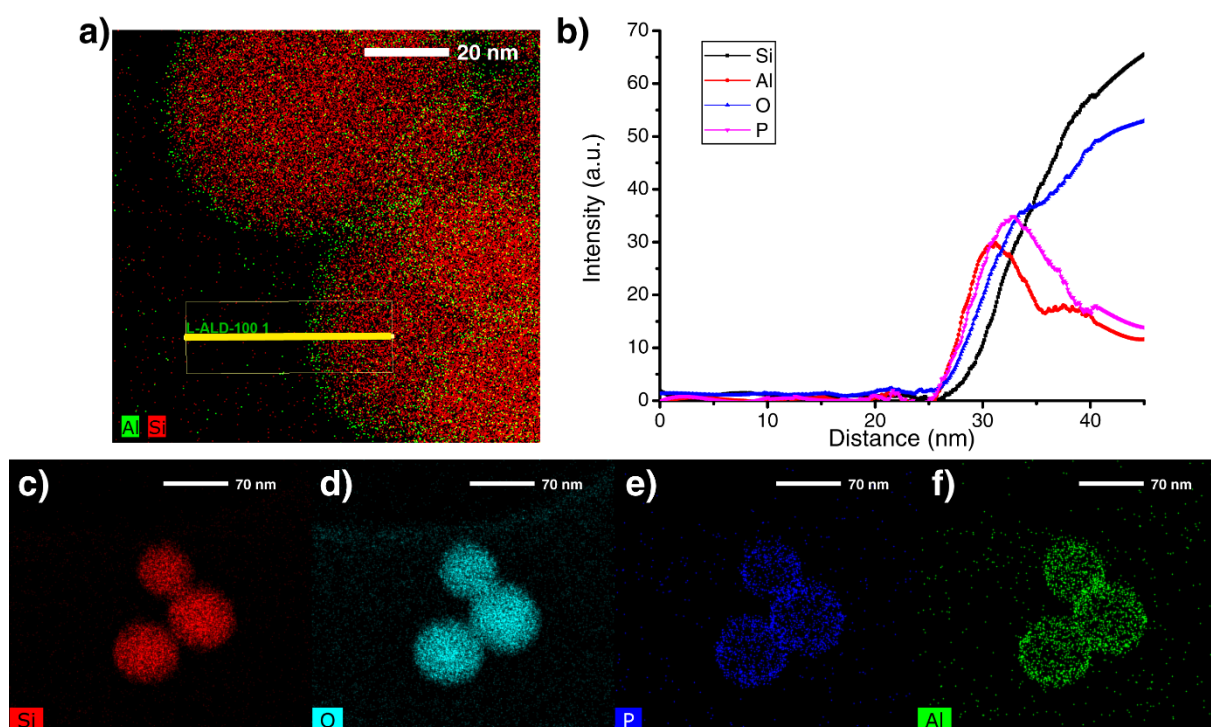


**Figure B.12:** Additional transmission electron microscopy analysis of silica nanospheres coated with 5 cycles of TMA/ $\text{H}_3\text{PO}_4$  in the liquid phase. a) Elemental mapping by EDX. b) Line scan corresponding the EDX picture shown in a), demonstrating that an overcoat contains Al, P and O while the bulk of the sphere is mainly composed of Si and O. c-f) Elemental mapping showing the distribution of silica and aluminum phosphate on the nanospheres, which confirms the highly conformal nature of the overcoat.

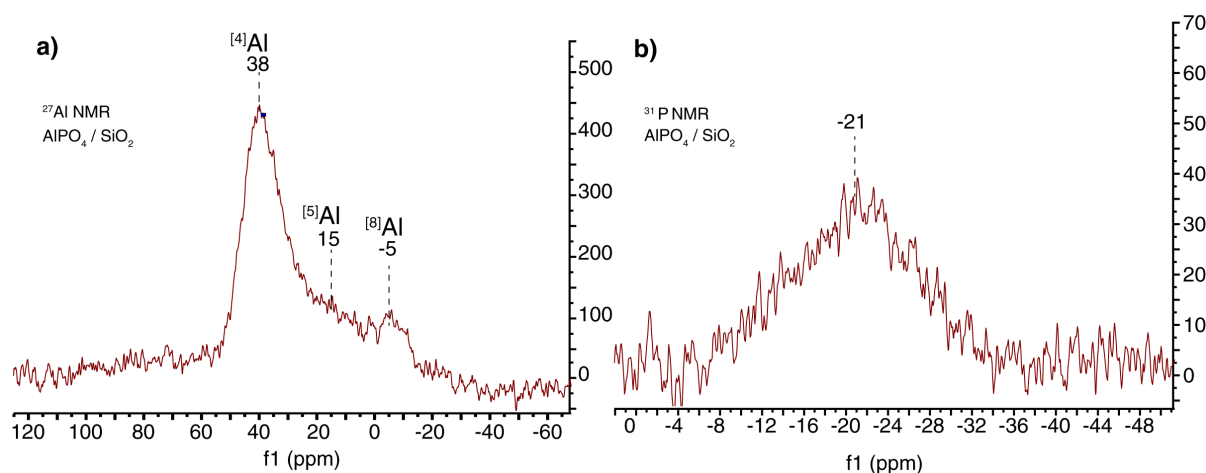


**Figure B.13:** aluminum a) and phosphorus b) solid state NMR spectra of silica coated with 10-cycles of AlPO using on trimethyl aluminum and phosphoric acid injections. The aluminum peaks match with what expected for an amorphous aluminum phosphate phase. The phosphorus chemical shift also matched what was expected for an aluminum phosphate phase.<sup>[287,288]</sup>



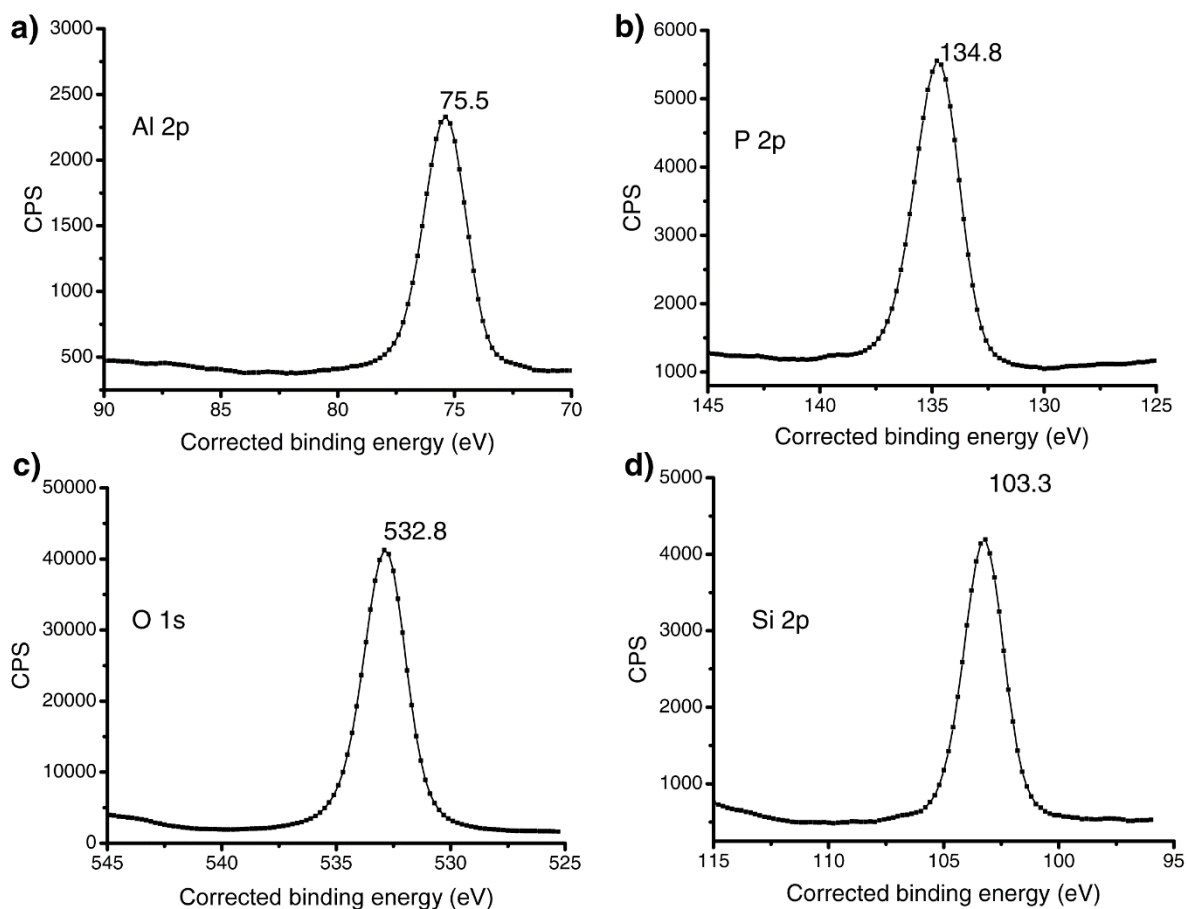


**Figure B.14:** XPS spectra of aluminum phosphate deposited onto silica spheres by 5 cycles of liquid phase ALD using injections of trimethyl aluminum and phosphoric acid. a) aluminum speak, b) phosphorous peak, c) oxygen peak and d) Si peak. The aluminum energy is relatively high, which is consistent with a phosphate or phosphonate phase.<sup>[288,289]</sup> The phosphorus peak energy matches that of a phosphate phase. No separation between the oxygen peaks of the phosphate and silica phases can be done because they are too close in energy. The silicon peak is consistent with a typical silica phase.<sup>[289][285]</sup>

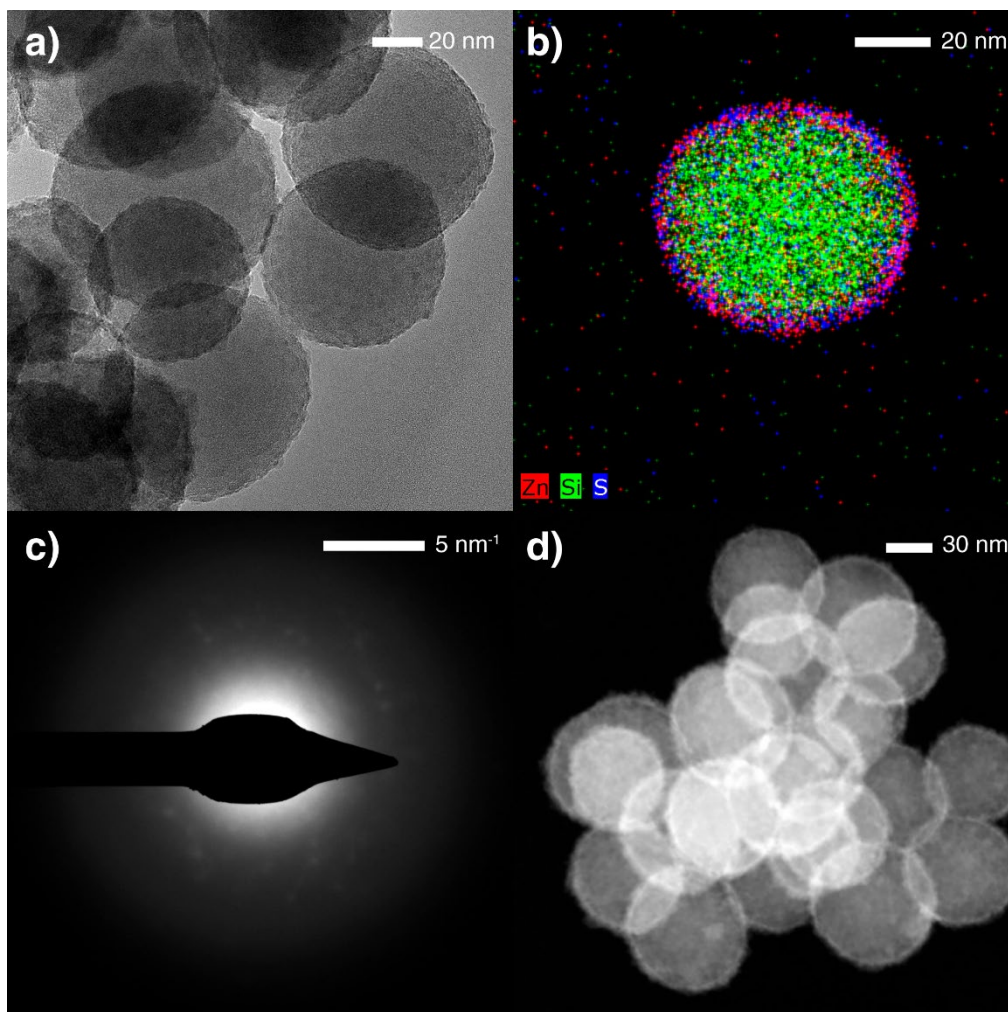


**Figure B.15:** TEM images of ZnS deposited on silica spheres by 5 cycles of liquid-phase ALD. a) TEM bright field image, b) EDX map, c) Electron diffraction pattern and d) STEM-HAADF image. The bright field picture reveals how homogeneously dispersed the crystallites are on the surface. The EDX mapping shows a continuous layer of ZnS consistent with a shell rather than isolated crystallites. The electron diffraction pattern shows clear diffraction spots, confirming that ZnS is at least partially crystalline. The STEM-HAADF imaging confirms that the ZnS layer is conformal and perfectly follows the surface of the substrate.

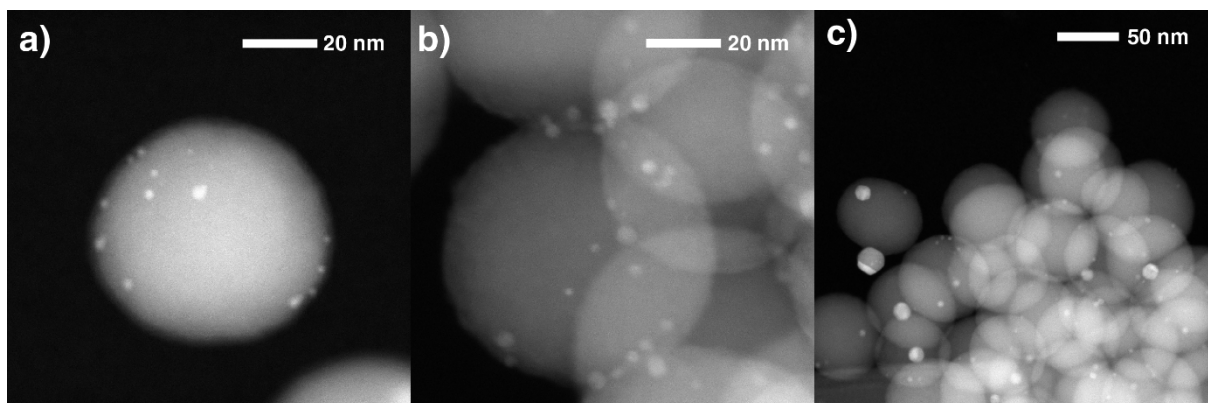


**Figure B.16:** STEM-HAADF images of a) Palladium supported on silica nanospheres b) the same catalyst with an alumina overcoat (after 20 cycles of TMA/H<sub>2</sub>O deposition in liquid phase) after thermal treatment (600°C under 10%H<sub>2</sub> in Ar for 1 hour, 20 °C/min), and c) the same catalyst without an overcoat after thermal treatment showing several large (>10 nm) particles.

## B.2 Details on material preparation based on previously published methods

### Silica spheres

The procedure was based on Stöber method.<sup>[246]</sup> Typically, 200mL of water and 100mL of ammonia were added to 4400 mL of ethanol. Then TEOS was rapidly added and the mixture was stirred overnight, neutralized with nitric acid, centrifuged, dried, and finally calcined at 500°C overnight to desorb any leftover nitrogen. All supports were humidified using a water spray prior to drying at the desired temperature (150 - 500 °C depending on the target hydroxyl density) and stored in a glove-box before coating. The hydroxyl density was quantified by measuring the methane released during a reaction between commercial methyl magnesium bromide and the substrate.

### Palladium model catalyst

The palladium catalyst was prepared following a published method with a loading of 0.5 wt% Pd.<sup>[145]</sup> Briefly, Palladium nitrate was dissolved into a citric acid solution and was added dropwise to disperse catalyst. After 2 hours of stirring at room temperature, the liquid was evaporated by rotavapor. The impregnation was followed by a calcination at 400°C (5 hours, 3 K/min) and then by a reduction step at 300°C (1 hour, 2 K/min).

## B.3 Experimental considerations for TMA titrations

When repeating the TMA titration for different silica quantities (**Figure B.17a**), one can see that points before surface saturation all fall exactly on the same line. After saturation, the points are still aligned but their slope can change from one experiment to another. Considering that the two experiments were performed using a different mass of silica, we concluded that the origin of the slope after saturation is likely linked to the solvent to substrate ratio rather than a surface reaction. TMA

is known to have a high vapor pressure, which is one of the reasons for its use in conventional gas phase ALD. Therefore, the post saturation slope likely comes from the sampling of gaseous TMA, which then decomposed in the injector of the GC to form additional methane. Slope variations post saturation from one experiment to another are thus likely influenced by the mass of catalyst but also temperature in the fumehood.

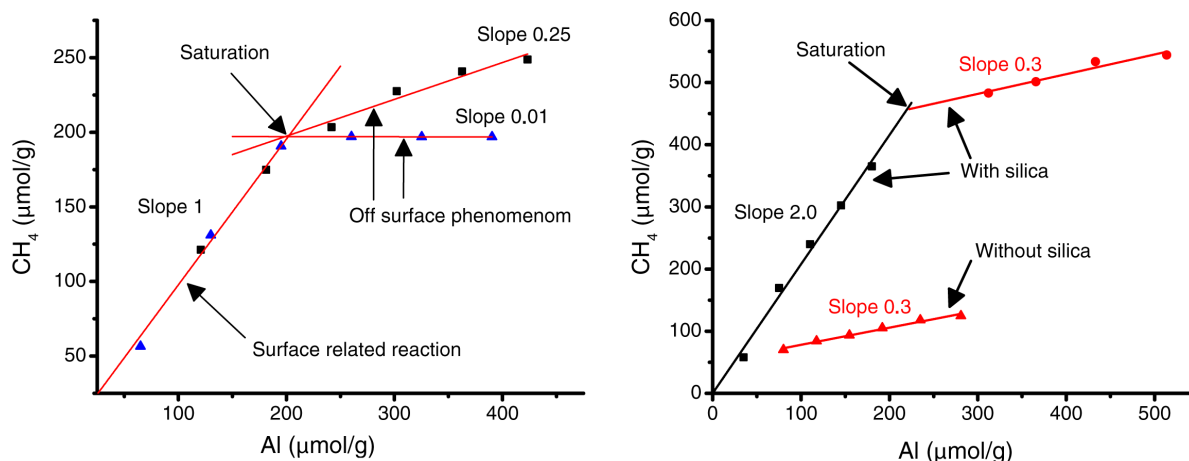


**Figure B.17:** a) Study of the post saturation slope by repeating TMA surface titration on 1.3g (black squares) and 2.3g (blue triangles) of silica. b) TMA titration with and without silica showing that the slope after saturation is independent of the presence of a support.

When fresh silica is used, a slope of 2 was observed, indicating two reactions per aluminum with the surface (**Figure B.17b**). After saturation, a smaller slope is observed, attributed to the injection of TMA in the vapor phase. When silica is absent, the same post saturation slope of 0.3 is present, which confirmed that this phenomenon was not due to interaction with silica but was likely due to TMA present in the gas phase.

To confirm that this slope could indeed be due to the vapor pressure of TMA, an estimate of this quantity can be performed. Assuming injections of 50  $\mu\text{mol}$  of TMA for 1g of catalyst, we can estimate the quantity of TMA in the gas phase.

The TMA vapor pressure can be calculated using the Antoine Equation:

$$\log(P) = A - \left(\frac{B}{t + C}\right)$$

**Equation B-1:** Antoine Equation

With  $A = 4.68$ ,  $B = 1724.231$  and  $C = -31.40$  given by J.P. McCullough et al.<sup>[290]</sup>

Leading to  $P = 16.3$  Pa.

Using the ideal gas law, we estimated that there would be about 2  $\mu\text{mol}$  of TMA in the vapor phase, hence giving a slope of  $3 \cdot (2/50) = 0.12$  methane released per TMA added, which is within the same order of magnitude as what we observed.



## B.4 Estimation of mass transfer limitations

We assume that the rate of reaction is much faster than mass transfer, because we know that TMA is extremely fast (< seconds) and a diffusion-limited system represents the worst-case scenario. We also treated the reaction of TMA with surface hydroxyl groups as an irreversible surface reaction (see reaction scheme).

$AlR_3 + OH_{surface} \rightarrow Al(R)_2O_{surface} + CH_4$  diffusion coefficient was estimated using the Stokes-Einstein equation:

$$D_{TMA} = \frac{k_B T}{6\pi r_{TMA} \mu_{DBE}} \quad (1)$$

**Equation B-2:** Stokes-Einstein equation

Where:

$k_B$  is the Boltzmann constant ( $1.38 \cdot 10^{-23} \text{ m}^2 \cdot \text{kg} \cdot \text{s}^{-2} \cdot \text{K}^{-1}$ )

$T$  is the temperature (298 K)

$\mu_B$  is the dynamic viscosity of DBE ( $0.000637 \text{ kg} \cdot \text{m}^{-1} \cdot \text{s}^{-1}$ )<sup>[291]</sup>

$r$  the equivalent radius of TMA, calculated from its molar volume ( $3.36 \cdot 10^{-10} \text{ m}$ )

This results in a diffusivity estimate of:  $D_{TMA} = 1.02 \cdot 10^{-5} \text{ cm}^2 \cdot \text{s}^{-1}$ .

Because the spheres are largely non-porous, we consider only external mass transfer. The external mass transfer coefficient ( $k_c$ ) can be estimated for spherical particles using an empirical correlation of the Schmidt (Sc), Sherwood (Sh) and Reynolds (Re) numbers<sup>[279]</sup>:

$$Sc = \frac{\mu}{\rho D_{TMA}} \quad (2)$$

$$Sh = \frac{k_c 2R_p}{D_{TMA}} \quad (3)$$

$$Re = \frac{\rho u (2R_p)}{\mu} \quad (4)$$

$$Sh = 2 + 0.6 Re^{1/2} Sc^{1/3} \quad (5)$$

$$k_c = \frac{Sh D_{TMA}}{2R_p} \quad (6)$$

**Equation B-3:** (2) Schmidt, (3) Sherwood and (4) Reynolds numbers

Where:

$\rho$  is the density of DBE (767 kg.m<sup>-3</sup>)<sup>[292]</sup>

$R_p$  is the radius of silica spheres (100 nm)

$u$  the fluid velocity, estimated based on the stirring speed (350 rpm, 0.458 m.s<sup>-1</sup>)

Using these equations, we estimated the external mass transfer coefficient as:  $k_c = 3.38.10^{-2}$  m.s<sup>-1</sup>

In the case of a process that is entirely controlled by external mass transfer, the reaction can be set equal to the external mass transfer:

$$-\frac{V_{reactor}}{surface\ area_{substrate}} \frac{d[TMA]}{dt} = k_c [TMA] \quad (7)$$

By rearranging and integrating:

$$\frac{\ln([TMA]/([TMA]_0))}{k_c \frac{surface\ area_{substrate}}{V_{reactor}}} = t \quad (8)$$

Considering a  $V_{reactor} = 20$  mL, 2 g of SiO<sub>2</sub> to be coated and a hydroxyl density of 400  $\mu$ mol/g (4.8 OH/nm<sup>2</sup>), we can calculate that the time needed to reach 99.99% conversion is  $5.5.10^{-5}$  s.

## B.5 Solvent and ligand effects during TMA titrations

We further investigated the effects of different solvent use on the deposition of TMA. Specifically, three different solvents were tested: dibutyl ether, dioxane and decane in dilute (20mL solvent, 1-2g of catalyst) and concentrated (at the incipient wetness point) conditions. With dibutyl ether and decane dilute or concentrated condition led to similar results. With decane, the slope was twice as small and the total quantity of aluminum deposited was twice as high compared to dibutyl ether, which is consistent with the results shown below (**Figure B.18**). As discussed in the main text, this phenomenon is likely due to TMA dimerization in alkanes.<sup>[293,294]</sup>

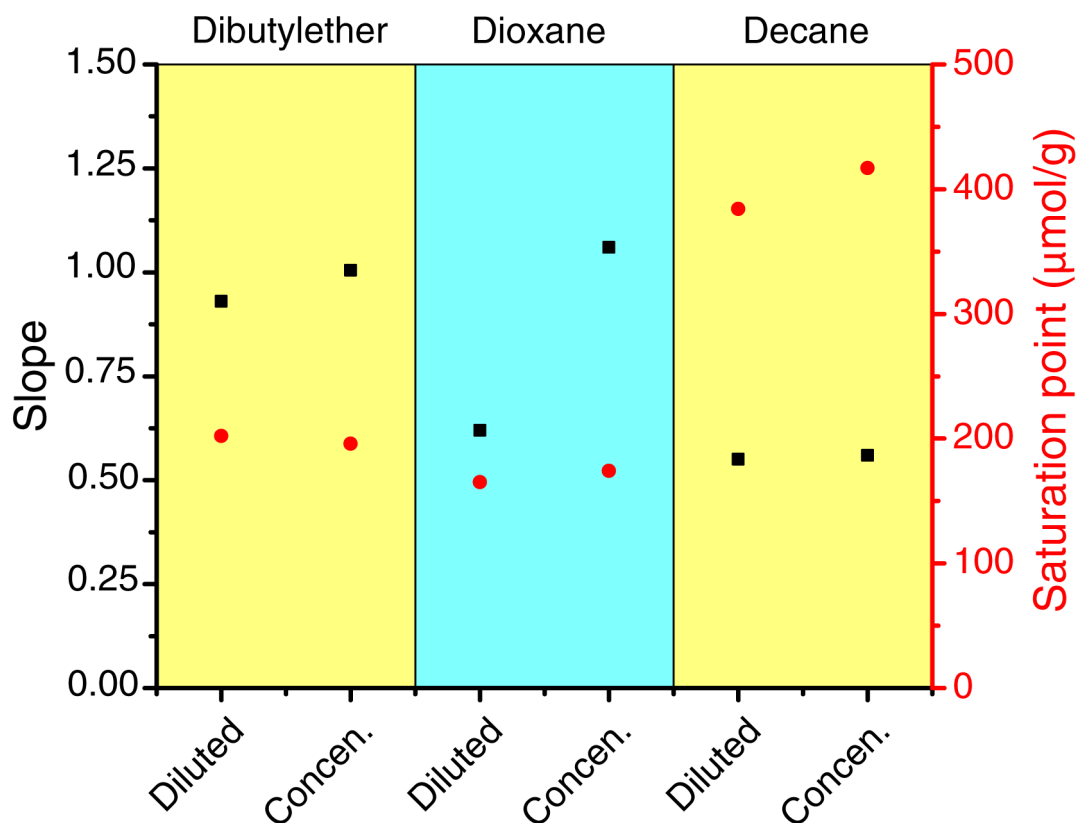


**Figure B.18:** Study of the solvent effect on the saturation point (equivalence at full coverage) and methane released during surface titration of silica with TMA (the slope represents the number of  $\text{CH}_4$  molecules release per atom of Al added).

We also tested the effects of using different ligands in alkyl aluminums during their deposition (Figure S.13). The difference in density between cases 1) and 2), where octyl aluminum was deposited in dibutyl ether and decane, respectively, was attributed to the complexation of the ethereal solvent to the aluminum center, increasing its Van der Waals size, and the corresponding space between two aluminum atoms. Using TMA systematically led to the highest surface density of deposited aluminum, which was likely caused by the lower steric hindrance associated with the smaller ligands. Finally, the use of decane as a solvent when depositing TMA, almost exactly doubled the quantity of aluminum on the surface compared to dibutyl ether. Once again, this doubling can be attributed to the formation of TMA dimers in alkanes while TMA is monomeric in heteroatom containing solvents.<sup>[293,295]</sup> Therefore, the same amount of aluminum is likely directly attached to the surface, but the surface bound aluminum is linked to a second aluminum within this dimer structure.

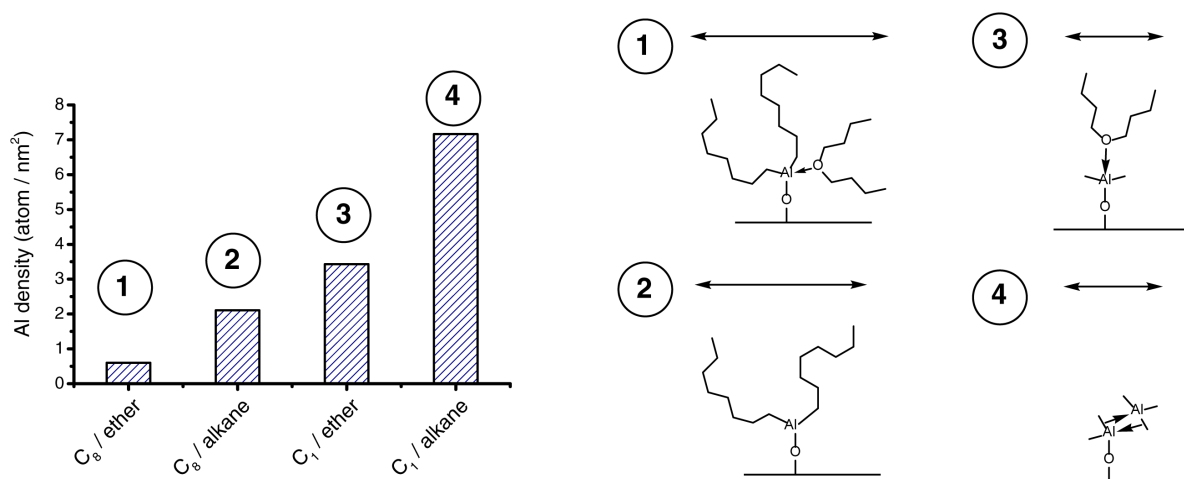


**Figure B.19:** Density of alkyl aluminum deposition on commercial alumina spheres (hydroxyl density: 8 OH/nm<sup>2</sup>) depending on the ligand size and solvent that was used. In case 1), the deposition was performed using tri octyl aluminum (C<sub>8</sub>) in dibutyl ether. In case 2), the same precursor was used but the solvent was decane. In case 3) trimethyl aluminum (C<sub>1</sub>) was used in dibutyl ether and finally in 4) TMA was used in decane.

In addition to the difference of size, the octyl ligand will be released as octane, which will remain in the liquid phase, while the methyl will be released as methane, which is gaseous. This difference changes the data analysis but results in an otherwise similar approach. When tri octyl aluminum was used for coating, small liquid phase samples (0.2mL) were taken from the reactor so as to minimally affect the reactor volume. The samples were filtered and hydrated with deionized water to hydrolyze the excess aluminum in solution (after the saturation point) and injected into a liquid GC-FID. The hydrolysis prior to injection was performed to protect the injector of the GC as any remaining reactant would hydrolyze in the injection system regardless. Considering that, contrary to when TMA was used where the any unreacted TMA remained largely in the unsampled liquid phase, in this case, the excess of trioctyl aluminum was hydrolyzed and injected along with the already released octane ligands. This leads to all ligands being systematically hydrolyzed and to a slope of 3 when plotting released octane per added aluminum after the full coverage is reached (figure S.20) (compared to a slope close to 0 when TMA was used). The point of full coverage is determined when the slope shifts from below 3 to 3 (**Figure B.20**).

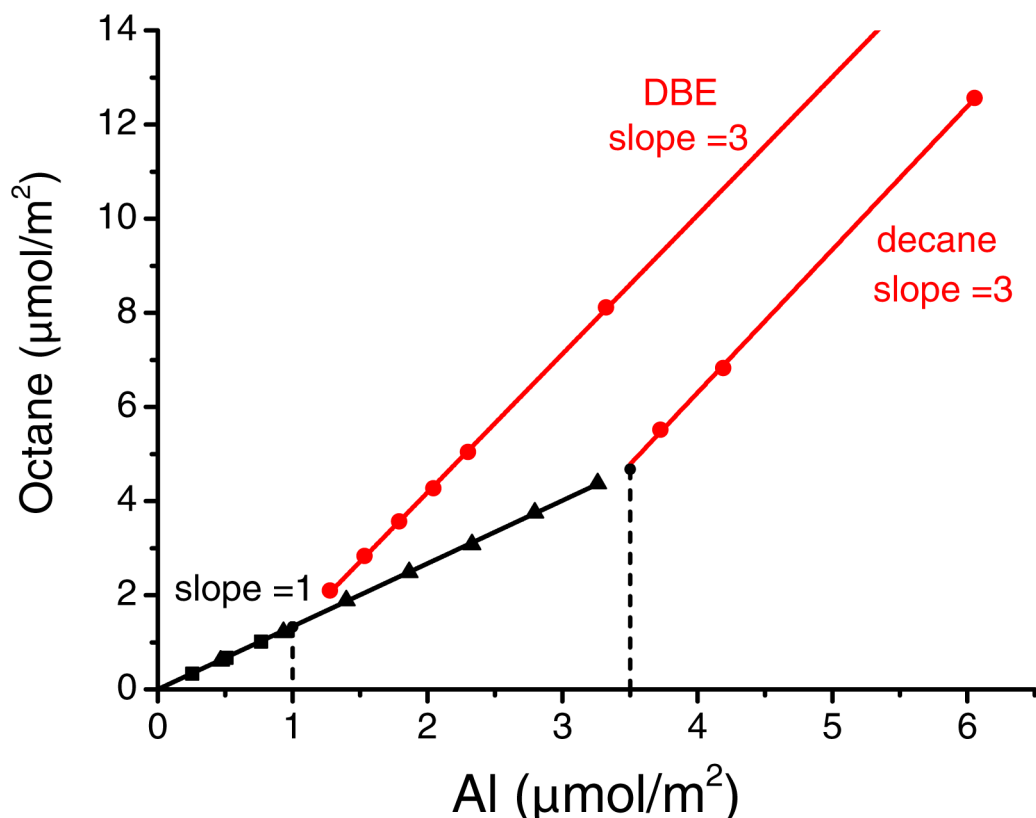


**Figure B.20:** Titration curve of alumina spheres by tri octyl aluminum in dibutyl ether and decane. Contrary to TMA, the released ligand is in the liquid-phase, as is the excess of precursor. Therefore, after full coverage, octane from the excess of precursor is detected, leading to a slope of 3 since each precursor is hydrolyzed and releases all 3 ligands.

## B.6 S4 Experimental considerations about water titrations

Water is not sufficiently soluble in dibutyl ether to prepare a dosing solution. Therefore, a small amount of water (typically 0.2mL) is diluted in 40 mL of dioxane and this solution is used for injections. While determining the stoichiometry of water needed to hydrolyze an aluminum covered surface is straightforward, the titration slope (representing CH<sub>4</sub> released per water injected) was significantly influenced by the solvent. As shown in Figure S.12 the use of dioxane as a solvent led to inconsistencies in this slope. The stoichiometry of the equivalent point was unaffected but only about half of the methane that was expected was detected whenever dioxane was present.

On all water titration curves where dioxane was present, the observed slope was 1 and 0.5 when 2 and 1 was expected. As far as we know, no mechanism in literature would justify a 0.5 ratio CH<sub>4</sub>/TMA or CH<sub>4</sub>/water during the surface reaction. Kinetic competition with alkyl transfer or surface rehydroxylation seems very unlikely considering the low temperature and the fact that it did not happen in dibutyl ether (where Al is in a similar electronic environment). Moreover, this effect is observed on all cycles, even after the formation of a continuous film that completely covered the silica. As a further control to show that this was purely a solvent effect, we performed an experiment where water in dioxane was injected directly into a solution of TMA in dibutyl ether in order to perform a simple solution phase hydrolysis (Figure S.14). The equivalence point was obtained

after 1.8 molecules of water were injected per molecule of TMA as expected but only 1 molecule of methane was released per molecule of water injected even though, in such an environment, water will always bridge two aluminum atoms, as confirmed by the equivalent point.

In summary, less methane is detected when even a small amount of dioxane is present, which is not fully understood. Because this phenomenon happened even when the control experiment was performed, a multiplication factor of 2 was applied to the methane measured during the water titration when dioxane was present. This numerical adjustment has no effect on the saturation point (on which all our mechanistic determination are based) since it concerns only the total methane released and not the quantity of water added.

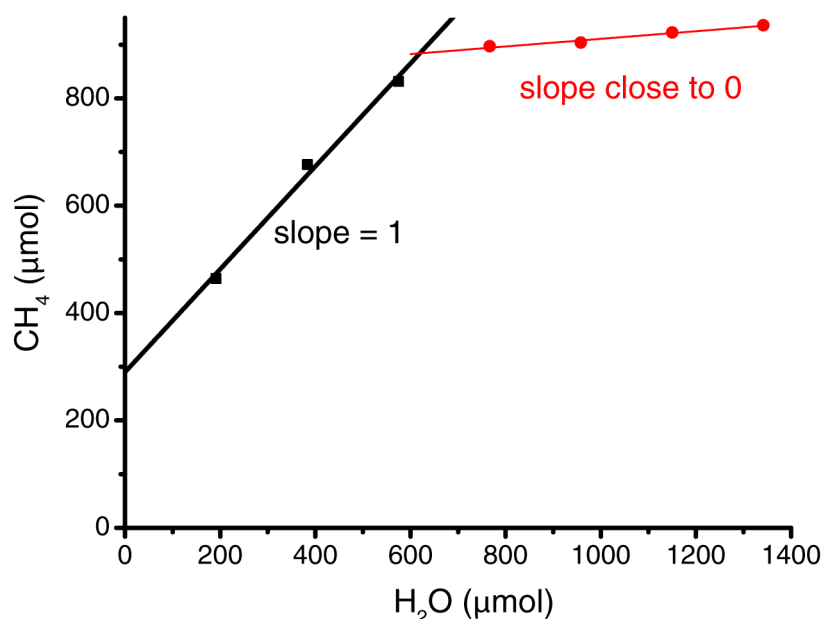


**Figure B.21:** Hydrolysis of TMA solution in dibutyl ether by a solution of water in dioxane.

Another way to observe this systematic effect was to deposit a monolayer of TMA onto silica and to compare the methane release when pure water or water diluted in dioxane was added (**Figure B.22**).

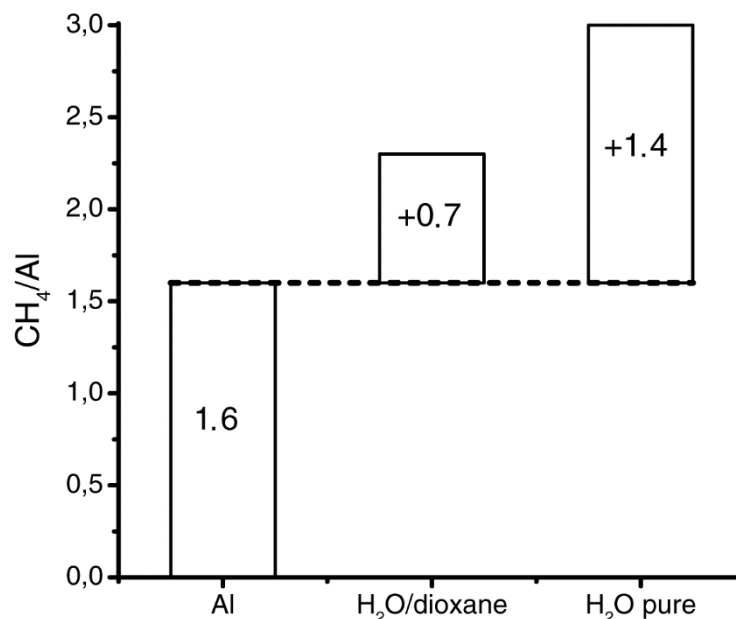


**Figure B.22:** Methane balance on the first cycle of deposition of trimethyl aluminum on silica powder, hydrolyzed by water solution in dioxane or pure water.

During the first half cycle when TMA was added, 1.6 methane per aluminum were released, indicating the presence of both bi and mono grafted aluminum. After hydrolysis by pure water, 1.4 equivalents of methane were released full recovery of methane was achieved, indicating that no, or very limited, alkyl transfer happened from the aluminums atoms to the silicon ones.<sup>[296]</sup> When the water was added at same time as dioxane, only half of the methane was detected, demonstrating how systematic this effect is.

A possible explanation for this phenomenon is that the dioxane reacts with TMA at room temperature in the presence of water and produces a product that remains soluble. To verify this, we analyzed liquid samples of hydrolyzed TMA in DBE and TMA hydrolyzed in a mixture of DBE and dioxane (**Figure B.23**).

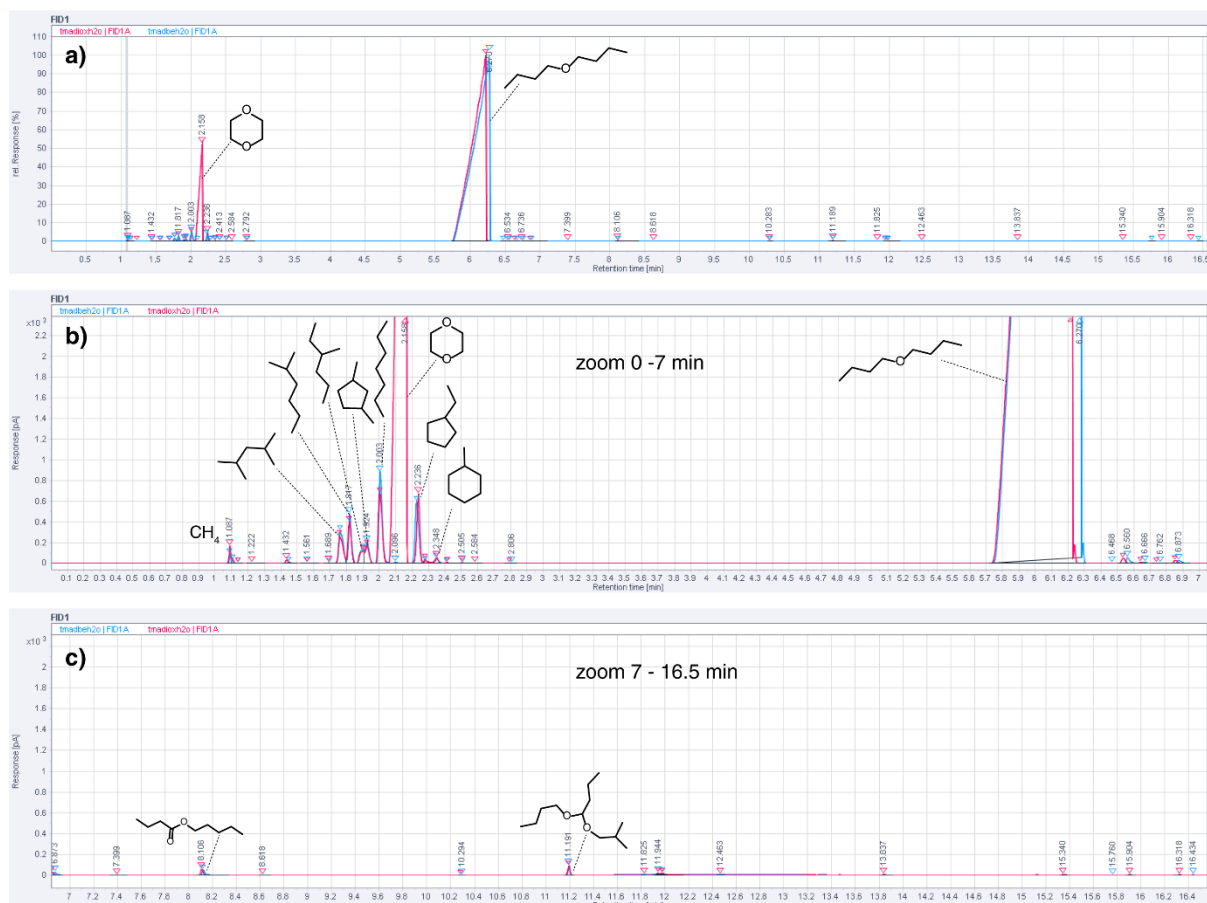


**Figure B.23:** Superimposed chromatograms corresponding to a solution of TMA hydrolyzed by water in DBE (blue chromatogram) and a mixture of dioxane and DBE (pink chromatogram). a) the full chromatograms b) a zoom on the first half of it and c) a zoom on the last part. Above the peaks, the corresponding molecule, identified by mass spectroscopy. The certainty of the structure of the two last peaks (part c) is high due to the very low concentration of these compounds. Methane is assumed to be the first compound to come out (no MS detection due to too low concentration).

The resulting chromatograms show the two major peaks: dioxane (2.096 min, in the solution containing it) and DBE (6.27 min). Beyond these two peaks, the number and the position of other small peaks are the same with area differences being due to measurement uncertainties the error of measurement. Small peaks have all been identified by GC-MS as impurities of DBE and dioxane and isomers of heptane (from the commercial TMA solution). No product of dioxane decomposition product was detected. However, these oxygenated products could come out at similar times as the solvent and be masked, which could still explain this effect.



## C Supplementary information of chapter 4

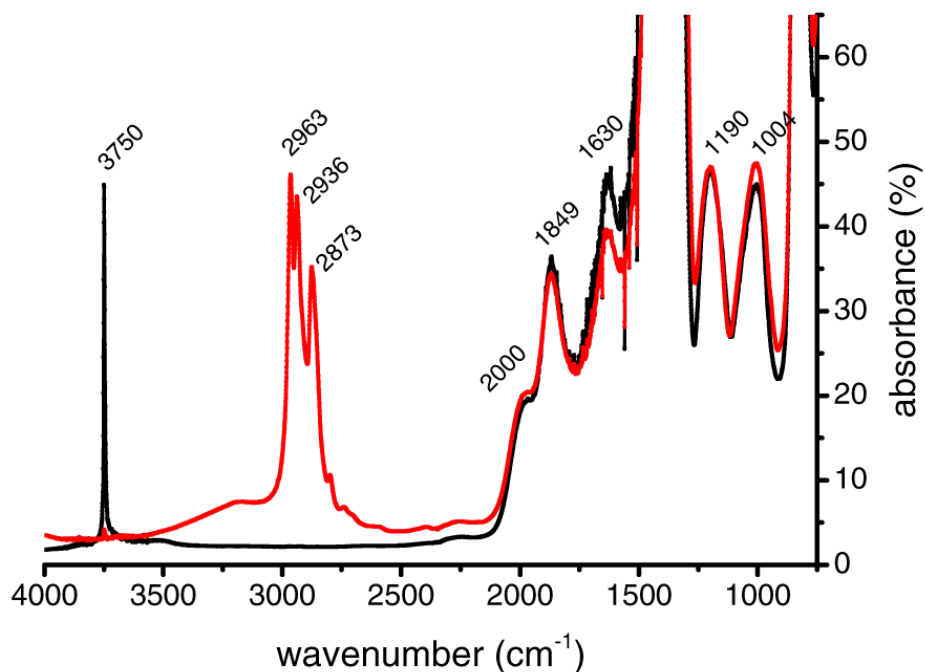


**Figure C.1:** Full window of DRIFT spectra of dehydroxylated silica (in black) and the same material after adding a stoichiometric amount of tri methyl aluminum (in red). The peak at 3750  $\text{cm}^{-1}$  is attributed to isolated hydroxyl vibration. The peaks at 2963, 2936 and 2873  $\text{cm}^{-1}$  are attributed to  $\text{CH}_2$  and  $\text{CH}_3$  vibrations from the aluminum precursor and the solvent still attached). The contribution below 2000  $\text{cm}^{-1}$  is mainly attributed to the vibrations of Si-O-Si bridges in the  $\text{SiO}_2$  bulk.

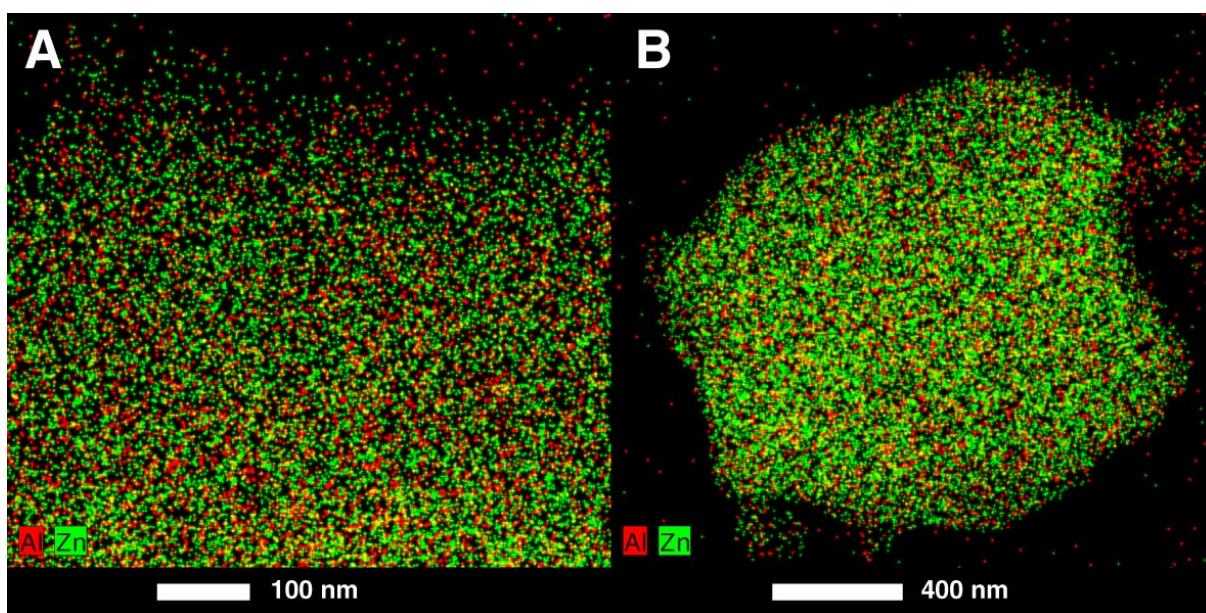


**Figure C.2:** Scanning transmission electron microscopy with energy disperse X-ray detector (STEM-EDX) elemental mapping of Al and Zn on as prepared "Zn-O-Al" catalyst. The sample display a

homogeneous distribution of Al and Zn throughout the silica matrix which is consistent with a homogeneous monolayer rather than particles formation.

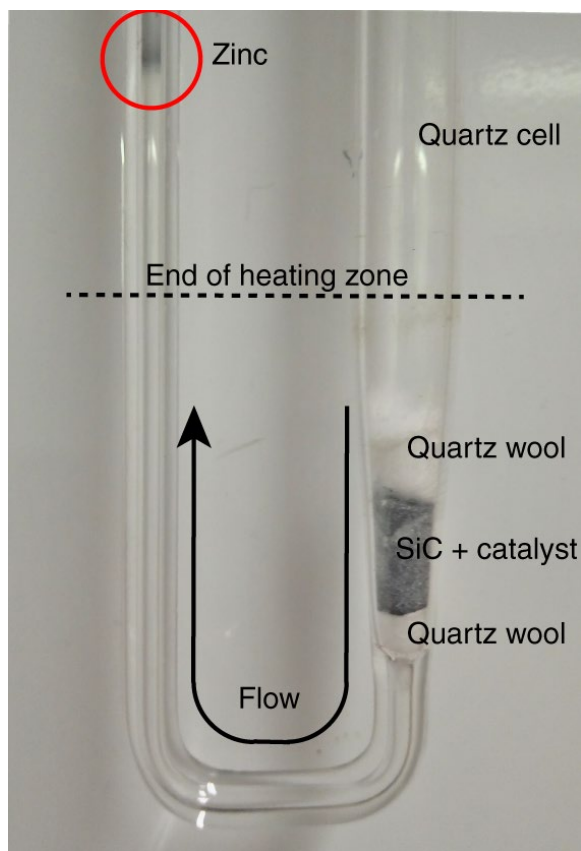


**Figure C.3:** Picture of the U shape quartz reactor containing the catalyst diluted in silicon carbide (SiC) stuck between two plugs of quartz wool. The red circle highlights the zone where the volatile zinc deposited after being carried off by the gas flow at high temperature.

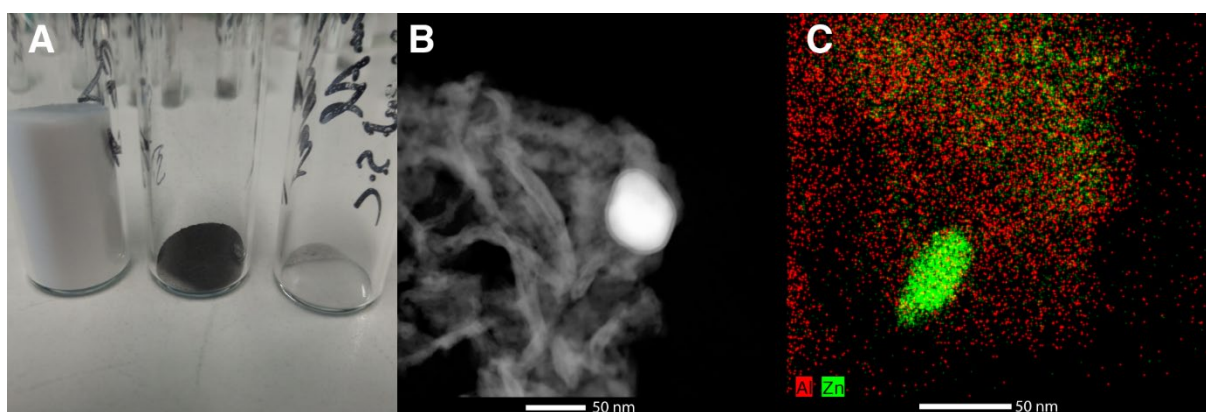


**Figure C.4:** Comparison of spent catalysts. (A) a picture showing, from left to right, fresh “Zn-O-Al”, spent “Zn-O-Al” from catalysis in stainless steel reactor and spent “Zn-O-Al” from quartz reactor. The fresh and spent in quartz samples are white (as should be the concerned metal oxide) while the catalyst spent in stainless steel reactor is black, indicative of extensive carbon deposition. (B) Scanning transmission electron microscopy (STEM) picture taken with high annular angle field (HAADF) detector of “Zn-O-Al” spent catalyst in stainless steel reactor. The picture shows carbon filaments that grew from a nanoparticle. Elemental analysis (with EDX detector) reveals that this

particle is made of pure iron and is likely coming from the pipes as no iron was detected on fresh catalysts. (C) STEM-EDX elemental mapping of “Zn-O-Al” spent catalyst in quartz reactor. In opposition with the previous case, no carbon filament were spotted. However, significant phase separation is observed as ZnO particles are spotted as well as some Zn-free zones around it. The aluminum seems to be still homogeneously dispersed.

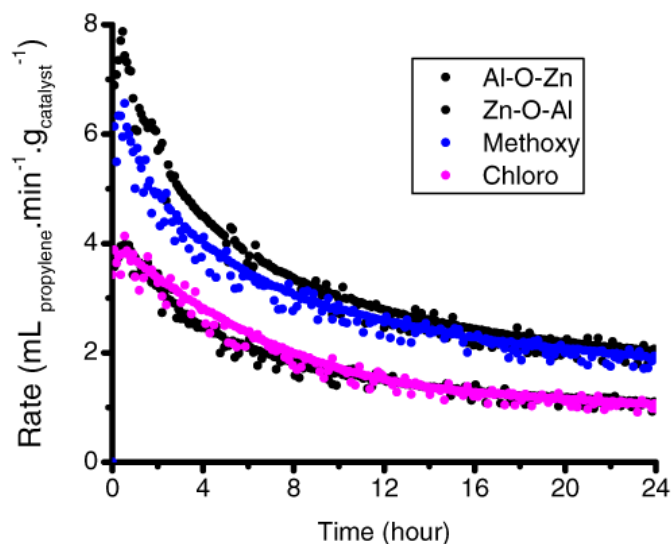


**Figure C.5:** Catalytic run in quartz reactor (550°C, 50 mL/min, 30% propane, 1 atm, 100 mg of catalyst). The data in black are the catalytic results showed in the main text and serves as a reference for the blue and pink one. In blue is the catalytic behavior of “Si-O-Zn-O-Al” when trimethyl methoxysilane was used as a precursor without the presence of pyridine. The match with “Zn-O-Al” behavior suggests that no silicon attached during the procedure. The pink data shows “Si-O-Zn-O-Al” catalyst when trimethyl chloride silane was used a precursor. The match with the “Al-O-Zn” behavior indicates that only one of the two zinc remain and it is unlikely that any silicon attached the surface.

# Chapter 5 Conclusion

## 5.1 Achieved results

The first objective, which was to design a method for layer-by-layer metal oxide deposition onto a catalyst surface, was successfully achieved and described in Chapter 2. The dispersion of a catalyst in an anhydrous organic solvent followed by alternating injections of aluminum alkoxide and water led to alumina growth selectively and conformally onto the catalyst surface. The method was highly reproducible, relatively easy to apply, and was efficient for stabilizing sensitive copper-based catalysts in harsh reaction conditions.

The second objective was to design a liquid-phase atomic layer deposition (ALD) method that would be more suitable for heterogeneous catalyst preparation than gas-phase ALD, while still matching its accuracy and versatility. In Chapter 3, this liquid-phase ALD method was presented with proof of self-limiting half reactions and high accuracy. Various materials were deposited (oxides, sulfides, and phosphates) on substrates relevant for heterogeneous catalysis (high and low surface area materials). These layers were extensively studied by electron microscopy and various types of spectroscopy to highlight the similar quality of overcoat conformality. Liquid-phase ALD turns out to be efficient at avoiding substrate agglomeration and requires only the stoichiometric amount of precursor needed per layer. This is in contrast with gas-phase ALD where, aside from a few specific processes being developed, extensive purges are required to avoid agglomeration and expensive precursors are always used in excess.

The third objective was to go beyond the current limitations of gas-phase ALD. This aim was reached in results described in Chapters 3 and 4. In Chapter 3, aluminum phosphate was deposited using inexpensive and non-volatile phosphoric acid as a phosphate source, which is not possible in gas-phase ALD. The overall process was drastically simplified from six steps (three injections and three purges) to two steps (two injections) per cycle. Moreover, up to 150 g of catalyst could be coated in a single batch, while usual commercial ALD reactors used in academia can only process 10 g per batch. Scaling up the process could be achieved with the usual tools available in a typical synthetic chemistry laboratory. Altogether, the ease of this method offers routes to greatly democratize the use of ALD in laboratory and, potentially, industrial settings.

In Chapter 4, liquid-phase ALD was successfully used to grow supported metal oxide clusters on silica. This procedure was only possible using the mild and stoichiometric conditions of liquid-phase ALD. Gas-phase ALD at regular temperatures would rehydroxylate the surface, leading to film growth. At room temperature, physisorbed water would also lead to the formation of a film. In addition, our method inherently allows us to track the stoichiometry of the reaction, which allows us to ensure cluster growth. Finally, we can easily switch between precursors by just using different ones at each injection. With gas phase ALD, due to the complexity of the physical setup, this operation would require extensive purging of lines and potential switching of the precursor sources, depending

on how many metals are targeted. Therefore, the method proposed here allows for relatively easy access to the controlled formation of multi-metal clusters for catalysis.

## 5.2 Future work and Outlook

In the short term, deeper characterization of the clusters presented in Chapter 4 is currently planned. Importantly, x-ray absorption spectroscopy measurements will provide more information about the electronic interactions between Al and Zn and their respective environments. Density functional theory will be used to better understand the bond dynamics and geometry around the Zn center. Finally, solid-state nuclear magnetic resonance will provide geometrical and electronic information around the aluminum atom.

In the medium term, the deposition of gallium oxide using trimethyl gallium via liquid-phase ALD would be an interesting target. Trialkyl gallium is less prone to hydrolysis than its aluminum or zinc counterparts. Therefore, the deposition of gallium oxide is an ideal demonstration that both halves of the ALD cycle (hydrolysis and condensation) can be catalyzed independently. The goal behind this project is to demonstrate that liquid-phase deposition allows a complete use of the liquid phase chemistry tool kit to solve ALD issues. Outside of the preparation challenge, gallium is a far better catalyst than zinc for propane dehydrogenation. Applying the approach described in Chapter 4 to gallium would possibly lead to a commercially competitive catalyst. Beyond this example, many active elements for catalysis have easily available precursors that could be used for deposition in this technique (e.g. Sn, Ti, Cu, Ni etc.).

In the longer term, another direction for material development could be the preparation of metal nitride layers by liquid-phase ALD. This would require some adjustments in the procedure as the precursors are very different from the examples described in Chapter 3. Metal chlorides ( $\text{TiCl}_4$ ,  $\text{GaCl}_3$  etc.) and ammonia react spontaneously and quickly to form amorphous metal nitrides, releasing  $\text{HCl}$ , and thus could be used for this deposition. As an example, a quick test mixing  $\text{GaCl}_3$  and ammonia quickly led to material precipitation. These opportunities will be further explored out by researchers following up on my project.

The immediate goal of this thesis work was to design a new way of preparing materials to unlock new strategies for understanding and synthesizing targeted active sites. The impact of my results will be measured by their utilization in challenges of applied catalysis such as green house gas conversion, ammonia synthesis, and biomass upgrading.



# Bibliography

- [1] E. Brown, *Des Chimistes de A à Z*, **2002**.
- [2] T. Montini, M. Melchionna, M. Monai, P. Fornasiero, *Chem. Rev.* **2016**, *116*, 5987.
- [3] J. C. Védrine, in *Met. Oxides Heterog. Catal.*, Elsevier, **2018**, pp. 1–41.
- [4] D. S. A. Simakov, H. Y. Luo, Y. Román-Leshkov, *Appl. Catal. B Environ.* **2015**, *168–169*, 540.
- [5] A. Venugopal, S. Naveen Kumar, J. Ashok, D. Hari Prasad, V. Durga Kumari, K. B. S. Prasad, M. Subrahmanyam, *Int. J. Hydrog. Energy* **2007**, *32*, 1782.
- [6] H. Hattori, Y. Ono, in *Met. Oxides Heterog. Catal.*, Elsevier, **2018**, pp. 133–209.
- [7] J. S. Noh, J. A. Schwarz, *J. Colloid Interface Sci.* **1989**, *130*, 157.
- [8] D. A. Sverjensky, *Geochim. Cosmochim. Acta* **1994**, *58*, 3123.
- [9] J. C. Hicks, R. Dabestani, A. C. Buchanan, C. W. Jones, *Chem. Mater.* **2006**, *18*, 5022.
- [10] B. Sow, S. Hamoudi, M. Hassan Zahedi-Niaki, S. Kaliaguine, *Microporous Mesoporous Mater.* **2005**, *79*, 129.
- [11] E. L. Margelefsky, R. K. Zeidan, M. E. Davis, *Chem. Soc. Rev.* **2008**, *37*, 1118.
- [12] K. Kalz, R. Kraehnert, M. Dvoyashkin, R. Dittmeyer, R. Gläser, U. Krewer, K. Reuter, J.-D. Grunwaldt, *ChemCatChem* **2016**, n/a.
- [13] T. W. Hansen, A. T. DeLaRiva, S. R. Challa, A. K. Datye, *Acc. Chem. Res.* **2013**, *46*, 1720.
- [14] S. Hu, W.-X. Li, *ChemCatChem* **2018**, *10*, 2900.
- [15] R. L. Coble, *J. Am. Ceram. Soc.* **1962**, *45*, 123.
- [16] C. H. Bartholomew, *Appl. Catal. Gen.* **2001**, *212*, 17.
- [17] C. Bartholomew, in *Kirk-Othmer Encycl. Chem. Technol.*, John Wiley & Sons, Inc., **2000**.
- [18] G. M. Lari, P. Y. Dapsens, D. Scholz, S. Mitchell, C. Mondelli, J. Pérez-Ramírez, *Green Chem.* **2016**, *18*, 1249.
- [19] J. M. Jones, V. A. Dupont, R. Brydson, D. J. Fullerton, N. S. Nasri, A. B. Ross, A. V. K. Westwood, *Catal. Today* **2003**, *81*, 589.
- [20] R. Rinaldi, F. Schüth, *Energy Environ. Sci.* **2009**, *2*, 610.
- [21] M. Besson, P. Gallezot, *Catal. Today* **2003**, *81*, 547.
- [22] C. Sievers, Y. Noda, L. Qi, E. M. Albuquerque, R. M. Rioux, S. L. Scott, *ACS Catal.* **2016**, *6*, 8286.
- [23] R.-J. Liu, P. A. Crozier, C. M. Smith, D. A. Hucul, J. Blackson, G. Salaita, *Appl. Catal. Gen.* **2005**, *282*, 111.
- [24] C. Hammond, *Green Chem.* **2017**, *19*, 2711.
- [25] J.-P. Lange, *Angew. Chem. Int. Ed.* **2015**, n/a.
- [26] X. Carrier, E. Marceau, J.-F. Lambert, M. Che, *J. Colloid Interface Sci.* **2007**, *308*, 429.
- [27] M. Besson, P. Gallezot, C. Pinel, *Chem. Rev.* **2014**, *114*, 1827.
- [28] S. Salameh, J. Gómez-Hernández, A. Goulas, H. Van Bui, J. R. van Ommen, *Particuology* **2017**, *30*, 15.
- [29] X. Carrier, S. Royer, E. Marceau, in *Met. Oxides Heterog. Catal.* (Ed.: J.C. Védrine), Elsevier, **2018**, pp. 43–103.
- [30] B. E. Yoldas, *Am. Ceram. Soc. bull.* **1975**, *54*.
- [31] K. Wfers, C. Misra, *Alcoa Technical Paper* **1987**.
- [32] G. C. Bye, J. G. Robinson, *Kolloid-Z. Z. Für Polym.* **n.d.**, *198*, 53.
- [33] J. Livage, M. Henry, C. Sanchez, *Prog. Solid State Chem.* **1988**, *18*, 259.
- [34] D. Zhao, *Science* **1998**, *279*, 548.
- [35] S. Marx, D. Avnir, *Acc. Chem. Res.* **2007**, *40*, 768.
- [36] A. Katz, M. E. Davis, *Nature* **2000**, *403*, 286.
- [37] D. L. Catone, E. Matijevic, *J. Colloid Interface Sci.* **1974**, *48*, 291.

- [38] Y. Murakami, T. Matsumoto, Y. Takasu, *J. Phys. Chem. B* **1999**, *103*, 1836.
- [39] J. N. Hasnidawani, H. N. Azlina, H. Norita, N. N. Bonnia, S. Ratim, E. S. Ali, *Procedia Chem.* **2016**, *19*, 211.
- [40] L. L. Hench, J. K. West, *Chem. Rev.* **1990**, *90*, 33.
- [41] S. Acosta, R. Corriu, D. Leclercq, P. H. Mutin, A. Vioux, *J. Sol-Gel Sci. Technol.* **1994**, *2*, 25.
- [42] A. Vioux, *Chem. Mater.* **1997**, *9*, 2292.
- [43] P. Arnal, R. J. P. Corriu, D. Leclercq, P. H. Mutin, A. Vioux, *J Mater Chem* **1996**, *6*, 1925.
- [44] S. Acosta, R. J. P. Corriu, D. Leclercq, P. Lefèvre, P. H. Mutin, A. Vioux, *J. Non-Cryst. Solids* **1994**, *170*, 234.
- [45] C. L. Lu, J. G. Lv, L. Xu, X. F. Guo, W. H. Hou, Y. Hu, H. Huang, *Nanotechnology* **2009**, *20*, 215604.
- [46] J. O. Eckert, C. C. Hung-Houston, B. L. Gersten, M. M. Lencka, R. E. Riman, *J. Am. Ceram. Soc.* **1996**, *79*, 2929.
- [47] C. S. Cundy, P. A. Cox, *Microporous Mesoporous Mater.* **2005**, *82*, 1.
- [48] O. M. Yaghi, H. Li, *J. Am. Chem. Soc.* **1995**, *117*, 10401.
- [49] S. ben Moussa, A. Mehri, M. Gruselle, P. Beaunier, G. Costentin, B. Badraoui, *Mater. Chem. Phys.* **2018**, *212*, 21.
- [50] M. Hirano, E. Kato, *J. Am. Ceram. Soc.* **1996**, *79*, 777.
- [51] J. Joo, B. Y. Chow, M. Prakash, E. S. Boyden, J. M. Jacobson, *Nat. Mater.* **2011**, *10*, 596.
- [52] H. Yin, Y. Wada, T. Kitamura, S. Kambe, S. Murasawa, H. Mori, T. Sakata, S. Yanagida, *J. Mater. Chem.* **2001**, *11*, 1694.
- [53] K. P. De Jong, J. W. Geus, *Catal. Rev.* **2000**, *42*, 481.
- [54] Ç. Öncel, Y. Yürüm, *Fuller. Nanotub. Carbon Nanostructures* **2006**, *14*, 17.
- [55] P. A. Goodman, H. Li, Y. Gao, Y. F. Lu, J. D. Stenger-Smith, J. Redepenning, *Carbon* **2013**, *55*, 291.
- [56] C. Moreno-Castilla, F. J. Maldonado-Hódar, *Carbon* **2005**, *43*, 455.
- [57] P. Losch, W. Huang, E. D. Goodman, C. J. Wrasman, A. Holm, A. R. Riscoe, J. A. Schwalbe, M. Cargnello, *Nano Today* **2019**, *24*, 15.
- [58] P. Prieel, H. Adekunle Salami, R. H. Padilla, Z. Zhong, J. A. Lopez-Sanchez, *Chin. J. Catal.* **2016**, *37*, 1619.
- [59] B. Roldan Cuenya, F. Behafarid, *Surf. Sci. Rep.* **2015**, *70*, 135.
- [60] A. Trovarelli, J. Llorca, *ACS Catal.* **2017**, *7*, 4716.
- [61] L. D. Pachón, G. Rothenberg, *Appl. Organomet. Chem.* **2008**, *22*, 288.
- [62] P. Munnik, P. E. de Jongh, K. P. de Jong, *Chem. Rev.* **2015**, DOI 10.1021/cr500486u.
- [63] M. Campanati, G. Fornasari, A. Vaccari, *Catal. Today* **2003**, *77*, 299.
- [64] J.-D. Grunwaldt, C. Kiener, C. Wögerbauer, A. Baiker, *J. Catal.* **1999**, *181*, 223.
- [65] J. R. A. Sietsma, J. D. Meeldijk, M. Versluijs-Helder, A. Broersma, A. J. van Dillen, P. E. de Jongh, K. P. de Jong, *Chem. Mater.* **2008**, *20*, 2921.
- [66] J. A. Farmer, C. T. Campbell, *Science* **2010**, *329*, 933.
- [67] H. Yan, C. Su, J. He, W. Chen, *J. Mater. Chem. A* **2018**, *6*, 8793.
- [68] H. Zhang, G. Liu, L. Shi, J. Ye, *Adv. Energy Mater.* **n.d.**, n/a.
- [69] X.-F. Yang, A. Wang, B. Qiao, J. Li, J. Liu, T. Zhang, *Acc. Chem. Res.* **2013**, *46*, 1740.
- [70] J. M. Thomas, R. Raja, D. W. Lewis, *Angew. Chem. Int. Ed.* **2005**, *44*, 6456.
- [71] L. DeRita, S. Dai, K. Lopez-Zepeda, N. Pham, G. W. Graham, X. Pan, P. Christopher, *J. Am. Chem. Soc.* **2017**, *139*, 14150.
- [72] S. F. J. Hackett, R. M. Brydson, M. H. Gass, I. Harvey, A. D. Newman, K. Wilson, A. F. Lee, *Angew. Chem. Int. Ed.* **2007**, *46*, 8593.
- [73] K. Asakura, H. Nagahiro, N. Ichikuni, Y. Iwasawa, *Appl. Catal. Gen.* **1999**, *188*, 313.
- [74] Q. Fu, *Science* **2003**, *301*, 935.
- [75] J. Jones, H. Xiong, A. T. DeLaRiva, E. J. Peterson, H. Pham, S. R. Challa, G. Qi, S. Oh, M. H. Wiebenga, X. I. Pereira Hernandez, Y. Wang, A. K. Datye, *Science* **2016**, *353*, 150.



- [76] E. D. Goodman, A. C. Johnston-Peck, E. M. Dietze, C. J. Wrasman, A. S. Hoffman, F. Abild-Pedersen, S. R. Bare, P. N. Plessow, M. Cargnello, *Nat. Catal.* **2019**, 2, 748.
- [77] Y. Chen, S. Ji, Y. Wang, J. Dong, W. Chen, Z. Li, R. Shen, L. Zheng, Z. Zhuang, D. Wang, Y. Li, *Angew. Chem. Int. Ed.* **2017**, 56, 6937.
- [78] G. Giannakakis, M. Flytzani-Stephanopoulos, E. C. H. Sykes, *Acc. Chem. Res.* **2019**, 52, 237.
- [79] A. Beniya, S. Higashi, *Nat. Catal.* **2019**, 2, 590.
- [80] C. Copéret, A. Comas-Vives, M. P. Conley, D. P. Estes, A. Fedorov, V. Mougel, H. Nagae, F. Núñez-Zarur, P. A. Zhizhko, *Chem. Rev.* **2016**, 116, 323.
- [81] B. Qiao, A. Wang, X. Yang, L. F. Allard, Z. Jiang, Y. Cui, J. Liu, J. Li, T. Zhang, *Nat. Chem.* **2011**, 3, 634.
- [82] M. Moliner, Y. Roman-Leshkov, M. E. Davis, *Proc. Natl. Acad. Sci.* **2010**, 107, 6164.
- [83] E. Nikolla, Y. Román-Leshkov, M. Moliner, M. E. Davis, *ACS Catal.* **2011**, 1, 408.
- [84] H. Wei, X. Liu, A. Wang, L. Zhang, B. Qiao, X. Yang, Y. Huang, S. Miao, J. Liu, T. Zhang, *Nat. Commun.* **2014**, 5, DOI 10.1038/ncomms6634.
- [85] S. Zhao, Y. Cheng, J.-P. Veder, B. Johannessen, M. Saunders, L. Zhang, C. Liu, M. F. Chisholm, R. De Marco, J. Liu, S.-Z. Yang, S. P. Jiang, *ACS Appl. Energy Mater.* **2018**, DOI 10.1021/acsaem.8b00903.
- [86] F. A. Westerhaus, R. V. Jagadeesh, G. Wienhöfer, M.-M. Pohl, J. Radnik, A.-E. Surkus, J. Rabeah, K. Junge, H. Junge, M. Nielsen, A. Brückner, M. Beller, *Nat. Chem.* **2013**, 5, 537.
- [87] S. P. Desai, J. Ye, J. Zheng, M. S. Ferrandon, T. E. Webber, A. E. Platero-Prats, J. Duan, P. Garcia-Holley, D. M. Camaioni, K. W. Chapman, M. Delferro, O. K. Farha, J. L. Fulton, L. Gagliardi, J. A. Lercher, R. L. Penn, A. Stein, C. C. Lu, *J. Am. Chem. Soc.* **2018**, 140, 15309.
- [88] P. Aich, H. Wei, B. Basan, A. J. Kropf, N. M. Schweitzer, C. L. Marshall, J. T. Miller, R. Meyer, *J. Phys. Chem. C* **2015**, 119, 18140.
- [89] M. D. Marcinkowski, M. T. Darby, J. Liu, J. M. Wimple, F. R. Lucci, S. Lee, A. Michaelides, M. Flytzani-Stephanopoulos, M. Stamatakis, E. C. H. Sykes, *Nat. Chem.* **2018**, 10, 325.
- [90] F. R. Lucci, M. T. Darby, M. F. G. Mattera, C. J. Ivimey, A. J. Therrien, A. Michaelides, M. Stamatakis, E. C. H. Sykes, *J. Phys. Chem. Lett.* **2016**, 7, 480.
- [91] C. Copéret, A. Fedorov, P. A. Zhizhko, *Catal. Lett.* **2017**, 147, 2247.
- [92] C. Copéret, M. Chabanas, R. Petroff Saint-Arroman, J.-M. Basset, *Angew. Chem. Int. Ed.* **2003**, 42, 156.
- [93] C. Copéret, *Nat. Energy* **2019**, DOI 10.1038/s41560-019-0491-2.
- [94] R. Mueller, H. K. Kammler, K. Wegner, S. E. Pratsinis, *Langmuir* **2003**, 19, 160.
- [95] M. Digne, P. Sautet, P. Raybaud, P. Euzen, H. Toulhoat, *J. Catal.* **2002**, 211, 1.
- [96] R. Wischert, C. Copéret, F. Delbecq, P. Sautet, *Angew. Chem. Int. Ed.* **2011**, 50, 3202.
- [97] L. T. Zhuravlev, *Colloids Surf. Physicochem. Eng. Asp.* **2000**, 173, 1.
- [98] M. Leskelä, M. Ritala, *Angew. Chem. Int. Ed.* **2003**, 42, 5548.
- [99] R. W. Johnson, A. Hultqvist, S. F. Bent, *Mater. Today* **2014**, 17, 236.
- [100] C. Marichy, M. Bechelany, N. Pinna, *Adv. Mater.* **2012**, 24, 1017.
- [101] Q. Sun, K. C. Lau, D. Geng, X. Meng, *Batter. Supercaps* **2018**, 1, 41.
- [102] V. Zardetto, B. L. Williams, A. Perrotta, F. Di Giacomo, M. A. Verheijen, R. Andriessen, W. M. M. Kessels, M. Creatore, *Sustain. Energy Fuels* **2017**, 1, 30.
- [103] N. P. Dasgupta, H.-B.-R. Lee, S. F. Bent, P. S. Weiss, *Chem. Mater.* **2016**, 28, 1943.
- [104] J. M. Lownsbury, J. A. Gladden, C. T. Campbell, I. S. Kim, A. B. F. Martinson, *Chem. Mater.* **2017**, DOI 10.1021/acs.chemmater.7b01491.
- [105] S. M. George, *Chem. Rev.* **2010**, 110, 111.
- [106] T. J. Knisley, L. C. Kalutarage, C. H. Winter, *Coord. Chem. Rev.* **2013**, 257, 3222.
- [107] M. B. M. Mousa, C. J. Oldham, G. N. Parsons, "Atmospheric Pressure Atomic Layer Deposition of Al<sub>2</sub>O<sub>3</sub> Using Trimethyl Aluminum and Ozone," DOI 10.1021/la500796r can be found under <https://pubs.acs.org/doi/abs/10.1021/la500796r>, **2014**.
- [108] Jesse. S. Jur, G. N. Parsons, *ACS Appl. Mater. Interfaces* **2011**, 3, 299.

- [109] R. L. Puurunen, *J. Appl. Phys.* **2005**, *97*, 121301.
- [110] B. J. O'Neill, D. H. K. Jackson, J. Lee, C. Canlas, P. C. Stair, C. L. Marshall, J. W. Elam, T. F. Kuech, J. A. Dumesic, G. W. Huber, *ACS Catal.* **2015**, *5*, 1804.
- [111] M. D. Groner, F. H. Fabreguette, J. W. Elam, S. M. George, *Chem. Mater.* **2004**, *16*, 639.
- [112] M. Rooth, A. Johansson, K. Kukli, J. Aarik, M. Boman, A. Hårsta, *Chem. Vap. Depos.* **2008**, *14*, 67.
- [113] S. B. S. Heil, J. L. van Hemmen, M. C. M. van de Sanden, W. M. M. Kessels, *J. Appl. Phys.* **2008**, *103*, 103302.
- [114] K. Kukli, K. Forsgren, J. Aarik, T. Uustare, A. Aidla, A. Niskanen, M. Ritala, M. Leskelä, A. Hårsta, *J. Cryst. Growth* **2001**, *231*, 262.
- [115] R. O'Donoghue, J. Rechmann, M. Aghaee, D. Rogalla, H.-W. Becker, M. Creatore, A. D. Wieck, A. Devi, *Dalton Trans.* **2017**, *46*, 16551.
- [116] M. E. Bartram, T. A. Michalske, J. W. Rogers, R. T. Paine, *Chem. Mater.* **1993**, *5*, 1424.
- [117] R. L. Puurunen, A. Root, P. Sarv, M. M. Viitanen, H. H. Brongersma, M. Lindblad, A. O. I. Krause, *Chem. Mater.* **2002**, *14*, 720.
- [118] J. Hämäläinen, M. Mattinen, K. Mizohata, K. Meinander, M. Vehkamäki, J. Räisänen, M. Ritala, M. Leskelä, *Adv. Mater.* **2018**, *30*, 1703622.
- [119] C. Goehry, N. Schneider, *J. Phys. Chem. C* **2017**, *121*, 5871.
- [120] S. Sinha, N. Mahuli, S. K. Sarkar, *J. Vac. Sci. Technol. Vac. Surf. Films* **2015**, *33*, 01A139.
- [121] J. Hämäläinen, J. Holopainen, F. Munnik, M. Heikkilä, M. Ritala, M. Leskelä, *J. Phys. Chem. C* **2012**, *116*, 5920.
- [122] S. D. Elliott, *Langmuir* **2010**, *26*, 9179.
- [123] D. J. H. Emslie, P. Chadha, J. S. Price, *Coord. Chem. Rev.* **2013**, *257*, 3282.
- [124] J. Hämäläinen, M. Ritala, M. Leskelä, *Chem. Mater.* **2014**, *26*, 786.
- [125] H. Feng, J. A. Libera, P. C. Stair, J. T. Miller, J. W. Elam, *ACS Catal.* **2011**, *1*, 665.
- [126] K. L. Pickrahn, A. Garg, S. F. Bent, *ACS Catal.* **2015**, *5*, 1609.
- [127] S. M. George, B. Yoon, A. A. Dameron, *Acc. Chem. Res.* **2009**, *42*, 498.
- [128] X. Meng, *J. Mater. Chem. A* **2017**, *5*, 18326.
- [129] J. Cai, Q. Sun, X. Meng, Department of Mechanical Engineering, University of Arkansas, Fayetteville, AR 72701, the United States, *AIMS Mater. Sci.* **2018**, *5*, 957.
- [130] D. Sarkar, S. Ishchuk, D. H. Taffa, N. Kaynan, B. A. Berke, T. Bendikov, R. Yerushalmi, *J. Phys. Chem. C* **2016**, *120*, 3853.
- [131] C. Chen, P. Li, G. Wang, Y. Yu, F. Duan, C. Chen, W. Song, Y. Qin, M. Knez, *Angew. Chem. Int. Ed.* **2013**, *52*, 9196.
- [132] B. Gong, J. C. Spagnola, G. N. Parsons, *J. Vac. Sci. Technol. Vac. Surf. Films* **2012**, *30*, 01A156.
- [133] R. L. Puurunen, W. Vandervorst, *J. Appl. Phys.* **2004**, *96*, 7686.
- [134] H.-B.-R. Lee, M. N. Mullings, X. Jiang, B. M. Clemens, S. F. Bent, *Chem. Mater.* **2012**, *24*, 4051.
- [135] A. J. M. Mackus, M. A. Verheijen, N. Leick, A. A. Bol, W. M. M. Kessels, *Chem. Mater.* **2013**, *25*, 1905.
- [136] Y. Zhang, J. A. Bertrand, R. Yang, S. M. George, Y. C. Lee, *Thin Solid Films* **2009**, *517*, 3269.
- [137] Y. Zhang, D. Seghete, A. Abdulagatov, Z. Gibbs, A. Cavanagh, R. Yang, S. George, Y.-C. Lee, *Surf. Coat. Technol.* **2011**, *205*, 3334.
- [138] T. A. Krajewski, U. Wachnicki, O. Witkowski, B. Guziejewicz, M. Godlewski, N. Huby, G. Tallarida, *n.d.*, 10.
- [139] D. Choi, K.-B. Chung, J.-S. Park, *Thin Solid Films* **2013**, *546*, 31.
- [140] B. J. O'Neill, D. H. K. Jackson, A. J. Crisci, C. A. Farberow, F. Shi, A. C. Alba-Rubio, J. Lu, P. J. Dietrich, X. Gu, C. L. Marshall, P. C. Stair, J. W. Elam, J. T. Miller, F. H. Ribeiro, P. M. Voyles, J. Greeley, M. Mavrikakis, S. L. Scott, T. F. Kuech, J. A. Dumesic, *Angew. Chem.* **2013**, *125*, 14053.

- [141] A. C. Alba-Rubio, B. J. O'Neill, F. Shi, C. Akatay, C. Canlas, T. Li, R. Winans, J. W. Elam, E. A. Stach, P. M. Voyles, J. A. Dumesic, *ACS Catal.* **2014**, *4*, 1554.
- [142] V. Sudheeshkumar, A. Lushington, X. Sun, R. W. J. Scott, *ACS Appl. Nano Mater.* **2018**, DOI 10.1021/acsanm.8b01709.
- [143] X. Liu, Q. Zhu, Y. Lang, K. Cao, S. Chu, B. Shan, R. Chen, *Angew. Chem. Int. Ed.* **2017**, *56*, 1648.
- [144] J. W. Han, C. Kim, J. S. Park, H. Lee, *ChemSusChem* **2014**, *7*, 451.
- [145] J. Lu, B. Fu, M. C. Kung, G. Xiao, J. W. Elam, H. H. Kung, P. C. Stair, *Science* **2012**, *335*, 1205.
- [146] K. Kraffert, M. Karg, R. Schmack, G. Clavel, C. Boissiere, T. Wirth, N. Pinna, R. Kraehnert, *Adv. Mater. Interfaces* **2018**, *5*, 1800360.
- [147] T. M. Onn, L. Arroyo-Ramirez, M. Monai, T.-S. Oh, M. Talati, P. Fornasiero, R. J. Gorte, M. M. Khader, *Appl. Catal. B Environ.* **2016**, *197*, 280.
- [148] H. Zhang, X.-K. Gu, C. Canlas, A. J. Kropf, P. Aich, J. P. Greeley, J. W. Elam, R. J. Meyers, J. A. Dumesic, P. C. Stair, C. L. Marshall, *Angew. Chem. Int. Ed.* **2014**, *53*, 12132.
- [149] C. P. Canlas, J. Lu, N. A. Ray, N. A. Grosso-Giordano, S. Lee, J. W. Elam, R. E. Winans, R. P. Van Duyne, P. C. Stair, J. M. Notestein, *Nat. Chem.* **2012**, *4*, 1030.
- [150] Z. Shang, X. Liang, *Nano Lett.* **2017**, *17*, 104.
- [151] H. Yi, H. Du, Y. Hu, H. Yan, H.-L. Jiang, J. Lu, *ACS Catal.* **2015**, *5*, 2735.
- [152] J. Zhao, C. Chen, B. Zhang, Z. Jiao, J. Zhang, J. Yang, Y. Qin, *Catal. Commun.* **2019**, *121*, 48.
- [153] T. W. van Deelen, C. Hernández Mejía, K. P. de Jong, *Nat. Catal.* **2019**, *2*, 955.
- [154] C. T. Campbell, *Nat. Chem.* **2012**, *4*, 597.
- [155] J. Zhang, J. W. Medlin, *Surf. Sci. Rep.* **2018**, DOI 10.1016/j.surfrep.2018.06.002.
- [156] R. M. Kennedy, L. A. Crosby, K. Ding, C. P. Canlas, A. Gulec, L. D. Marks, J. W. Elam, C. L. Marshall, K. R. Poepelmeier, P. C. Stair, *Catal. Lett.* **2018**, *148*, 2223.
- [157] K. Hayek, R. Kramer, Z. Paál, *Appl. Catal. Gen.* **1997**, *162*, 1.
- [158] R. Burch, A. R. Flambard, *J. Catal.* **1982**, *78*, 389.
- [159] L. Wang, J. Zhang, Y. Zhu, S. Xu, C. Wang, C. Bian, X. Meng, F.-S. Xiao, *ACS Catal* **2017**, 7461.
- [160] C. H. Mejía, T. W. van Deelen, K. P. de Jong, *Nat. Commun.* **2018**, *9*, 4459.
- [161] J. Lee, S. P. Burt, C. A. Carrero, A. C. Alba-Rubio, I. Ro, B. J. O'Neill, H. J. Kim, D. H. K. Jackson, T. F. Kuech, I. Hermans, J. A. Dumesic, G. W. Huber, *J. Catal.* **2015**, *330*, 19.
- [162] N. Cheng, M. Norouzi Banis, J. Liu, A. Riese, S. Mu, R. Li, T.-K. Sham, X. Sun, *Energy Environ. Sci.* **2015**, *8*, 1450.
- [163] F. Jiang, J. Huang, L. Niu, G. Xiao, *Catal. Lett.* **2015**, *145*, 947.
- [164] S. P. Sree, J. Dendooven, T. I. Korányi, G. Vanbutsele, K. Houthoofd, D. Deduytsche, C. De-tavernier, J. A. Martens, *Catal. Sci. Technol.* **2011**, *1*, 218.
- [165] J. Keränen, P. Carniti, A. Gervasini, E. Iiskola, A. Auroux, L. Niinistö, *Catal. Today* **2004**, *91–92*, 67.
- [166] Y. J. Pagán-Torres, J. M. R. Gallo, D. Wang, H. N. Pham, J. A. Libera, C. L. Marshall, J. W. Elam, A. K. Datye, J. A. Dumesic, *ACS Catal.* **2011**, *1*, 1234.
- [167] S. Mahurin, L. Bao, W. Yan, C. Liang, S. Dai, *J. Non-Cryst. Solids* **2006**, *352*, 3280.
- [168] J. A. Libera, J. W. Elam, M. J. Pellin, *Thin Solid Films* **2008**, *516*, 6158.
- [169] Y. Liu, L. Zhang, F. Göttl, M. R. Ball, I. Hermans, T. F. Kuech, M. Mavrikakis, J. A. Dumesic, *ACS Catal.* **2018**, *8*, 10707.
- [170] T. M. Onn, S. Zhang, L. Arroyo-Ramirez, Y. Xia, C. Wang, X. Pan, G. W. Graham, R. J. Gorte, *Appl. Catal. B Environ.* **2017**, *201*, 430.
- [171] T. M. Onn, M. Monai, S. Dai, L. Arroyo-Ramirez, S. Zhang, X. Pan, G. W. Graham, P. Fornasiero, R. J. Gorte, *Appl. Catal. Gen.* **2017**, *534*, 70.
- [172] T. M. Onn, M. Monai, S. Dai, E. Fonda, T. Montini, X. Pan, G. W. Graham, P. Fornasiero, R. J. Gorte, *J. Am. Chem. Soc.* **2018**, *140*, 4841.

- [173] J. Li, X. Liang, D. M. King, Y.-B. Jiang, A. W. Weimer, *Appl. Catal. B Environ.* **2010**, *97*, 220.
- [174] T. D. Gould, A. M. Lubers, B. T. Neltner, J. V. Carrier, A. W. Weimer, J. L. Falconer, J. Will Medlin, *J. Catal.* **2013**, *303*, 9.
- [175] K. Wettergren, F. F. Schweinberger, D. Deiana, C. J. Ridge, A. S. Crampton, M. D. Rötzer, T. W. Hansen, V. P. Zhdanov, U. Heiz, C. Langhammer, *Nano Lett.* **2014**, *14*, 5803.
- [176] S. T. Christensen, H. Feng, J. L. Libera, N. Guo, J. T. Miller, P. C. Stair, J. W. Elam, *Nano Lett.* **2010**, *10*, 3047.
- [177] M. J. Weber, A. J. M. Mackus, M. A. Verheijen, C. van der Marel, W. M. M. Kessels, *Chem. Mater.* **2012**, *24*, 2973.
- [178] J. Lu, K.-B. Low, Y. Lei, J. A. Libera, A. Nicholls, P. C. Stair, J. W. Elam, *Nat. Commun.* **2014**, *5*, 3264.
- [179] J. Lu, P. C. Stair, *Angew. Chem. Int. Ed.* **2010**, *49*, 2547.
- [180] N. Cheng, X. Sun, *Chin. J. Catal.* **2017**, *38*, 1508.
- [181] H. Yan, H. Cheng, H. Yi, Y. Lin, T. Yao, C. Wang, J. Li, S. Wei, J. Lu, *J. Am. Chem. Soc.* **2015**, *137*, 10484.
- [182] N. Cheng, S. Stambula, D. Wang, M. N. Banis, J. Liu, A. Riese, B. Xiao, R. Li, T.-K. Sham, L.-M. Liu, G. A. Botton, X. Sun, *Nat. Commun.* **2016**, *7*, 13638.
- [183] J. Camacho-Bunquin, P. Aich, M. Ferrandon, A. “Bean” Getsoian, U. Das, F. Dogan, L. A. Curtiss, J. T. Miller, C. L. Marshall, A. S. Hock, P. C. Stair, *J. Catal.* **2017**, *345*, 170.
- [184] L. Zhang, R. Si, H. Liu, N. Chen, Q. Wang, K. Adair, Z. Wang, J. Chen, Z. Song, J. Li, M. N. Banis, R. Li, T.-K. Sham, M. Gu, L.-M. Liu, G. A. Botton, X. Sun, *Nat. Commun.* **2019**, *10*, DOI 10.1038/s41467-019-12887-y.
- [185] E. Granneman, P. Fischer, D. Pierreux, H. Terhorst, P. Zagwijn, *Surf. Coat. Technol.* **2007**, *201*, 8899.
- [186] P. Poodt, D. C. Cameron, E. Dickey, S. M. George, V. Kuznetsov, G. N. Parsons, F. Roozeboom, G. Sundaram, A. Vermeer, *J. Vac. Sci. Technol. Vac. Surf. Films* **2012**, *30*, 010802.
- [187] P. Ryan Fitzpatrick, Z. M. Gibbs, S. M. George, *J. Vac. Sci. Technol. Vac. Surf. Films* **2012**, *30*, 01A136.
- [188] D. H. Levy, S. F. Nelson, D. Freeman, *J. Disp. Technol.* **2009**, *5*, 484.
- [189] T. M. Onn, R. Küngas, P. Fornasiero, K. Huang, R. J. Gorte, *Inorganics* **2018**, *6*, 34.
- [190] D. Longrie, D. Deduytsche, C. Detavernier, *J. Vac. Sci. Technol. Vac. Surf. Films* **2014**, *32*, 010802.
- [191] S. Adhikari, S. Selvaraj, D.-H. Kim, *Adv. Mater. Interfaces* **n.d.**, *0*, 1800581.
- [192] L. F. Hakim, J. Blackson, S. M. George, A. W. Weimer, *Chem. Vap. Depos.* **n.d.**, *11*, 420.
- [193] A. P. Didden, J. Middelkoop, W. F. A. Besling, D. E. Nanu, R. van de Krol, *Rev. Sci. Instrum.* **2014**, *85*, 013905.
- [194] A. W. Weimer, *J. Nanoparticle Res.* **2019**, *21*, DOI 10.1007/s11051-018-4442-9.
- [195] J. A. McCormick, K. P. Rice, D. F. Paul, A. W. Weimer, S. M. George, *Chem. Vap. Depos.* **2007**, *13*, 491.
- [196] D. Longrie, D. Deduytsche, J. Haemers, K. Driesen, C. Detavernier, *Surf. Coat. Technol.* **2012**, *213*, 183.
- [197] J. A. McCormick, B. L. Cloutier, A. W. Weimer, S. M. George, *J. Vac. Sci. Technol. Vac. Surf. Films* **2007**, *25*, 67.
- [198] C.-L. Duan, X. Liu, B. Shan, R. Chen, *Rev. Sci. Instrum.* **2015**, *86*, 075101.
- [199] J. R. van Ommen, D. Kooijman, M. de Niet, M. Talebi, A. Goulas, *J. Vac. Sci. Technol. Vac. Surf. Films* **2015**, *33*, 021513.
- [200] J.-P. Lange, *Angew. Chem. Int. Ed.* **2015**, *54*, 13186.
- [201] C. H. Bartholomew, *Appl. Catal. Gen.* **2001**, *212*, 17.
- [202] F. Héroguel, B. Rozmysłowicz, J. S. Luterbacher, *Chim. Int. J. Chem.* **2015**, *69*, 582.

- [203] T. J. Schwartz, B. J. O'Neill, B. H. Shanks, J. A. Dumesic, *ACS Catal.* **2014**, *4*, 2060.
- [204] J. S. Luterbacher, D. M. Alonso, J. A. Dumesic, *Green Chem.* **2014**, *16*, 4816.
- [205] M. V. Twigg, M. S. Spencer, *Appl. Catal. Gen.* **2001**, *212*, 161.
- [206] B. J. O'Neill, D. H. K. Jackson, A. J. Crisci, C. A. Farberow, F. Shi, A. C. Alba-Rubio, J. Lu, P. J. Dietrich, X. Gu, C. L. Marshall, P. C. Stair, J. W. Elam, J. T. Miller, F. H. Ribeiro, P. M. Voyles, J. Greeley, M. Mavrikakis, S. L. Scott, T. F. Kuech, J. A. Dumesic, *Angew. Chem. Int. Ed.* **2013**, *52*, 13808.
- [207] I. Lee, Q. Zhang, J. Ge, Y. Yin, F. Zaera, *Nano Res.* **2010**, *4*, 115.
- [208] Z. Bo, T. R. Eaton, J. R. Gallagher, C. P. Canlas, J. T. Miller, J. M. Notestein, *Chem. Mater.* **2015**, *27*, 1269.
- [209] M. Caillot, A. Chaumonnot, M. Digne, C. Poleunis, D. P. Debecker, J. A. vanBokhoven, *Microporous Mesoporous Mater.* **2014**, *185*, 179.
- [210] F. Héroguel, G. Siddiqi, M. D. Detwiler, D. Y. Zemlyanov, O. Safonova, C. Copéret, *J Catal* **2015**, *321*, 81.
- [211] K. Wang, Y. Lin, M. A. Morris, J. D. Holmes, *J. Mater. Chem.* **2006**, *16*, 4051.
- [212] F. Zhang, X. Carrier, J.-M. Krafft, Y. Yoshimura, J. Blanchard, *New J. Chem.* **2010**, *34*, 508.
- [213] E. Santacesaria, M. Cozzolino, M. Di Serio, A. M. Venezia, R. Tesser, *Appl. Catal. Gen.* **2004**, *270*, 177.
- [214] W. Yan, S. M. Mahurin, S. H. Overbury, S. Dai, *Top. Catal.* **2006**, *39*, 199.
- [215] M. Baca, E. de la Rochefoucauld, E. Ambroise, J.-M. Krafft, R. Hajjar, P. P. Man, X. Carrier, J. Blanchard, *Microporous Mesoporous Mater.* **2008**, *110*, 232.
- [216] P. Iengo, M. Di Serio, A. Sorrentino, V. Solinas, E. Santacesaria, *Appl. Catal. Gen.* **1998**, *167*, 85.
- [217] A. Dandekar, M. A. Vannice, *J. Catal.* **1998**, *178*, 621.
- [218] K. Larmier, S. Tada, A. Comas-Vives, C. Copéret, *J. Phys. Chem. Lett.* **2016**, *7*, 3259.
- [219] R. Wischert, C. Coperet, F. Delbecq, P. Sautet, *Angew. Chem.-Int. Ed.* **2011**, *50*, 3202.
- [220] D. M. Alonso, S. G. Wettstein, M. A. Mellmer, E. I. Gurbuz, J. A. Dumesic, *Energy Environ. Sci.* **2012**, *6*, 76.
- [221] C. M. Cai, T. Zhang, R. Kumar, C. E. Wyman, *J. Chem. Technol. Biotechnol.* **2014**, *89*, 2.
- [222] A. Eseyin E., E. E. Anthonia, H. S. Philip, *Int. J. Adv. Chem.* **2015**, *3*, 42.
- [223] M. A. Mellmer, C. Sener, J. M. R. Gallo, J. S. Luterbacher, D. M. Alonso, J. A. Dumesic, *Angew. Chem. Int. Ed.* **2014**, *53*, 11872.
- [224] L. Shuai, J. Luterbacher, *ChemSusChem* **2016**, *9*, 133.
- [225] B. J. O'Neill, J. T. Miller, P. J. Dietrich, F. G. Sollberger, F. H. Ribeiro, J. A. Dumesic, *Chem-CatChem* **2014**, *6*, 2493.
- [226] R. L. Puurunen, *Chem. Vap. Depos.* **2014**, *20*, 332.
- [227] Y.-Q. Cao, X.-R. Zhao, J. Chen, W. Zhang, M. Li, L. Zhu, X.-J. Zhang, D. Wu, A.-D. Li, *Sci. Rep.* **2018**, *8*, 12131.
- [228] L. F. Hakim, D. M. King, Y. Zhou, C. J. Gump, S. M. George, A. W. Weimer, *Adv. Funct. Mater.* **2007**, *17*, 3175.
- [229] J. Lu, J. W. Elam, P. C. Stair, *Surf. Sci. Rep.* **2016**, *71*, 410.
- [230] F. Héroguel, L. Silvioli, Y.-P. Du, J. S. Luterbacher, *J. Catal.* **2018**, *358*, 50.
- [231] Y.-P. Du, F. Héroguel, J. S. Luterbacher, *Small* **2018**, *14*, 1801733.
- [232] A. Loiudice, M. Strach, S. Saris, D. Chernyshov, R. Buonsanti, *J. Am. Chem. Soc.* **2019**, DOI 10.1021/jacs.9b02061.
- [233] F. Héroguel, B. P. Le Monnier, K. S. Brown, J. C. Siu, J. S. Luterbacher, *Appl. Catal. B Environ.* **2017**, *218*, 643.
- [234] K. S. Brown, C. Saggese, B. P. Le Monnier, F. Héroguel, J. S. Luterbacher, *J. Phys. Chem. C* **2018**, *122*, 6713.
- [235] H. M. Pathan, C. D. Lokhande, *Bull. Mater. Sci.* **2004**, *27*, 85.

- [236] Y. Wu, D. Döhler, M. Barr, E. Oks, M. Wolf, L. Santinacci, J. Bachmann, *Nano Lett.* **2015**, *15*, 6379.
- [237] J. Li, J. A. DiVerdi, G. E. Maciel, **2006**, 17093.
- [238] R. N. Kerber, A. Kermagoret, E. Callens, P. Florian, D. Massiot, A. Lesage, C. Copéret, F. Delbecq, X. Rozanska, P. Sautet, *J. Am. Chem. Soc.* **2012**, *134*, 6767.
- [239] C. Guerra-Nuñez, M. Döbeli, J. Michler, I. Utke, *Chem. Mater.* **2017**, DOI 10.1021/acs.chemmater.7b02759.
- [240] A. C. Dillon, A. W. Ott, J. D. Way, S. M. George, *Surf. Sci.* **1995**, *322*, 230.
- [241] M. K. Wiedmann, D. H. K. Jackson, Y. J. Pagan-Torres, E. Cho, J. A. Dumesic, T. F. Kuech, *J. Vac. Sci. Technol. A* **2011**, *30*, 01A134.
- [242] S. Knohl, A. K. Roy, R. Lungwitz, S. Spange, T. Mäder, D. J. Nestler, B. Wielage, S. Schulze, M. Hietschold, H. Wulff, C. A. Helm, F. Seidel, D. R. T. Zahn, W. A. Goedel, *ACS Appl. Mater. Interfaces* **2013**, *5*, 6161.
- [243] Y. S. Kim, S. J. Yun, *Appl. Surf. Sci.* **2004**, *229*, 105.
- [244] J. Ihanus, M. Ritala, M. Leskelä, T. Prohaska, R. Resch, G. Friedbacher, M. Grasserbauer, *Appl. Surf. Sci.* **1997**, *120*, 43.
- [245] R. J. Ding, L. He, Z. Ye, A. L. Cui, C. H. Sun, L. F. Liu, X. N. Hu, in *Infrared Technol. Appl. XLIV* (Eds.: G.F. Fulop, C.M. Hanson, P.R. Norton, B.F. Andresen, J.L. Miller), SPIE, Orlando, United States, **2018**, p. 72.
- [246] W. Stöber, A. Fink, E. Bohn, *J. Colloid Interface Sci.* **1968**, *26*, 62.
- [247] F. Qi, B. Xu, Z. Chen, L. Zhang, P. Zhang, D. Sun, *Chem. Eng. J.* **2010**, *165*, 490.
- [248] F. Qi, Z. Chen, B. Xu, J. Shen, J. Ma, C. Joll, A. Heitz, *Appl. Catal. B Environ.* **2008**, *84*, 684.
- [249] H. Tamura, A. Tanaka, K. Mita, R. Furuichi, *J. Colloid Interface Sci.* **1999**, *209*, 225.
- [250] S. Seo, B. C. Yeo, S. S. Han, C. M. Yoon, J. Y. Yang, J. Yoon, C. Yoo, H. Kim, Y. Lee, S. J. Lee, J.-M. Myoung, H.-B.-R. Lee, W.-H. Kim, I.-K. Oh, H. Kim, *ACS Appl. Mater. Interfaces* **2017**, *9*, 41607.
- [251] M. Cargnello, V. V. T. Doan-Nguyen, T. R. Gordon, R. E. Diaz, E. A. Stach, R. J. Gorte, P. Fornasiero, C. B. Murray, *Science* **2013**, *341*, 771.
- [252] F. Calle-Vallejo, J. Tymoczko, V. Colic, Q. H. Vu, M. D. Pohl, K. Morgenstern, D. Loffreda, P. Sautet, W. Schuhmann, A. S. Bandarenka, *Science* **2015**, *350*, 185.
- [253] G.-M. Schwab, *Discuss. Faraday Soc.* **1950**, *8*, 166.
- [254] A. J. Plomp, D. M. P. van Asten, A. M. J. van der Eerden, P. Mäki-Arvela, D. Yu. Murzin, K. P. de Jong, J. H. Bitter, *J. Catal.* **2009**, *263*, 146.
- [255] L. Wang, E. Guan, J. Zhang, J. Yang, Y. Zhu, Y. Han, M. Yang, C. Cen, G. Fu, B. C. Gates, F.-S. Xiao, *Nat. Commun.* **2018**, *9*, 1.
- [256] J. Jiao, R. Lin, S. Liu, W.-C. Cheong, C. Zhang, Z. Chen, Y. Pan, J. Tang, K. Wu, S.-F. Hung, H. M. Chen, L. Zheng, Q. Lu, X. Yang, B. Xu, H. Xiao, J. Li, D. Wang, Q. Peng, C. Chen, Y. Li, *Nat. Chem.* **2019**, *11*, 222.
- [257] J. Paterson, M. Potter, E. Gianotti, R. Raja, *Chem. Commun.* **2011**, *47*, 517.
- [258] A. Bakandritsos, R. G. Kadam, P. Kumar, G. Zoppellaro, M. Medved', J. Tuček, T. Montini, O. Tomanec, P. Andrášková, B. Drahoš, R. S. Varma, M. Otyepka, M. B. Gawande, P. Fornasiero, R. Zbořil, *Adv. Mater.* **2019**, *31*, 1900323.
- [259] J.-K. Lee, M. C. Kung, H. H. Kung, *Top. Catal.* **2008**, *49*, 136.
- [260] N. I. Jaeger, K. Möller, P. J. Plath, *J. Chem. Soc. Faraday Trans. 1 Phys. Chem. Condens. Phases* **1986**, *82*, 3315.
- [261] S. Bordiga, E. Groppo, G. Agostini, J. A. van Bokhoven, C. Lamberti, *Chem. Rev.* **2013**, *113*, 1736.
- [262] D. S. Su, T. Jacob, T. W. Hansen, D. Wang, R. Schlögl, B. Freitag, S. Kujawa, *Angew. Chem. Int. Ed.* **2008**, *47*, 5005.
- [263] T. Kobayashi, F. A. Perras, I. I. Slowing, A. D. Sadow, M. Pruski, *ACS Catal.* **2015**, *5*, 7055.
- [264] T. Kobayashi, M. Pruski, *ACS Catal.* **2019**, *9*, 7238.

- [265] T. Lunkenbein, J. Schumann, M. Behrens, R. Schlögl, M. G. Willinger, *Angew. Chem. Int. Ed.* **2015**, *54*, 4544.
- [266] B. P. L. Monnier, F. Wells, F. Talebkeikhah, J. S. Luterbacher, *Adv. Mater.* **2019**, *31*, 1904276.
- [267] S. D. Fleischman, S. L. Scott, *J. Am. Chem. Soc.* **2011**, *133*, 4847.
- [268] R. H. Stolen, G. E. Walrafen, *J. Chem. Phys.* **1976**, *64*, 2623.
- [269] P. S. Bagus, E. S. Ilton, C. J. Nelin, *Surf. Sci. Rep.* **2013**, *68*, 273.
- [270] N. M. Schweitzer, B. Hu, U. Das, H. Kim, J. Greeley, L. A. Curtiss, P. C. Stair, J. T. Miller, A. S. Hock, *ACS Catal.* **2014**, *4*, 1091.
- [271] I. Chorkendorff, J. W. Niemantsverdriet, *Concepts of Modern Catalysis and Kinetics*, John Wiley & Sons, **2006**.
- [272] S. Lew, A. F. Sarofim, M. Flytzani-Stephanopoulos, *Chem. Eng. Sci.* **1992**, *47*, 1421.
- [273] N. A. Ray, R. P. Van Duyne, P. C. Stair, *J. Phys. Chem. C* **2012**, *116*, 7748.
- [274] N. Cheng, M. N. Banis, J. Liu, A. Riese, X. Li, R. Li, S. Ye, S. Knights, X. Sun, *Adv. Mater.* **2015**, *27*, 277.
- [275] M. Piernavieja-Hermida, Z. Lu, A. White, K.-B. Low, T. Wu, J. W. Elam, Z. Wu, Y. Lei, *Nanoscale* **2016**, *8*, 15348.
- [276] In *Chem. Elem. Second Ed.*, Butterworth-Heinemann, Oxford, **1997**, pp. 1201–1226.
- [277] R. A. Assink, and B. D. Kay, *Annu. Rev. Mater. Sci.* **1991**, *21*, 491.
- [278] Y. Du, X. Du, S. M. George, *J. Phys. Chem. C* **2007**, *111*, 219.
- [279] M. E. Davis, R. J. Davis, *Fundamentals of Chemical Reaction Engineering*, McGraw-Hill Higher Education, New York, NY, **2003**.
- [280] P. Harriott, *Chemical Reactor Design*, **2003**.
- [281] [http://www.ddbst.com/en/EED/PCP/VIS\\_C39.php](http://www.ddbst.com/en/EED/PCP/VIS_C39.php) n.d.
- [282] S. R. S. Sastri, S. Mohanty, K. K. Rao, *Can. J. Chem. Eng.* **1996**, *74*, 170.
- [283] S. K. Lee, S. B. Lee, S. Y. Park, Y. S. Yi, C. W. Ahn, *Phys. Rev. Lett.* **2009**, *103*, DOI 10.1103/PhysRevLett.103.095501.
- [284] B. Topuz, D. Şimşek, M. Çiftçioğlu, *Ceram. Int.* **2015**, *41*, 43.
- [285] D. Barreca, A. Gasparotto, C. Maccato, C. Maragno, E. Tondello, *Surf. Sci. Spectra* **2006**, *13*, 81.
- [286] J. A. Rotole, P. M. A. Sherwood, *Surf. Sci. Spectra* **1998**, *5*, 53.
- [287] R. Lookman, P. Grobet, R. Merckx, W. H. Van Riemsdijk, *Geoderma* **1997**, *80*, 369.
- [288] R. Zhao, P. Rupper, S. Gaan, *Coatings* **2017**, *7*, 133.
- [289] J. A. Rotole, P. M. A. Sherwood, *Surf. Sci. Spectra* **1998**, *5*, 60.
- [290] J. P. McCullough, J. F. Messerly, R. T. Moore, S. S. Todd, *J. Phys. Chem.* **1963**, *67*, 677.
- [291] D. R. LIDE, *Handbook of Chemistry and Physics*, CRC Press, **2001**.
- [292] X. Meng, J. Wu, Z. Liu, *J. Chem. Eng. Data* **2009**, *54*, 2353.
- [293] E. G. Hoffmann, *Transaction Of The Faraday Society*, Amsterdam, **1961**.
- [294] T. Mole, E. A. Jeffery, *Organoaluminium Compounds*, Elsevier, **1972**.
- [295] B. Smith, *Journal of Organometallic Chemistry* **1972**, *46*, 31.
- [296] M. J. D. Low, A. G. Severdia, J. Chan, *J. Catal.* **1981**, *69*, 384.

# Curriculum vitae

Benjamin P. Le Monnier

French  
29/08/1992  
+41 21 693 36 85

[benjaminpierre.lemonnier@epfl.ch](mailto:benjaminpierre.lemonnier@epfl.ch)  
[Google Scholar](#)

## EDUCATION

---

- 2015 Master of Material Chemistry and Catalysis  
Pierre and Marie Curie University (now called Sorbonne University)
- 2013 Bachelor of Chemistry  
Sorbonne University
- 2012 Technological university Diploma of Chemistry (material chemistry minor)  
Joseph Fourier University

## RESEARCH LABORATORY EXPERIENCE

---

- 2015 PhD studies, 4.5 years  
*Heterogeneous catalyst design by liquid-phase Atomic Layer Deposition*  
Laboratoire des procédés durables et catalytiques (LPDC)  
Ecole Fédérale Polytechnique de Lausanne (EPFL)  
Supervisor: Prof. Jeremy S. Luterbacher
- 2015 Master level internship, 5 months  
*Sol-gel overcoating of catalysts for biomass conversion*  
LPDC - EPFL  
Supervisor: Prof. Jeremy S. Luterbacher
- 2014 Master level internship, 5 months  
*Cu nanoparticle size effect on hydrogen sorption properties of  $\text{LiBH}_4$*   
Group of Inorganic Chemistry and Catalysis  
Utrecht University  
Supervisor: Prof. Petra De Jongh
- 2013 Bachelor level internship, 1 month  
*Hydration study of hybrid organic inorganic solid electrolyte*  
Laboratoire de Chimie de la Matière Condensée de Paris  
Sorbonne University  
Supervisor: Prof. Christel Laberty-Robert
- 2013 Bachelor level internship, 2 months  
*Hydroxy apatite preparation by hydrothermal method*  
Laboratoire de Réactivité de Surface



Sorbonne University  
Supervisor: Dr. Frederic Averseng

2012 Laboratory technician level internship, 3 months  
*Raman analysis of fuel cell electrode*  
Laboratoire d'Electrochimie et Physicochimie des Matériaux et Interfaces  
Université Savoie Mont Blanc  
Supervisor: Prof. Corine Bas

## TEACHING AND MENTORING

---

2019-2020 Safety mentoring of a Phd student, Farzaneh Talebkeikhah

2019 Supervisor of a master project  
*“Atom by atom heterogeneous catalyst design”*, Raphael Schnyder

2017-2018 Supervision of a laboratory technician training, Frederick Wells

2016-2019 Teaching assistant (TA) and occasional lecturer for a theoretical course  
*“Heterogeneous reaction engineering”*, master level (3 semesters, 3 h/week)

2015-2018 TA and head of TAs for a practical course  
*“Chemical engineering lab and project”*, master level (3 semesters, 8 h/week)

2015-2016 Co-supervision of short-term interns, Kristopher Brown and Juno Siu

## MEMBERSHIPS

---

2018 American Institute of Chemical Engineers member

2015-2020 Swiss Chemical Society member

## AWARDS

---

2019 Teaching excellence award – assistant, 1 000 CHF

2015 Eole grant, 500 euro

## PUBLICATIONS

---

- Ydna M Questell-Santiago, Jher Hau Yeap, Masoud Talebi Amiri, **Benjamin P Le Monnier**, Jeremy S Luterbacher, Catalyst evolution enhances production of xylitol from acetal-stabilized xylose, ACS Sustainable Chem. Eng. 2020  
<https://pubs.acs.org/doi/abs/10.1021/acssuschemeng.9b06456>
- **Benjamin P. Le Monnier**, Frederik Wells, Farzaneh Talebkeikhah and Jeremy S. Luterbacher, Atomic layer deposition on dispersed material in liquid phase by stoichiometrically limited injections, Advanced Materials, 31, (52), 1970373  
<https://onlinelibrary.wiley.com/doi/10.1002/adma.201904276>
- Bartosz Rozmysłowicz, Jher Hau Yeap, Ahmed M. I. Elkhaiary, Masoud Talebi Amiri, Robert L. Shahab, Ydna M. Questell-Santiago, Charilaos Xiros, **Benjamin P. Le Monnier**, Michael H. Studer and Jeremy S. Luterbacher, Catalytic valorization of the acetate fraction of biomass to aromatics and its integration into the carboxylate platform, Green chem., 2019, 21, 2801-2809  
<https://pubs.rsc.org/en/content/articlehtml/2019/gc/c9gc00513g>
- Kristopher S Brown, Chiara Saggese, **Benjamin P. Le Monnier**, Florent Héroguel, Jeremy Scott Luterbacher, *A Simulation of Gas and Liquid-Phase Layer-by-Layer Deposition of Metal Oxides by Coarse-Grained Modeling*, J. Phys. Chem. C, 2018, vol 218, 643  
<https://pubs.acs.org/doi/abs/10.1021/acs.jpcc.8b00197>
- Florent Héroguel\*, **Benjamin P Le Monnier\***, Kristopher S Brown, Juno C Siu, Jeremy S Luterbacher, *Catalyst stabilization by stoichiometrically limited layer-by-layer overcoating in liquid media*, Appl. Catal. B: Environmental, 2017, vol 2018, 643.  
\*Co-first authors  
<https://www.sciencedirect.com/science/article/pii/S092633731730646X>
- Márton Kollár, Luka Ćirić, J Hugo Dil, Andrew Weber, Stefan Muff, Henrik M Ronnow, Bálint Náfrádi, **Benjamin Pierre Le Monnier**, Jeremy Scott Luterbacher, László Forró, Endre Horváth, *Clean, cleaved surfaces of the photovoltaic perovskite*, Sci. rep., 2017, vol 7, issue 1, 695  
<https://www.nature.com/articles/s41598-017-00799-0>

## CONTRIBUTION TO INTERNATIONAL CONFERENCES

---

- American Institute of chemical engineers annual meeting, Pittsburg, U.S.A, 2018  
“Liquid phase atomic layer deposition on powder”  
Poster presentation
- Swiss Chemical Society fall meeting, Lausanne, Switzerland, 2018  
“Cheap and upscalable process for liquid phase atomic layer deposition on powder”  
Poster presentation

- Swiss Chemical Society fall meeting, Zurich, Switzerland, 2016  
“Catalyst overcoating by chemical layer deposition”  
Poster presentation
- Trends in Nanotechnology meeting, Fribourg, Switzerland, 2016  
“Catalyst overcoating by chemical layer deposition”  
Poster presentation

## TECHNICAL SKILLS

---

### Synthesis and preparation

- Support preparation, nanoparticle deposition and single atom grafting for catalysis
- Synthesis under inert atmosphere (glovebox, Schlenck line)
- Atomic Layer Deposition using a fluidized bed reactor
- Liquid-phase ALD in batch reactor

### Characterization

- Electron microscopy (SEM and TEM- BF/DF/HAADF/EDX)
- Physisorption and chemisorption (apparatus upgrading and analysis)
- Single crystal and powder X-ray diffraction
- Gas chromatography for gas and liquid analysis – TCD/MS/FID
- Standard chemical analysis (IR, UV, NMR)

### Catalysis

- Continuous flow reactor in liquid and gas phase (building and using the setups)
- High pressure batch reactor

### Digital competence

- Pack Office
- Illustrator
- Olex2 (SCXRD structure refinement)
- Origin (data processing)
- Blender (3D design and animation)